Multimodal structural, compositional, and mechanical characterization of cortical bone on the micron scale

D i s s e r t a t i o n

zur Erlangung des akademischen Grades
doctor rerum naturalium
(Dr. rer. nat.)
im Fach: Physik
Spezialisierung: Experimentalphysik
eingereicht an der
Mathematisch-Naturwissenschaftliche Fakultät
der Humboldt-Universität zu Berlin
von

Diplom Physikerin Susanne Schrof

Präsident der Humboldt-Universität zu Berlin
Prof. Dr.-Ing. Dr. Sabine Kunst

Dekan der Mathematisch-Naturwissenschaftlichen Fakultät
Prof. Dr. Elmar Kulke

Gutachter/innen:
1. Prof. Dr. Kay Raum
2. Prof. Dr. Peter Fratzl
3. Prof. Dr. Helga Lichtenegger

Tag der mündlichen Prüfung: 03.03.2017

Abstract

Key design factors determining the remarkable mechanical performance of bone are the material composition and the complex hierarchically structure. To further elucidate the intricate interplay of structural, compositional, and mechanical aspects of bone tissue on the (sub-) micron length scale, this work introduces novel experimental approaches that allow for concurrent high-resolution imaging of complementary tissue parameters.

Polarized Raman spectroscopy (PRS) was applied to simultaneously investigate structural and compositional properties of human lamellar bone in a single experiment. In particular, it was demonstrated that PRS can be employed to decipher the three-dimensional organization of collagen fibrils. The anisotropic Raman scattering of the collagen-associated amide I band was spatially analyzed as a function of the incident laser polarization and allowed for identification of different parameters related to the orientation and the degree of alignment of the collagen fibrils in the lamellar structure. By supporting the experimental analysis with theoretical models, two coexisting major fibrillar organization patterns were identified. Furthermore, spectral indicators of the degree of alignment suggested the presence of disordered collagen within the lamellar organization.
To further extend the analysis, PRS experiments were combined with synchrotron X-ray phase contrast nano tomography (SR-nanoCT) and scanning acoustic microscopy (SAM) measurements in a site-matched study design. This multimodal approach aimed to investigate the link between lamellar architecture, composition and resulting elastic properties of healthy femoral bone at two levels of bone structural hierarchy: (i) single bone lamellae and (ii) entire tissue domains. In line with earlier studies, cross-correlation analysis strongly suggested that the characteristic elastic modulations of bone lamellae were the result of the twisting fibrillar orientation, rather than compositional variations, modulations of the mineral particle maturity, or mass density fluctuations. Furthermore, it was demonstrated how predominant fibril orientations in entire tissue domains can be effectively assessed from PRS parameter maps. Interestingly, predominant fiber orientations could be linked to the coexistence of different plywood arrangements within individual structural tissue domains.
In addition to the investigations of healthy human bone, SAM was applied

to analyze the pathologic impact of the neurofibromin 1 gene (Nf1) mutation on the development of the mechanical performance of the cortical bone matrix. Experimental analysis of two knock-out mouse models revealed that only Nf1 ablation in early mesenchymal progenitor cells significantly impairs the elastic stiffness of the long bone cortex.

Finally, the findings of this thesis provided proof of the versatility of the employed technical approaches. In particular, the capability of the combined PRS and SAM approach in providing compositional and 3D structural information in relation to local elastic material behavior in a complex fiber composite such as bone was demonstrated. In future studies, the presented multimodal methodology can be translated for non-destructive investigation of small pathologic samples from bone biopsies and for characterization of a broad range of other biological and synthetic materials.

Keywords

Multimodal analysis, lamellar bone, polarized Raman spectroscopy, scanning acoustic microscopy, chemical composition, collagen fibril orientation, mass density, elastic stiffness

Kurzzusammenfassung

Zu den Schlüsselfaktoren der bemerkenswerten mechanischen Eigenschaften von Knochen gehören die komplexe hierarchische Struktur und die chemische Zusammensetzung des Materials. Um das komplexe Zusammenwirken von strukturellen, kompositionellen und mechanischen Aspekten von Knochengewebe auf der (Sub-) Mikrometerskala weiter aufzuklären, stellt die vorliegende Arbeit neue experimentelle Konzepte vor, die einen simultanen Zugang zu komplementären Parametern ermöglichen.

Um sowohl kompositionelle als auch strukturelle Informationen über humanen lamellären Knochen in einem Experiment zu gewinnen, wurde Polarisierte Raman Spektroskopie (PRS) eingesetzt. Es konnte gezeigt werden, dass PRS nicht nur verwendet werden kann, um Veränderungen der Materialzusammensetzung zu erfassen, sondern auch um die drei-dimensionale Organisation der Kollagenfasern aufzuklären. Hierfür wurde die anisotrope Streuung des kollagen-assoziierten Amide I Ramanbandes als Funktion der Laserpolarisation analysiert. Im Rahmen der modellgestützten Analyse wurden verschiedene Parameter ausgemacht, die mit der Faserorientierung und dem Grad der Faserordnung im Gewebe in Verbindung gebracht werden konnten. Zwei koexistierende Faserorganisationsmuster wurden identifiziert und Hinweise auf ungeordnete Faseranteile in der lamellären Struktur erbracht.
Die Analyse wurde durch Kombination der PRS Experimente mit Synchrotron-Röntgen-Phasenkontrast-Tomografie und Rasterultraschallmikroskopie erweitert. Ziel des multimodalen Ansatzes war es, parallel die lamelläre Faserarchitektur, deren Materialzusammensetzung und die daraus hervorgehenden lokalen elastischen Eigenschaften auf zwei hierarchischen Ebenen der Knochenstruktur zu untersuchen: (i) einzelnen Knochenlamellen und (ii) kompletten Gewebedomänen. Durch Kreuzkorrelationsanalyse wurde aufgezeigt, dass die charakteristischen lamellären Modulationen der Elastizität in erster Linie durch sich lokal ändernde Faserorientierungen bedingt werden und nicht durch Variationen der Materialzusammensetzung, Abweichungen der Mineralkristallpartikeleigenschaften oder durch Fluktuationen der Massendichte. Darüber hinaus wurde dargestellt, wie dominante Faserorientierungen ganzer Gewebedomänen effizient aus PRS-Daten abgeleitet werden können. Interessanterweise konnten diese dominanten

Faserorientierungen mit der Koexistenz verschiedener Faserorganisationsmustern in den Gewebedomänen verknüpft werden.
Zusätzlich zu den Untersuchungen an gesundem humanem Knochen wurde mittels akustischer Mikroskopie der Einfluss der Mutation des Neurofibromin 1 (Nf1) Genes auf die pathologische Entwicklung der mechanischen Knochenkortexeigenschaften untersucht. Durch experimentelle Analyse zweier Knockout-Mausmodelle wurde festgestellt, dass nur eine Nf1 Mutation in frühen mesenchymalen Vorläuferzellen die Steifigkeit der Röhrenknochen signifikant beeinträchtigt.

Die Ergebnisse dieser Arbeit verdeutlichen die Vielseitigkeit der verwendeten experimentellen Ansätze, insbesondere die der Kombination von Raman- und Ultraschallmikroskopie, welche zur Darstellung von Komposition und 3D Struktur in Relation zur lokalen Elastizität in einem komplexen Faserverbundwerkstoff wie Knochen genutzt wurde. Perspektivisch eignet sich dieser multimodale Ansatz für nicht-destruktive Untersuchungen von pathologischen Knochenproben aus Biopsien und darüber hinaus zur Charakterisierung eines breiten Spektrums biologischer und synthetischer Materialien.

Schlüsselwörter

Multimodale Analyse, lamellärer Knochen, polarisierte Raman Spektroskopie, akustische Rastermikroskopie, chemische Komposition, Kollagenfaserorientierung, Massendichte, elastische Steifigkeit

Table of contents

Table of contents

1

Introduction

1.1 Motivation

Bone is a living fiber composite material, highly optimized to fulfill manifold essential metabolic and structural functions in the human body. From a metabolic point of view, bone's major function is to provide a mineral reservoir necessary for maintaining the body's calcium and phosphorus homeostasis. The structural duties of bone include the support of the body, enabling movement, the coverage and protection of brain and inner organs, and the housing of blood-forming marrow [1, 2].

Bone has remarkable mechanical properties, it optimally combines high stiffness and strength with toughness, allowing it to withstand static and dynamic loads without appreciable bending or fracturing. Yet, it maintains light weight. Moreover, bone material is not static, but continuously remodeling in order to respond to external loading situations and to self-repair damages [3].

The mechanical competence of bone is the result of the composition of two dissimilar phases, i.e. organic collagen fibrils and inorganic mineral particles, which are arranged in a complex hierarchical structure. This hierarchy encompasses multiple levels at various length scales from the nano- to the macroscale, each optimized regarding the overall functional performance of the material. Thus, understanding of the mechanical properties of bone requires fundamental characterization of every organizational level in a multiscale framework. Even though bone hierarchy and composition have been the subject of considerable research, the synergy between compositional and structural aspects and its link on the local mechanical performance on the (sub-)microscopic level are still not fully understood. By introducing novel experimental approaches, allowing for concurrent assessment of complementary multiscalar tissue parameters, the study on hand attempts to further decipher this intricate interplay of composition, structure, and mechanics.

The outstanding characteristics of bone have drawn attention to the material not only in basic clinical science, but have also become a source of inspira-

tion for the design of novel synthetic bio-inspired materials. Still, bone characterization is most relevant from a medical point of view, not only because mechanical competence is of key importance with regard to bone fractures, but also because disorders of the structure-function relationship can lead to severe diseases such as osteoporosis or osteogenesis imperfecta. The basis for medical research is the understanding and characterization of healthy bone, as presented in this thesis, which is essential for recognition, investigation, and treatment of pathological conditions.

1.2 Objectives

The main research focus of this work is the investigation of (human) lamellar cortical bone. Lamellar bone is the most abundant type in the cortex of human bones [4]. On the micron scale, lamellar bone exhibits anisotropic elastic properties, which have been attributed to a multitude of material and structural properties. Its complex 3D fibrillar architecture, chemical composition, tissue mineralization, mass density, and the size and shape of mineral particles have emerged as key factors in previous studies [5–8].

It has been demonstrated that the collagen fibrils in lamellar bone are arranged in a sophisticated layered microarchitecture, following 3D organization patterns. This microarchitecture is assumed to integrate anisotropic stiffness and toughness, optimizing the mechanical competence regarding the local mechanical environment [9–13]. To elucidate the fibrillar arrangement patterns, a wide range of analytical techniques has been applied that allowed to probe structural orientation. Amongst others, light [14, 15] and electron microscopy [16–21], X-ray imaging [13], X-ray small- and wide angle scattering or diffraction [22] were applied. The majority of these studies described the lamella as a staggered array of sublayers, each consisting of unidirectional aligned fibrils with a distinct angle of twist. However, the descriptions differed with respect to the individual sublayer thickness, twist angle and packing. Regarding the local mechanical properties of the bone lamellae, many of these techniques were limited to structural imaging only and failed in providing a more comprehensive picture of other correlated tissue properties, such as the tissue composition. Moreover, many of the approaches required elaborate sample preparation (dehydration, embedding, demineralization, or thin sections) or were limited by a small field of view.
Polarized Raman spectroscopy (PRS) is a non-destructive imaging tool providing a high lateral resolution ($\leq 1\mu m$) that can be applied to analyze bone samples in a close to native state. Its use is well established for the characterization of bone tissue composition [23–25] and mineral maturity [26, 27]. Additionally, it was demonstrated that PRS can also provide structural material information, because the intensity of PRS scattering depends on both the

chemical composition and on the spatial orientation of the vibrational units with respect to the orientation of the incident laser polarization. Therefore, particular Raman bands exhibit significant peak modulations in highly structured biological tissues such as tendon or bone [24, 28, 29]. Due to systematically organized arrangements of mineral platelets and collagen fibrils in bone, these mineral and collagen associated bands exhibit anisotropic intensity responses [30–34]. Previous studies on rat tail tendon PRS experiments [35] and theoretical simulations of collagen molecule spectroscopy [36] took first steps towards deriving 3D orientation information on collagen by exploiting the anisotropic scattering of the amide I Raman band.

The micromechanical elastic properties of lamellar bone have been analyzed in previous studies using nanoindentation (NI) [37–39] and scanning acoustic microscopy (SAM) [7, 8, 40]. Both methods revealed periodically oscillating modulations of the measured elastic properties (i.e. indentation modulus and acoustic impedance for NI and SAM, respectively) across bone lamellae. Several approaches aimed at correlating the observed micro-mechanical undulations (i) to variations of the tissue composition and/or based on the transverse isotropic mechanical properties of mineralized collagen fibrils (ii) to changes of the fibrillar orientation. A combined quantitative backscattered electron imaging (qBEI) and NI study [39] suggested locally varying mineral contents in osteonal lamellae and concluded that both compositional variations and varying fiber orientations contributed to the oscillating mechanical properties. Intralamellar variations of the distribution of mineral particles were also observed in a backscattered electron microscopy analysis [41]. Contrary to these observations, experimental evidence of the homogeneity of the lamellar composition was presented by means of PRS [7, 24, 42] and synchrotron X-ray phase nano tomography (SR-nanoCT) [13]. Recently, a correlative approach using SAM, SAXS, and synchrotron X-ray micro tomography [8] proposed a predominant determination of the modulated apparent elastic properties by variations of the fiber orientation in single osteons and to a lesser extent by variations of the mineral particle size and density. However, these propositions are in contrast to the findings of another study based on combined qBEI, NI, and quantitative polarized light microscopy measurements [43]. Interestingly, the authors of the latter approach observed no substantial correlation of indentation moduli with mineralization and fiber orientation. The variety of different proposals on the link between micromechanical properties, structural fiber arrangement, and chemical composition underlines the difficulty in analyzing the structure-function relationship of lamellar bone tissue at the micron length scale.

The present thesis explored interplaying tissue properties of human cortical lamellar bone on the micron length scale. The research aimed at the following

major objectives:

- The first objective was to analyze the organization of collagen fibrils in lamellar bone by means of PRS to demonstrate that, in addition to the tissue composition, PRS is capable of simultaneous deciphering of intricate 3D microarchitectures. In particular, the specific fibrillar orientation patterns of single lamellae and the predominant fibril directionalities of entire tissue domains were investigated.
- By proposing a novel multimodal approach, combining PRS, SAM, synchrotron X-ray phase contrast micro tomography (SR-µCT) and SR-nanoCT in a site-matched study design, it was aimed to investigate the relationship between local interaction of structure, composition and micromechanics at two hierarchical levels (i.e. single bone lamellae and entire tissue domains) and in regions of different tissue maturity.
- Furthermore, the thesis aimed to validate the PRS estimated fibril orientation by means of SR-nanoCT.

Finally, besides the investigation of healthy bone, the last objective of this thesis focuses on the analysis of pathological bone. Neurofibromatosis type 1 (NF1) is a genetically determined bone disorder causing severe skeletal abnormalities, including impaired mechanical tissue properties in long bones.

- To elucidate the role of Nf1 in the development of long bones, conditional mouse mutants characterized by Nf1 ablation in different mesenchymal progenitor cells were investigated in an experimental SAM analysis. The aim of the study was to gain a deeper understanding of the Nf1 function and the mechanisms underlying the decreased stiffness values observed in the cortex of long bones.

1.3 Outline

According to the aims and objectives formulated above, this thesis is organized as follows:

Chapter 1 introduces the general context and the motivation behind the thesis. The fascination of the material bone is outlined and the focus of the presented research is defined. Furthermore, the specific objectives of the thesis are described in detail.

Chapter 2 describes the state of research with regard to the experimental studies carried out within the frame of the thesis. Bone's basic components

are introduced and the hierarchical structure of the material is explained. In particular, the lamellar structure of cortical bone and the fibril arrangements in bone lamellae are discussed. Following this, the technologies applied in the experimental studies, PRS, SAM and SR-μCT/SR-nanoCT are introduced and set into the context of other prominent methodologies commonly applied in bone research. The theoretical basis of each technique is provided and applications on bone tissue important for the focus of this thesis are summarized.

Chapter 3 presents the experimental studies of this thesis. In the first study (Sec. 3.1), PRS was applied to simultaneously analyze structural and compositional aspects of human lamellar bone tissue. Different parameters in Raman spectra correlated to the fibril orientation in the plane perpendicular and parallel to the laser polarization were identified. Analysis of the lamellar organization patterns was supported by theoretical models.
In a second approach (Sec. 3.2), PRS analysis was combined with SR-μCT, SR-nanoCT, and SAM measurements. In a site-matched manner, collagen fibril orientation, microelastic properties, tissue composition, mineral maturity, and mass density were spatially correlated. Computational simulations were employed to verify the experimental outcome. Using kernel density estimation on Raman data of entire tissue domains, predominant fibril orientations and coexisting fibril patterns were determined. Moreover, the fibril orientation estimation provided by means of PRS and SR-nanoCT were compared.
The last experimental study (Sec. 3.3) focused on the analysis of the role of the neurofibromin (Nf1) gene mutation in the development of the bone matrix stiffness. SAM measurements on different conditional mouse mutants featuring Nf1 ablation were compared to wild types.

Finally, in chapter 4, a conclusion of this thesis work and an outlook is presented.

2

State of the Art

2.1 Bone

2.1.1 Chemical Composition

The major components of bone are [44–47] :

- **50 – 60 wt.% inorganic phase** consisting of **mineral particles** in the form of carbonated hydroxyapatite (hAp) nanocrystals,
- **30 – 40 wt.% organic phase**, predominantly consisting of **type I collagen** (~90%) and a small contingent (~10%) of non-collagenous proteins (NCPs) (e.g., osteonectin and osteopontin),
- **10 – 20 wt.% water** in free form and bound to both crystals and collagen molecules, located in intra- and extrafibrillar spaces.

The mineral phase of bone is calcium phosphate in a structure closely related to hAp. Bone mineral is impure and contains significant amounts of carbonate (~5 wt.%) and ions (Mg, Na, F, Cl), which replace Ca, PO_4^{-3} and OH in the crystal lattice. In addition, significant portions of citrate (~2 wt.%) were found, and evidence of citrate adsorption to the crystal surface was provided [48]. Due to lattice substitutions, small crystal dimensions and/or amorphous calcium phosphate phases associated to hAp, bone mineral particles are considered poorly crystalline [49].

Mineral particles feature a plate-like shape with an average thickness of 1.5 - 4 nm, a length of 15 - 200 nm, and a width of 10 - 80 nm [50–52]. The collagen type I molecule, also called tropocollagen, is wound together into a triple helical structure and has a length of ~300 nm and a diameter of 1.24 nm [53, 54] (Fig. 2.1a). In bone, collagen is organized in arrays of parallel-oriented molecules that form long, cylindrical fibrils with a diameter of 80 - 120 nm [19]. The molecules are staggered by 67 nm. As a result, an overlap region of 27 nm length and a 40 nm gap region between adjacent collagen molecules can be observed (Fig. 2.1a). Enzymatic and non-enzymatic intermolecular cross-links [55, 56] and hydrogen bonds [57] within and between

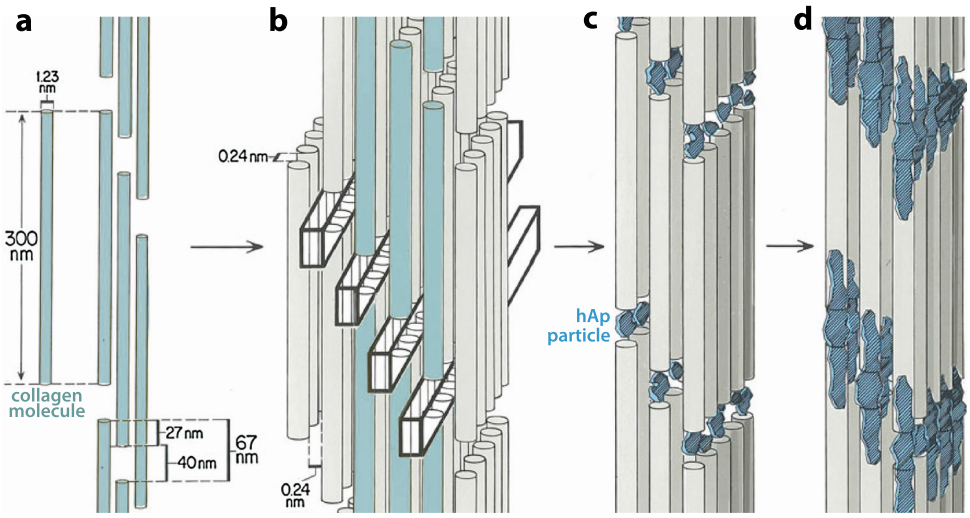

Figure 2.1: Schematic of the progressive formation of mineralized collagen fibrils. (a) Dimensions of a single collagen molecule and staggered 2D collagen molecule array displaying the characteristic gap (40 nm) and overlap (27 nm) regions of collagen fibrils. (b) 3D model illustrating the molecule packing in collagen fibrils. (c) Intrafibrillar nucleation of hAp particles in collagen gap regions. (d) Formation of nanoplatelets as a result of mineral crystal growth out of the gap regions. Image reprinted from [62] with permission from Elsevier.

fibrils stabilize the structure. Mineral particles form after the assembly of collagen fibrils. Evidence has been provided that the nucleation and growth of the mineral particles is initiated in the gap region of collagen fibrils (Fig. 2.1c), extending with growth into the overlap regions [51, 58](Fig. 2.1d). Additionally, extrafibrillar mineral growth on the fibril surface has been observed [59, 60]. Both intrafibrillar and surface attached mineral crystals grow with their c-axis parallel aligned with the longitudinal axis of the collagen fibrils [60, 61]. Together, collagen molecules and mineral particles form mineralized collagen fibrils (MCF), the basic building block of bone material.

The relative proportions and assembly motifs of bone constituents into structures of higher order depend on a multitude of factors, such as species, anatomical location, age, sex, and bone type.

2.1.2 Hierarchical Structure

Lamellar bone features a complex 3D hierarchical organization at several structural levels ranging over various length scales from single molecules to entire bones. The following condensed definition of these levels is based on the schemes proposed by Weiner and Wagner [45], Rho et al. [5], Fratzl et al. [51], as well as recent updates by Reznikov et al. [21, 63] and Varga et al. [13].

- The major **components**, **type I collagen fibrils**, **carbonated hAp crystals**, and **water molecules** are considered the first level of hierarchy at the (sub-) nanometer scale

- The joint structure of **mineralized collagen fibrils** represents the second level of hierarchy.

- The majority of mineralized collagen fibrils are organized in **ordered arrays of parallel-aligned fibrils**, representing the next level of structural hierarchy. However, a small fraction of fibrils are present in a **disordered** form and exhibit little or no preferential orientation.

- The fibril arrays are arranged in specific **array patterns** at the submicrometer and micrometer level. A diversity of different structural patterns between bone tissues is known. The most common one is the **lamella**, a planar layered structure of bone tissue. The majority of current studies describe the lamella as staggered arrays of sublayers (sublamellae), each consisting of arrays of unidirectional aligned fibrils. The fibrils of each sublayer have a distinct angle of twist φ (Fig. 2.2b).

- At the micrometer and submillimeter scale, lamellae are arranged in repetitive stacks; in human bone either in a circumferential fashion around a vascular canal forming **osteons** (Fig. 2.2a) or quasi-parallel in struts, so-called **trabeculae**.

- At the next structural level, **compact cortical tissue** forming the outer shell of bones and **spongy trabecular tissue**, which partially fills the shell volume, is distinguished. In humans, cortical bone is formed by osteonal tissue and is characterized by low porosity (<10%). In contrast, trabecular bone consists of trabeculae and plates organized in a loose network and features high porosity (~80%) and a wide surface area.

- Lastly, on the macroscopic level, the **whole bone organ** represents the highest level of structural hierarchy.

Within the scope of this thesis, tissue properties at several levels of bone structural hierarchy were investigated. In particular, osteonal and lamellar structural design and resulting mechanical properties were elucidated. Therefore, these structures are described in closer detail in the following subsection. A schematic sketch of the osteonal and the lamellar tissue architecture is displayed in Fig. 2.2.

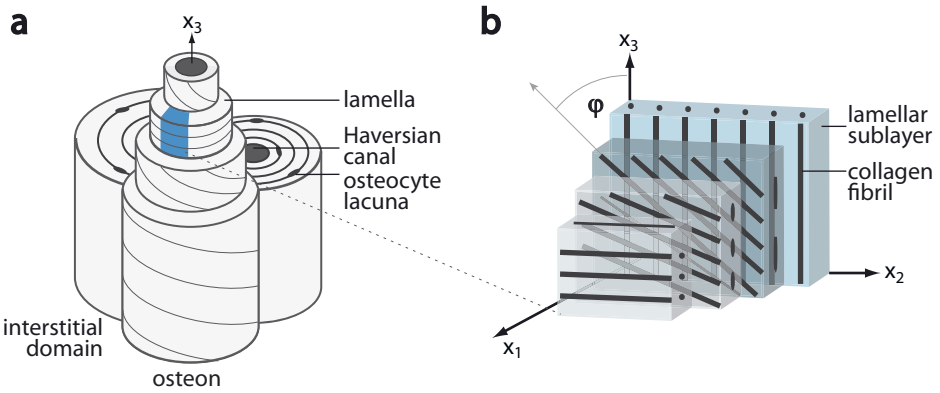

Figure 2.2: Lamellar architecture of bone. (a) Schematic sketch of osteons formed by lamellae concentrically disposed around a central Haversian canal and osteocyte lacunae. Adjacent remnants of older osteons are called interstitial tissue domains. (b) Illustration of a single lamellae. The fibrils of the lamellae are organized in parallel sublayers consisting of unidirectional aligned collagen fibrils. The fibril orientation follows specific organization patterns. The x_2x_3 plane is the lamellar plane; x_1 is the axis perpendicular to the lamellar plane.

Osteonal and Interstitial Tissue Domains

Osteons are cylindrical structures with a diameter of approximately 150 – 250 µm. The central vascular canal (Haversian canal) features a diameter of approximately 50 µm [64] (Fig. 2.2a). In long bones, the majority of osteons is parallel aligned with the bone long axis. The central canal is wrapped by 4-20 lamellae and bordered by a circumferential wall called the cement line to the surrounding tissue [5]. Osteons are interspersed by ellipsoidal cavities (diameter ~ 5 - 10 µm), so-called lacunae, which house the osteocytes. Osteocytes are bone cells that are involved in routine ion metabolism processes of bone matrix. Moreover, osteocytes are assumed to fulfill mechanosensory functions and to orchestrate bone remodeling [65, 66].

Osteons are embedded in interstitial domains, remnants of the initially built general lamellae or older osteons that have been partially resorbed and replaced during bone remodeling. Like osteons, interstitial domains are structures of quasi-parallel periodic layered lamellae. However, due to their increased tissue age, interstitial domains exhibit on average a higher degree of mineralization, stiffness and an increased level of mineral maturity than directly adjacent osteons [67–69]. It is worth noting that due to the coexistence of young osteonal and older interstitial tissue domains, bone matrix displays strong heterogeneities regarding tissue age, mineralization, and stiffness at the micrometer scale.

Bone Lamellae

As stated above, bone lamellae are layered structures of fibril arrays arranged in specific patterns (Fig. 2.2b). Typically, lamellae feature a width of 3 - 7 µm. The micro-architecture of bone lamellae has been analyzed in numerous studies by means of a wide range of different techniques. Surprisingly, experimental observations were conflicting and consequently structural conclusions about the fibrillar organization were partially or fully contradictory. Thus, some basic questions about the lamellar architecture still remain unresolved and the detailed structure and implied mechanical consequences are not yet fully understood.

Early investigations of the fibril patterns in osteonal lamellae go back to Gebhardt [70] who suggested that individual lamellae are constituted of unidirectional aligned fibrils and assumed an abrupt change of orientation of 90° between adjacent lamellae. Ascenzi and Bonucci [14, 71] hypothesized that each lamellae consists of mainly longitudinal, transverse, or alternating fibril orientations. In contrast, Marotti [17] described the lamellar unit as a disordered structure of interwoven fibrils periodically arranged in collagen-rich dense and collagen-poor loose layers.

Recent studies have contradicted these first findings and provided evidence about much more complex fibril arrangements in bone lamellae. Generally, consensus was reached that single lamellae are composed of numerous sublayers, each characterized by unidirectional aligned fibrils. The fibrils of each sublayer feature a distinct angle of twist in the lamellar plane and with respect to the osteonal axis, which varies according to the location of the sublayer across the lamellae. Idealized models, precisely describing the fibrillar pattern of bone lamellae, were established in these studies. However, striking differences considering discrete or continuous fibrillar transition between sublayers, maximum angular deflection with respect to the osteonal axis, and sublayer thickness were reported.

(i) Giraud-Guille [16] proposed the **twisted plywood pattern** as the predominant and repetitive organization motif. Her proposition was based on the observation of arching structures in transmission electron microscopy (TEM) images of obliquely cut osteons (Fig. 3.8a). The twisted plywood structure is characterized by a smooth, continuous, and full fibril rotation in the lamellar plane. The pattern has been confirmed by various recent studies [13, 63].

(ii) Giraud-Guille's concept was modified by the proposition of an **asymmetrical rotated plywood pattern** composed of five unidirectional sub-

layers of varying thickness and discrete, specific fibrillar transitions of 30° between adjacent sublayers by Weiner et al. [4, 19].

(iii) Wagermaier et al. [22] suggested a **helicoidal plywood structure** with a spiral twisting fibril orientation.

(iv) Recently, the concept of an **oscillating plywood** arrangement has been introduced [13], characterized by twist angles that smoothly oscillate around the osteon axis x_3 and exhibit a distinct maximum angular deflection significantly smaller than 90°. It is worth noting that these oscillating plywood patterns were observed **coexisting with twisted plywood patterns** in a consecutive manner. Interestingly, in these experiments single sublayers with partial randomly oriented fibrils were observed.

(v) More recently, Reznikov et al. [20, 21, 63] have presented novel findings that unite several of these model descriptions: bone lamellae with both twisted and oscillating arrangements were observed that consisted of **ordered phases** (mainly aligned fibrils) and **disordered phases** (proportions of randomly oriented fibrils, less densely packed).

2.1.3 Bone Remodeling

Bone is a dynamic living tissue and features the unique ability to adapt to changing spatial and temporal external stimuli [2, 3, 72]. Furthermore, it has the capacity to self-heal damage to the bone matrix. Under healthy conditions, a balanced interplay of resorption and subsequent formation of bone matrix is observed. Osteoclasts, large bone-resorbing macrophages, disassemble and digest bone mineral and organic phases by secreting acid and collagenase, respectively. Their antagonists, the osteoblasts, are responsible for new bone formation in the resorption cavities created by the osteoclasts. They initially lay down osteoid, the unmineralized organic matrix and basis of new osteons. Additionally, osteoblasts control the progressive mineralization process of the osteoid. Some osteoblasts differentiate into osteocytes and remain buried in the mineralized matrix.

2.2 Imaging Modalities for Bone Characterization

Over the last decades, an arsenal of different techniques has been applied to investigate structural, chemical, mechanical, and functional aspects of bone material at various length scales. A comprehensive list of prominent modalities qualified for the imaging of bone properties at the micrometer and submicrometer scale is presented in table 2.1. In this summary, the techniques used for the experimental investigations of this thesis (marked in blue) are compared to alternative tools, and major advantages and drawbacks of each modality are pointed out. The methods applied in this thesis are described in closer detail and their physical background is provided below.

2.2.1 Raman Spectroscopy

Raman spectroscopy is a vibrational spectroscopic technique and has been proven to be a versatile characterization tool in biomaterial research. It is employed to elucidate the molecular structure based on characteristic vibrational transitions [99, 100]. Raman scattering is a two-photon scattering process. Due to the interaction of the incident laser light with the polarizability of a molecule, a dipole moment is induced. This dipole moment emits radiation that contains Rayleigh and Raman scattered photons. Rayleigh scattering is an elastic process and scattered photons have the same energy as incident laser photons. In contrast, Raman scattering is an inelastic event and Raman radiation is shifted with respect to the incoming laser light (Fig. 2.3). This energy shift is represented in Raman band spectra and provides information about characteristic molecular vibrational modes, enabling identification of specific chemical vibrational units and corresponding molecules.

Raman spectroscopy offers a range of advantages for imaging of biological systems: one of the major benefits in biomedical applications of Raman spectroscopy in comparison with other techniques and in particular with infrared spectroscopy is that Raman does not require elaborate sample preparation and can be applied to differently prepared specimens, including native samples [78]. Specimens can be examined in hydrated form, as water provides a weak, uncomplicated Raman signal [100]. Moreover, thin sectioning, dehydration, fixation, and embedding are not compulsory, but do not interfere with Raman microspectroscopy [78, 101], which facilitates subsequent measurements with other techniques and even in situ applications. Furthermore, Raman measurements may be extended to fluorescently labeled or stained samples [102, 103]. Finally, as used in this thesis, confocal Raman spectroscopy provides a high spatial resolution ($\leq 1\,\mu m$) and is well suited for non-destructive parameter mapping that can be combined with other measurements in a straightforward way.

Table 2.1: Comparison of prominent techniques used for bone characterization. ***Part 1.*** Techniques marked in blue have been applied in the experimental studies of this thesis. References: LM [73, 74], PLM [17, 70, 75], CLSM [76, 77], RS [24, 36, 42, 78, 79], FTIR [80–82], SEM [17, 18, 41], qBEI [25, 39], EDX [83–85].

Technique	Type of property	Dimen-sion	Reso-lution	Specimen Destruction	Major advantages	Major disadvantages
visible light based techniques						
Conventional light microscopy (LM)	structural information	2D	~1 µm	no	• widely available • fast image acquisition times • component-specific staining and functional imaging possible due to fluorescent labeling	• image blurring due to out-of-focus signals, superimposed lateral image information from multiple depths • in transmission mode thin samples obligatory
Polarized light microscopy (PLM)	structural information	2D	~1 µm	no	• fast image acquisition times • no staining necessary	• thin samples obligatory (control of thickness required for quantitative results)
Confocal laser scanning microscopy (CLSM)	structural information	3D	< 200 nm	no	• component-specific staining and functional imaging possible due to fluorescent labeling	• limited optical penetration in bone (70-100 µm); thin sample sectioning and fluorescent labeling obligatory
vibrational spectroscopic techniques						
Polarized Raman spectroscopy (PRS)	tissue composition, structural information	2D	~1 µm	no	• very simple sample preparation (applicable to various preparation conditions, including in situ settings) • higher spatial resolution than FTIR	• time consuming in mapping mode • peak contributions mainly from major bone components
Fourier transformed infrared spectroscopy (FTIR)	tissue composition	2D	~5-10 µm	no	• superior signal-to-noise-ratio than RS • shorter acquisition times than PRS	• complex sample preparation, thin sectioning obligatory • relatively low resolution • peak contributions mainly from major bone components
electron microscopy techniques						
Scanning electron microscopy (SEM)	structural information	2D	~3 nm	no	• high resolution • easily accessible	• measurements under vacuum conditions • potential radiation damage
Quantitative backscattered electron imaging (qBEI)	tissue composition	2D	~1 µm	no	• relative mineral density quantification	• surface topography of specimen not as accurately resolved as in SEM imaging
Energy dispersive X-ray spectroscopy (EDX)	tissue composition	2D	< 1 µm	no	• qualitative distribution of material constituting elements • high resolution	• potential radiation damage • detection of low-concentrated elements difficult • smooth sample surfaces required

Comparison of prominent techniques used for bone characterization. ***Part 2.*** Techniques marked in blue have been applied in the experimental studies of this thesis. References: FIB-SEM [20, 63], TEM [16–19], lab based desktop µCT [86, 87], SR based µCT [88–90], SR-nanoCT [13, 91], SAXS/WAXD [22, 92, 93], XANES [94, 95].

Technique	Type of property	Dimen-sion	Reso-lution	Specimen Destruction	Major advantages	Major disadvantages
Serial focused ion beam SEM (FIB-SEM)	structural information	3D	~10 nm	yes	• highest resolution in 3D imaging available	• highly time consuming • limited field of view • destructive
Transmission electron microscopy (TEM)	structural information	2D	~1 nm	no	• images with highest resolution available	• complex sample preparation, ultra-thin sample sectioning (10-100nm) obligatory; • measurements under vacuum conditions • limited field of view
X-ray imaging techniques						
X-ray absorptionCT (lab based desktop µCT)	structural information	3D	~1 µm	no	• simple sample preparation • quantification of relative mineral density on the micron scale • nowadays broadly availabe	• high radiation dose • image quality at high resolutions poor (blurring, distortions), due to insufficient photon flux, polychromatic beam, and limitations of the detectors • beam-hardening artefacts
X-ray absorptionCT (SR based µCT)	structural information, mineral density	3D	~ 0.5 µm	no	• simple sample preparation • superior image quality than desktop µCT, due to higher flux and monochromatic beams • quantitative imaging of mineral density	• high radiation dose • requires access to synchrotron radiation facility
X-ray phase nano tomography (SR-nanoCT)	structural information	3D	~120-150 nm	no	• very high resolution 3D imaging • absolute quantification of mass density distribution • simple sample preparation • decreased radiation dose	• requires access to synchrotron radiation facility • intricate and time consuming image reconstruction
Small angle X-ray scattering (SAXS) / Wide angle X-ray diffraction (WAXD)	structural information	2D	~ 1µm	no	• multiple information on orientation, shape, and thickness of mineral platelets in bone	• thin sample sectioning obligatory
X-ray absorption near edge spectroscopy (XANES)	chemical composition, structural information	2D	~ 0.5 µm	no	• characterization of apatite calcium phosphate and calcium carbonate • large field of view • fast image acquisition times	• requires access to synchrotron radiation facility

Comparison of prominent techniques used for bone characterization. ***Part 3.*** Techniques marked in blue have been applied in the experimental studies of this thesis. References: AFM [59, 96], NI [10, 37, 39, 97], SAM [7, 8, 98].

Technique	Type of property	Dimen-sion	Reso-lution	Specimen Destruction	Major advantages	Major disadvantages
Scanning probe microscopy						
Atomic force microscopy (AFM)	structural information/ elastic properties	2D	~20-50 nm	no	• 3D surface profile • mapping of elastic modulus • high image resolution, comparable to SEM no surface coating/vacuum settings required	• time consuming • limited field of view • susceptible to surface artefacts
Mechanical mapping of elastic properties						
Scanning nanoindentation (NI)	hardness/ elastic properties	2D	~1 µm	yes	• characterization of local indentation modulus and hardness on microscale	• derivation of elastic modulus from indentation modulus indirect, requires structural model assumptions • destruction of sample surface • time consuming in mapping mode • limited to relatively small field of view
Scanning acoustic microscopy (SAM)	elastic properties	2D	~1 µm	no	• high sampling rate • large field of view • fast image acquisition times • applicable at various spatial resolutions, investigations of several levels of hierarchy possible	• derivation of elastic properties from acoustic impedance indirect, requires empirical validation or information on material sound velocity/density • complex sample preparation (critical surface polishing) • susceptible to surface artefacts

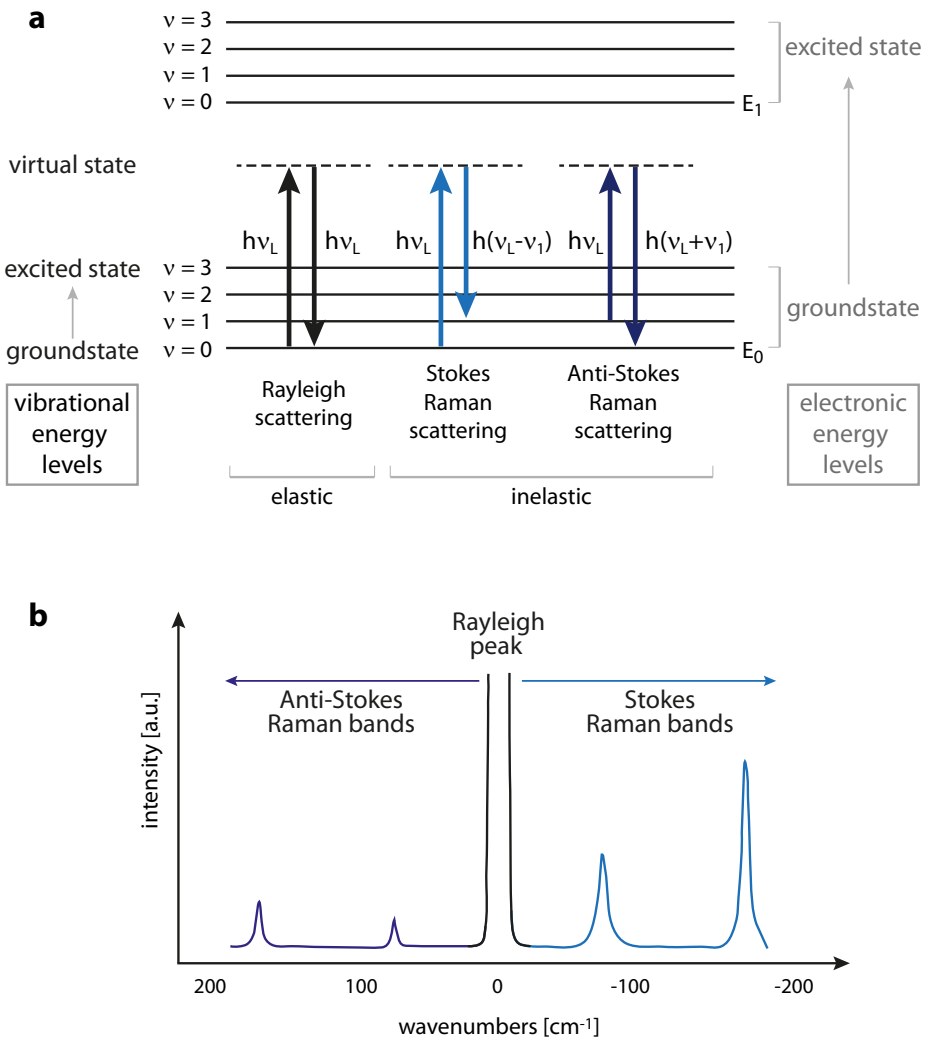

Figure 2.3: Schematic of the molecular energy transitions associated to Rayleigh and Raman scattering. a) In Rayleigh scattering events, a photon interacts with a molecule by polarizing the electron cloud and raising it to a virtual, short-lived energy state. When returning back to the ground state a photon with the same energy as the initial one is emitted. In contrast, Stokes and Anti-Stokes Raman scattering are each associated with the release of a photon with less and more energy than the initial one, respectively. (b) The three scattering processes are represented in the characteristic peaks of Raman spectra. The intensity of the Raman peaks reflect the probability of the energy transition.

However, there are several major limitations to Raman spectroscopy that need to be mentioned. As the major components mineral phosphate and carbonate, and matrix collagen dominate the spectra, investigations of minor constituents such as lipids and NCPs are problematic [103]. Especially, the observation of NCP associated Raman signals remains challenging, as a

result of their spectral similarity to collagen and small proportion in bone composition [104, 105]. Moreover, tissue fluorescence may cause an intense spectral background that can potentially overlap spectroscopic information [106]. Ultimately, due to the small fraction of Raman scattered light, Raman acquisition times are comparably longer than those typically needed for infrared spectroscopic measurements [78, 107, 108].

Classic Theory of Raman Scattering

As a result of the interaction with the electric field E_L of the laser, an oscillating electric dipole μ is induced in the irradiated molecule [109]

$$\mu = \alpha E_L \tag{2.1}$$

where α is the polarizability of the molecule. The electric field is an oscillating function

$$E_L(t) = E_0 \cos(2\pi\nu_L t) \tag{2.2}$$

with E_0 being the amplitude of the oscillation and ν_L the frequency of the laser light. Thus, the induced dipole oscillates in phase with the electric field

$$\mu(t) = \alpha E_0 \cos(2\pi\nu_L t). \tag{2.3}$$

The polarizability of the molecule is determined by the molecular geometry, the chemical environment and the vibrational mode. The vibrational displacement q of the n^{th} atom in the molecule is

$$q_n = q_n^0 \cos(2\pi\nu_m t) \tag{2.4}$$

with q_n^0 representing the amplitude of the vibrational displacement and ν_m the frequency of the vibration. The polarizability can be approximated by means of a Taylor series

$$\alpha = \alpha_0 + \sum_n \left(\frac{\partial\alpha}{\partial q_n}\right)_{(q_n=0)} + \frac{1}{2}\sum_{n,j}\left(\frac{\partial^2\alpha}{\partial q_i \partial q_j}\right)_{(q_i=q_j=0)} q_i\, q_j + \ldots \tag{2.5}$$

For small amplitude vibrations, terms higher than second order can be neglected. Combining Eqs. (2.3) and (2.5), the polarizability of a molecule is

$$\begin{aligned}\mu =& \alpha_0 E_0 \cos(2\pi\nu_L t) \\ &+ \frac{1}{2}\sum_n \left(\frac{\partial\alpha}{\partial q}\right)_{(q_n=0)} q_n E_0 \left[\cos(2\pi(\nu_L - \nu_m)t) + \cos(2\pi(\nu_L + \nu_m)\right].\end{aligned} \tag{2.6}$$

The first term in Eq. 2.6 represents an oscillating dipole that emits photons with a frequency ν_L and is related to elastic Rayleigh scattering. The second term corresponds to Raman scattering at a frequency of $(\nu_L - \nu_m)$ and $(\nu_L + \nu_m)$

representing Stokes Raman and Anti-Stokes Raman scattering, respectively. It is worth noting that only vibrational modes that involve a change of polarizability are Raman active [109].

$$\left(\frac{\partial \alpha}{\partial q}\right) \neq 0 \tag{2.7}$$

Polarized Raman Spectroscopy

In addition to providing chemical material information, Raman spectroscopy is inherently sensitive to the orientation of molecules. By capitalizing on the anisotropic Raman scattering at different polarization angles of the incident laser light, Raman spectroscopy provides information on molecular arrangements.

Polarizability Tensor and Raman Tensor

The electric dipole moment $\vec{\mu}(t)$ and the electric field $\vec{E_L}(t)$ are vector quantities. In the previous subsection, the polarizability was assumed to be scalar. Note that this holds true for spherical symmetric polarizability only. For non-isotropic molecules, the magnitude of the induced dipole moment depends on the angle between the electric field vector E_L and the differential polarizability [110]

$$\vec{\mu} = \alpha \vec{E} \tag{2.8}$$

with α representing the second-rank polarizability tensor. As a result, directional information about the polarizability and thus about the orientation of the molecule can be obtained when polarized laser light is applied [110]. The so-called Raman tensor α' is defined as the first derivative (with respect to the vibrational normal coordinate) of the polarizability tensor and is unique for each Raman active vibrational mode [111]. In other words, the Raman tensor describes how the polarizability of the molecule oscillates with the normal mode of vibration [112]. The correlation of these parameters and their impact on the measured intensity of Raman scattered light are mathematically derived in this subsection.
Using Maxwell's equation, the electric field E_S of the scattered radiation at a distance r can be defined as

$$\vec{E}_s(t) = 4\pi^2 \left(\frac{\nu_s^2 \vec{\mu}(t)}{r}\right) \sin\phi \tag{2.9}$$

with ν_S being the frequency of the scattered radiation and ϕ the angle between dipole axis and scattered radiation. The intensity of the scattered radiation is

$$I_s = \left|E_s(t)\right|^2 r^2 = 16\pi^4 \nu_s^4 \left|\alpha^2\right| \left|E_L\right|^2 \sin\phi. \tag{2.10}$$

Using Eqs. 2.5 and 2.6 and the Raman tensor for Stokes Raman scattering, the intensity I_{Stokes} of the scattering event can be estimated as

$$I_{Stokes} = \frac{2^4\pi^4}{3^2c^3} |E_L|^2 (\nu_l - \nu_m)^4 \sum_{ij} |\alpha'_{ij}|^2 . \tag{2.11}$$

Note that I_{Stokes} is the intensity summation over a solid angle of 4π. However, if an analyser is introduced in the Raman microscope, specific polarizations of the scattered light can be detected. By analysing anisotropic Raman intensities, spectra can provide further information about the Raman tensor of specific vibrational units. Consecutively, Eq. 2.11 can be simplified for polarized Raman scattering $I_{Stokes\circ}$ (scattering per solid angle) to the following equation that considers the polarization directions of the incident laser light and the Raman scattered light [110]

$$I_{Stokes\circ} = I_0 \left| l_{p'} \, \alpha' \, l_p \right|^2 \tag{2.12}$$

with p and p being the polarization directions of laser and analyzer, respectively, l_p and l'_p the direction cosines of incident and Raman scattered light and I_0 representing the summary of constants in Eq. 2.11. Eq. 2.13 defines the intensity of a single Raman scattering molecule. The intensity $I_{Stokes\circ}$ of all molecules within the irradiation volume of the sample is

$$I_{Stokes\circ} = I_0 \sum \left| l_{p'} \, \alpha' \, l_p \right|^2 . \tag{2.13}$$

This relation is the basis for the analysis of the anisotropic amide I Raman band scattering and the corresponding information about the orientation of collagen molecules in bone material investigated in this thesis.

Raman Investigations of Bone Tissue

Within the last years, the application of spatially resolved vibrational spectroscopy on bone tissue has increased remarkably. Raman spectroscopy and Fourier transformed infrared spectroscopy provide the advantage of gaining complementary information about the chemical composition, the molecular state, the maturation, and the organization of bone and other biological tissues.

A representative Raman spectrum of a human cortical bone tissue section is shown in Fig. 2.4. The main contributions in the spectrum arise from the inorganic mineral phase and the organic collagen phase. Prominent bands associated to hAp include: the most intense band in bone spectra, the phosphate ν_1 PO_4^{-3} peak (symmetric stretch at ~ 960 cm^{-1}), the phosphate ν_2 PO_4^{-3} peak (symmetric bending at ~ 440 cm^{-1}), and the ν_4 PO_4^{-3}

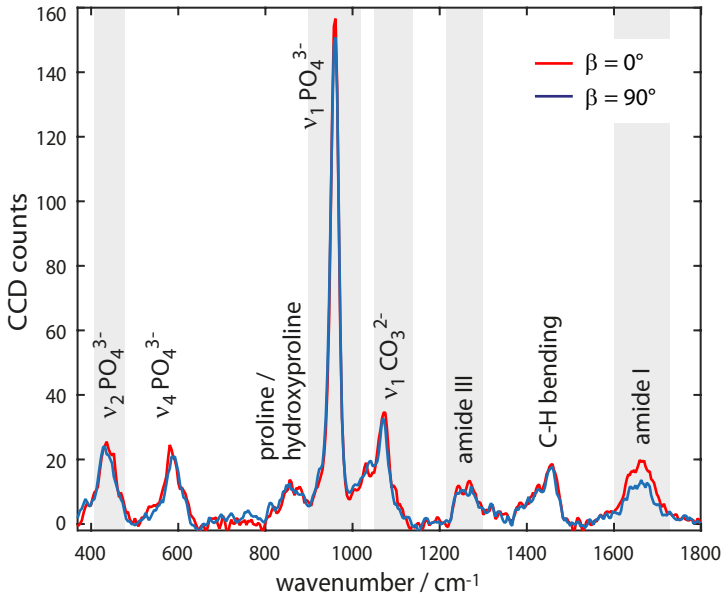

Figure 2.4: Typical Raman spectrum of a cortical bone sample measured at different polarization angles of the incident laser. Raman peaks associated to the collagen and mineral phase of bone are indicated. Bands investigated as a part of this thesis are marked in gray.

peak (asymmetric bending at ~ 590 cm^{-1}). Another hAp associated band is carbonate ν_1 CO_3 $^{-2}$ (symmetric stretch at ~ 1070 cm^{-1}). Important Raman bands reflecting on the organic matrix are the amide I (C=O stretch at ~1660 cm^{-1}) and the amide III band (C-N vibration and C-O stretch at ~ 1240 - 1270 cm^{-1}), which mainly represent the peptide bonds within the backbone of the collagen molecule. The C-C stretching vibrations of proline (at ~ 855 cm^{-1}) and hydroxyproline (at ~875 cm^{-1}) are collagen markers as well. The C-H bending deformation (at ~ 1458 cm^{-1}) is a general marker of protein content, which can reflect on collagen, NCPs, and PMMA in bone spectral analysis. A detailed register of the bone Raman bands is listed in table 2.2.

Investigations of Bone Chemistry

Raman spectroscopy enables assessment of several important tissue parameters related to the description of bone quality [78]. These parameters include: the mineral-to-matrix-ratio (MTMR), the carbonate-to-phosphate-ratio (CTPR), the mineral crystallinity, collagen maturity, and acid phosphate. The tissue parameters investigated within the frame of this thesis are introduced in this subsection.

Table 2.2: Raman band assignments for human cortical bone. Bands investigated within the framework of this thesis are highlighted in blue.

Raman shift / cm^{-1}	Raman band assignment	molecular species
410 – 460	ν_2 PO_4^{-3}	anorganic hAP
590	ν_4 PO_4^{-3}	anorganic hAP
854	hydroxyproline	organic collagen
878	hydroxyproline	organic collagen
920	proline	organic collagen
960	ν_1 PO_4^{-3}	anorganic hAP
1002	phenylalanine	organic collagen
1070	ν_1 CO_3^{-2}	anorganic hAP
1215 - 1290	amide III	organic collagen
1300	CH_2 deformation	lipid
1439	CH_2 deformation	lipid
1448	CH_2 deformation	organic collagen
1610 -1700	amide I	organic collagen
1745	C-O	lipid
2880 - 2980	C-H stretching	lipid
broad band ~3500	H_20	water

The MTMR is a frequently used compositional indicator of the relative mineral content in bone. It denotes the ratio of integrated peak areas / peak intensities of a mineral and an organic phase representing band and can be analyzed to investigate spatial variations in tissue composition within individual samples and series of related specimens. The potential of MTMR in describing relative bone tissue mineralization was demonstrated in different validation studies: Pienkowski et al. [113] and Boskey and Mendelsohn [23] showed that infrared spectroscopically determined MTMR is strongly correlated with the ash weight of bone. Moreover, Roschger et al. [25] recently provided proof of the link between MTMR and the Ca content (wt. % Ca) in bone in a combined Raman and qBEI approach. Their measurements demonstrated a strong linear correlation (R^2=0.75) between MTMR and wt % mineral/(100-wt. % mineral) obtained by qBEI.
There are several Raman bands that have been used for calculation of MTMR so far. The most relevant mineral phase reflecting bands included the phosphate bands ν_1 PO_4^{-3}, ν_2 PO_4^{-3}, and ν_4 PO_4^{-3}, whereas important organic phase representing bands comprised the collagen bands amide I, amide III and proline/hydroxyproline. The different bands were chosen for reasons of embedding or instrumentation [78]. Recently, Kazanci et al. [24] demonstrated that several of these peaks, in particular ν_1 PO_4^{-3} and amide I strongly depend on the orientation and organization of mineral particles and collagen fibrils. As a result, consideration of these bands for material composition analysis might lead to incorrect conclusions. The authors provided proof that other bands such as ν_2 PO_4^{-3} and amide III exhibit minimal susceptibility to tissue organization and orientation effects, better qualifying them for compositional analysis.

The CTPR is a measure of the carbonate type-B substitution in phosphate positions of the hAp lattice. Similar to MTMR, Raman bands exhibiting minimal orientation dependency are best suited for analysis of carbonate substitution. Thus, the CTPR is optimally calculated by dividing ν_1 CO_3^{-2} and ν_2 PO_4^{-3} peak areas or intensities [24]. Validation of the spectroscopic analysis of carbonate content in bone composition was provided by investigations of synthetic carbonated apatite crystals [114, 115]. In their study of synthetic apatites with increasing carbonate content, Ou-Yang et al. [114] showed that spectroscopically calculated CTPR are linearly and positively correlated with analytically determined ratios (R^2=0.99). Raman measures of CTPR can provide valuable insights into the chemical composition of calcified tissues, as variations of the parameter with tissue type (enamel, dentine, bone) [26], age [27, 116], mineral crystallinity, and even history of fracture [117] have been demonstrated.

Closely related to CTPR is mineral crystallinity, a tissue marker reflecting the orderliness of the hAP crystals and the mineral crystal size. Several investigations demonstrated that the mineral crystallinity is spectroscopically reflected in the bandwidth of the phosphate ν_1 PO_4^{-3} peak and can be assessed by calculating the FWHM [27, 118] or the inverse FWHM [119, 120] of the Gaussian fitted phosphate ν_1 PO_4^{-3} band. Raman investigations of synthetic apatites showed that increased crystallinity, reflected in reduced carbonated substitution levels (i.e. reduced CTPR), yielded narrower phosphate ν_1 PO_4^{-3} bandwidths [114, 115]. Furthermore, validation with X-ray diffraction on different apatic specimen (including human bone, buffalo enamel, and hydroxyapatite) and synthetic apatites showed that the crystallinity is positively correlated with the length of the mineral particle c-axis [118, 121, 122]. However, it is worth noting that the range of bandwidths possible for each given tissue type was comparably small (approximately $1 - 3$ cm^{-1}), thus the parameter precision was rather low [78]. Nevertheless, significant differences in crystallinity have been shown as a function of animal age, despite increasing carbonate substitution levels, most likely due to increasing crystal length [80, 118, 119]. Interestingly, in osteoporotic bone, an increase in crystallinity accompanied by an decrease in MTMR and increased in CTPR was observed [23, 123, 124].

Investigations of Bone Structure

Despite the tissue parameters reflecting chemical and physicochemical aspects of bone material, Raman spectroscopy has been proven to be a useful and increasingly popular tool in providing orientation information on mineral and organic phases in highly structured materials such as bone, tendon, and teeth.

Based on the inherently polarized incident laser light and the polarization-dependent molecular polarizability (Sec. 2.2.1), individual Raman band intensities are dependent on dual influence of composition and structure. Thus, significant modulations of Raman peak intensities can be observed with changing polarization angle of the incident laser light [24, 30–34]. As a result, compositional analysis based on orientation susceptible bands is highly critical, and particularly single point measurements cannot describe the heterogeneous composition of bone adequately. However, recent studies have demonstrated that the polarization-dependent intensity anisotropy can be employed to enrich compositional data with structural information on the orientation of collagen fibrils and mineral particles.

One of the major research focuses of this thesis is the assessment of the collagen orientation in bone by means of polarization-dependent amide I peak

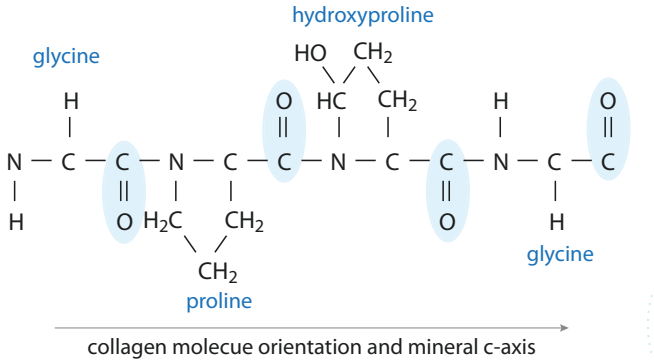

Figure 2.5: Collagen molecule sequence. It is worth noting that the C=O bonds (amide I), marked in blue, are perpendicular to the backbone, while C–N bonds (amide III) are both in the backbone and perpendicular to it. Adapted from [24] with permission from Elsevier.

analysis. Therefore, the molecular structure of collagen, the corresponding amide I Raman tensor, and the theoretical background of anisotropic amide I Raman scattering are briefly reviewed in the following subsection.

A schematic sketch of a typical sequence of the collagen molecule is depicted in Fig. 2.5. The amide I band is mainly associated with the C=O stretching vibration of the trans peptide group (CONH) [125]. Note that the C=O double bond is oriented perpendicular to the backbone of the collagen molecule [24]. The Raman tensor of amide I was established by Tsuboi and Thomas [111] based on experiments on a single crystal of the dipeptide aspartame. The authors proposed that the tensor could be transferred to complex multipeptides. Following this approach, Galvis et al. [36] derived the corresponding amide I Raman tensor for collagen-like peptide molecules with multiple peptide units. Using classic Raman theory they predicted the amide I scattering intensity of these collagen-like molecules as a function of the molecular orientation with respect to the orientation and polarization of the incident laser light. The collagen-like molecules exhibited a sinusoidal anisotropic Raman response when oriented in the plane perpendicular to the incoming laser beam (in-plane orientation), with Raman scattered light being maximal when the polarization of the laser was perpendicular to the molecule orientation and minimal when parallel. The amide I Raman scattering became isotopic, when the molecular orientation was parallel to the incoming laser beam (out-of-plane orientation) (Fig. 2.6) [36]. Experimental validation on rat tail tendon (RTT) was in good agreement with the theoretical results.

In contrast, the amide III band encompasses vibrations from different molecular units, with major contributions from N-H bending and C-N stretching vibrations of the peptide group. Due to contributions of components ori-

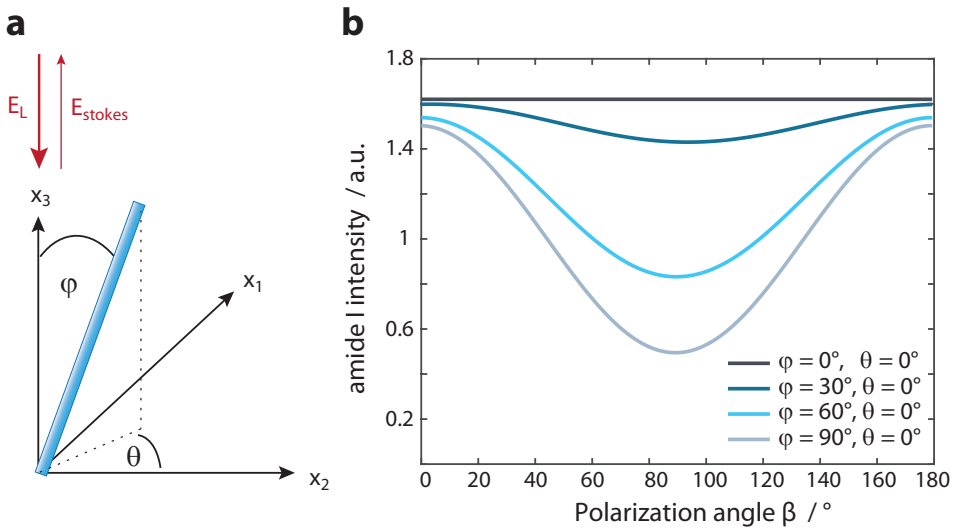

Figure 2.6: Theoretical amide I intensity of collagen-like peptide molecules. (a) Schematic of molecule orientation. (b) Theoretically estimated amide I response at varying molecular orientation φ.

ented parallel and perpendicular to the molecule backbone (Fig. 2.5), Raman amide III scattering is orientation independent. However, it should be kept in mind that orientation independency is observed only if the whole amide III signal is analyzed [24, 126].

To date, several studies have been performed to clarify and exploit the orientation effects of Raman bands associated with the orientation of collagen and mineral phase in bone and other structured biomaterials: Kazanci et al. [24] systematically analyzed the orientation dependency of collagen and mineral associated bands in human bone and were the first to propose bands qualified for compositional analysis with minimal orientation susceptibility. Similarly, Janko et al. [29] investigated the orientation dependency of collagen associated bands in Raman spectra of rat tail tendon (RTT). Hofmann et al. [7] combined Raman measurements with SAM and NI experiments and proposed a link between collagen orientation and elastic stiffness of human cortical bone tissue. Gamsjaeger et al. [30] studied variations of bone composition collagen orientation in murine cortical bone as a function of animal age. Recently, Falgayrac et al. [31] simultaneously investigated the orientation of collagen fibrils and apatite crystals in human cortical bone, based on ν_3 PO_4^{-3}/ν_1 PO_4^{-3}, amide III (1271 cm^{-1})/amide III (1243 cm^{-1}), and amide I / amide III (1243 cm^{-1}) Raman band ratios. Their findings indicated simultaneous tilting of collagen molecule and mineral crystal orientations. Finally, Masic et at. [35] exploited the anisotropic amide I scattering to study the impact of loading on the collagen molecule orientation in the fibrillar crimp

region of RTT.

2.2.2 Scanning Acoustic Microscopy

Over the last two decades, scanning acoustic microscopy (SAM) has become a valuable analytical tool in bone research. It allows for a fast characterization of the elastic properties of bone at a high lateral resolution. SAM is based on the measurement of the linear elastic response of the probed material, which is locally deformed by a high-frequency ultrasound pulse. In previous studies, SAM has been successfully applied to measure the apparent elastic properties of bone tissue at several length scales [67, 98, 127]. Consistent with nanoindentation approaches, acoustic microscopy allows for imaging of the undulating elastic properties characteristic for lamellar cortical bone [7, 8, 40]. Since the acoustic impedance assessed by SAM is highly correlated with the indentation modulus measured by nanoindentation [7, 128], SAM is becoming more and more competitive in mechanical studies of bone tissue.

In addition to fast image acquisition, the major advantage of SAM is the non-destructive mapping in a relatively large field of view, enabling consecutive imaging with other methodologies. Though on the other hand, the acoustic impedance cannot be directly linked to elastic properties without empirical validation. In contrast to SAM, nanoindentation measurements assess the mechanical properties (hardness and elastic modulus) of isotropic materials directly. However, bone is an anisotropic material and its mechanical properties depend on the testing direction. Therefore, in bone studies, the parameter derived by nanoindentation is referred to as the indentation modulus [39, 129]. In combination with structural models, the indentation modulus can be converted into the elastic modulus [10, 130, 131].

Acoustic Theory

Ultrasonic waves are mechanical waves propagating through a medium (fluid or solid) with frequencies above 20 kHz. They are defined by spatial and temporal displacements of particles from their equilibrium position due to mechanical perturbation, leading to a periodic change in pressure, density, and temperature that is gradually transmitted through the medium. The particle displacement can be either in the direction parallel or perpendicular to the direction of wave propagation, causing longitudinal (compressional) or transverse (shear) waves (Fig. 2.7a,b), respectively. Compressional waves can be generated in both fluids and solids, whereas shear waves can propagate in solid materials only. In addition to these two types of waves, surface (Rayleigh) waves (Fig. 2.7c) can propagate between solid and liquid materials [132].

In the following subsections, the acoustic impedance, the output paramter of SAM is defined and its relation to the elastic material properties is briefly

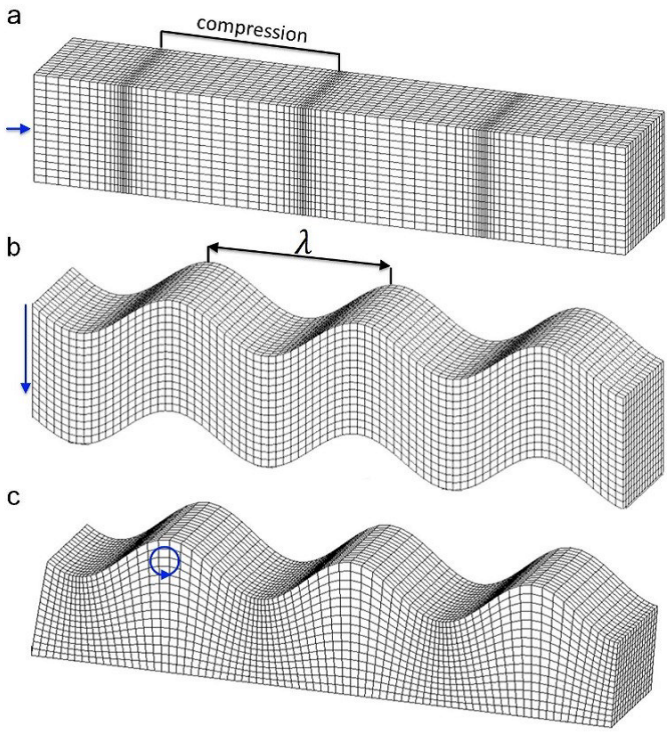

Figure 2.7: Acoustic wave forms. The blue arrows indicate the direction of the particle displacement of each wave form. (a) Longitudinal (compressional) wave, (b) transverse (shear) wave, (c) surface (Rayleigh) wave. Image reprinted from [133].

outlined. With regard to the experiments conducted in this thesis, the major focus of the theoretical description is on compressional waves in solid anisotropic materials.

Ultrasonic Wave Propagation in Infinite Anisotropic Elastic Solids

The wave propagation velocity of a monochromatic wave is defined as

$$c = \lambda f \tag{2.14}$$

with c being the propagation velocity (speed of sound) and f the frequency of the wave. The speed of sound is a material characteristic and is defined by the mass density and the linear elastic properties.
The linear elastic properties describe the stiffness of a material, the capability to deform proportionally and reversibly to an external load. In solids, the linear elastic properties can be defined by the generalized Hooke's law, which describes how much a material deforms under a specific stress. Hooke's law linearly relates stress, strain, and stiffness in an ideal, perfectly elastic solid

$$\sigma = C\,\varepsilon \tag{2.15}$$

with σ representing the stress tensor, ε the strain tensor and C the stiffness tensor. In index notation, the relation is:

$$\sigma_{ij} = c_{ijkl}\,\varepsilon_{kl} \qquad (i,j,k,l = 1,2,3) \tag{2.16}$$

where ε_{kl} is related to the particle displacement u

$$\varepsilon_{kl} = \frac{1}{2}\left(\frac{\partial u_k}{\partial x_l} + \frac{\partial u_l}{\partial x_k}\right). \tag{2.17}$$

The stiffness tensor C represents the intrinsic mechanical properties of the elastic continuum. It is a fourth order tensor with a maximum of 21 independent coefficients depending on the material symmetry. In matrix form (using Voigt's notation[1]), Eq. (2.16) can be expressed as

$$\begin{bmatrix}\sigma_{11}\\ \sigma_{22}\\ \sigma_{33}\\ \sigma_{23}\\ \sigma_{13}\\ \sigma_{12}\end{bmatrix} = \begin{bmatrix} c_{11} & c_{12} & c_{13} & c_{14} & c_{15} & c_{16}\\ & c_{22} & c_{23} & c_{24} & c_{25} & c_{26}\\ & & c_{33} & c_{34} & c_{35} & c_{36}\\ & & & c_{44} & c_{45} & c_{46}\\ & sym. & & & c_{55} & c_{56}\\ & & & & & c_{66}\end{bmatrix} \cdot \begin{bmatrix}\varepsilon_{11}\\ \varepsilon_{22}\\ \varepsilon_{33}\\ 2\varepsilon_{23}\\ 2\varepsilon_{13}\\ 2\varepsilon_{12}\end{bmatrix}. \tag{2.18}$$

In orthotropic materials with three orthogonal planes of symmetry (in the material coordinate system (x_1-x_2-x_3)), the number of independent coefficients of the stiffness tensor is reduced to 9

$$C = \begin{bmatrix} c_{11} & c_{12} & c_{13} & 0 & 0 & 0\\ c_{12} & c_{22} & c_{23} & 0 & 0 & 0\\ c_{13} & c_{23} & c_{33} & 0 & 0 & 0\\ 0 & 0 & 0 & c_{44} & 0 & 0\\ 0 & 0 & 0 & 0 & c_{55} & 0\\ 0 & 0 & 0 & 0 & 0 & c_{66}\end{bmatrix}. \tag{2.19}$$

In the case of a transverse isotropic symmetry in an axial-symmetric system, the stiffness tensor is comprised of five independent coefficients

$$C = \begin{bmatrix} c_{11} & c_{12} & c_{13} & 0 & 0 & 0\\ c_{12} & c_{22} & c_{13} & 0 & 0 & 0\\ c_{13} & c_{13} & c_{33} & 0 & 0 & 0\\ 0 & 0 & 0 & c_{44} & 0 & 0\\ 0 & 0 & 0 & 0 & c_{44} & 0\\ 0 & 0 & 0 & 0 & 0 & (c_{11}-c_{12})/2\end{bmatrix}. \tag{2.20}$$

[1] Voigt notation: each pair of subscripts in the tensor equations is condensed to a single: 1↔11; 2↔22; 3↔33; 4↔23; 5↔13; 6↔12

A transverse isotropic symmetry can be assumed, for example, for the mineralized collagen fibril investigated in this thesis. Accordingly, the corresponding stiffness tensor is used in the theoretical simulations of the fibrils in bone. It is worth noting that the inverse stiffness tensor C^{-1}, i.e. the compliance tensor, of an orthotropic material can be expressed as a function of the engineering parameters Young's moduli E_i, Poisson ratios ν_{ij} , and shear moduli G_{ij}

$$\begin{bmatrix} \varepsilon_{11} \\ \varepsilon_{22} \\ \varepsilon_{33} \\ 2\varepsilon_{23} \\ 2\varepsilon_{13} \\ 2\varepsilon_{12} \end{bmatrix} = \begin{bmatrix} \frac{1}{E_1} & -\frac{\nu_{12}}{E_2} & -\frac{\nu_{13}}{E_3} & 0 & 0 & 0 \\ -\frac{\nu_{21}}{E_1} & \frac{1}{E_2} & -\frac{\nu_{23}}{E_3} & 0 & 0 & 0 \\ -\frac{\nu_{31}}{E_1} & -\frac{\nu_{32}}{E_2} & \frac{1}{E_3} & 0 & 0 & 0 \\ 0 & 0 & 0 & \frac{1}{G_{23}} & 0 & 0 \\ 0 & 0 & 0 & 0 & \frac{1}{G_{13}} & 0 \\ 0 & 0 & 0 & 0 & 0 & \frac{1}{G_{12}} \end{bmatrix} \cdot \begin{bmatrix} \sigma_{11} \\ \sigma_{22} \\ \sigma_{33} \\ \sigma_{23} \\ \sigma_{13} \\ \sigma_{12} \end{bmatrix}. \tag{2.21}$$

Plane Wave Propagation in Elastic Media

The full derivation of the wave propagation equation is beyond the scope of this summary. The detailed mathematical description can be found in standard text books [134–137]. A brief overview of the principle mathematical derivation is provided below.

In an ideal solid (neglecting body forces) the equation of motion of the elastic continuum is

$$\rho \frac{\partial^2 u_i}{\partial t^2} = \frac{\partial \sigma_{ij}}{\partial x_j} \tag{2.22}$$

where ρ denotes the mass density of the solid and u the particle displacement. For plane wave propagation, the displacement u in the direction of the unit vector n (normal to the wavefront) is

$$u_i = U\, p_i\, e^{-i(k_j x_j - \omega t)} \tag{2.23}$$

with U being the amplitude of the harmonic wave, p_i the displacement (or unit polarization) vector, k the wave vector, and ω the angular frequency. The wave vector is defined as

$$k_j = \frac{2\pi}{\lambda}\, n_j = \frac{\omega}{v_{phase}}\, n_j. \tag{2.24}$$

By combining the stress-strain relationship (Eqs. 2.16), the relationship between strain and displacement (Eq. 2.17), plus the equation describing the motion of the elastic continuum (Eq. 2.22) and considering the direction of particle displacement (i.e. compressional or shear wave), it can be demonstrated that the phase velocity v_{ij} of the acoustic wave is directly determined

by the material stiffness and the mass density

$$\begin{aligned} c_{ii} &= \rho v_{ii}^2 \qquad (i = 1, 2, 3) \\ c_{44} &= \rho v_{23}^2 = \rho v_{32}^2 \\ c_{55} &= \rho v_{13}^2 = \rho v_{31}^2 \\ c_{66} &= \rho v_{12}^2 = \rho v_{21}^2 . \end{aligned} \tag{2.25}$$

Acoustic Impedance and Elasticity

The characteristic acoustic impedance in anisotropic materials is represented by the tensor Z_n and relates tensile stresses σ_i to particle displacement velocities v_j [136]:

$$-\sigma_i^n = (Z^n)_{ij} \frac{\partial u_j}{\partial t} = (Z^n)_{ij} v_j \qquad (i = 1, 2, 3) \tag{2.26}$$

where n is the direction in which the impedance is measured. The normal stress σ_i^n is defined as

$$\begin{bmatrix} \sigma_1^n \\ \sigma_2^n \\ \sigma_3^n \end{bmatrix} = \begin{bmatrix} n_1 & 0 & 0 & 0 & n_3 & n_2 \\ 0 & n_2 & 0 & n_3 & 0 & n_1 \\ 0 & 0 & n_3 & n_2 & n_1 & 0 \end{bmatrix} \cdot \begin{bmatrix} \sigma_{11} \\ \sigma_{22} \\ \sigma_{33} \\ \sigma_{23} \\ \sigma_{13} \\ \sigma_{12} \end{bmatrix} . \tag{2.27}$$

Combination of the elasticity equations (Eqs. 2.16, 2.17) leads to

$$\frac{\partial \sigma_{ij}}{\partial t} = c_{ijkl} \frac{\partial \varepsilon}{\partial t} = \frac{1}{2} c_{ijkl} \left(\frac{\partial v_k}{\partial x_l} + \frac{\partial v_l}{\partial x_k} \right). \tag{2.28}$$

For plane waves (Eq. 2.23) $\partial/\partial x$ and $\partial/\partial t$ can be replaced by (ik_j) and $(i\omega)$, respectively. This leads to the following relation

$$\begin{bmatrix} \sigma_{11} \\ \sigma_{22} \\ \sigma_{33} \\ \sigma_{23} \\ \sigma_{13} \\ \sigma_{12} \end{bmatrix} = \begin{bmatrix} c_{11} & c_{12} & c_{13} & c_{14} & c_{15} & c_{16} \\ & c_{22} & c_{23} & c_{24} & c_{25} & c_{26} \\ & & c_{33} & c_{34} & c_{35} & c_{36} \\ & & & c_{44} & c_{45} & c_{46} \\ & sym. & & & c_{55} & c_{56} \\ & & & & & c_{66} \end{bmatrix} \cdot i \begin{bmatrix} k_0 & 0 & 0 \\ 0 & k_2 & 0 \\ 0 & 0 & k_1 \\ 0 & k_3 & k_2 \\ k_3 & 0 & k_1 \\ k_2 & k_1 & 0 \end{bmatrix} \begin{bmatrix} v_1 \\ v_2 \\ v_3 \end{bmatrix} . \tag{2.29}$$

Considering Eq. 2.26 and substitution of Eq. 2.29 for Eq. 2.27 leads to

$$\omega Z^n = \begin{bmatrix} n_1 & 0 & 0 & 0 & n_3 & n_2 \\ 0 & n_2 & 0 & n_3 & 0 & n_1 \\ 0 & 0 & n_3 & n_2 & n_1 & 0 \end{bmatrix} \cdot \begin{bmatrix} c_{11} & c_{12} & c_{13} & c_{14} & c_{15} & c_{16} \\ & c_{22} & c_{23} & c_{24} & c_{25} & c_{26} \\ & & c_{33} & c_{34} & c_{35} & c_{36} \\ & & & c_{44} & c_{45} & c_{46} \\ & sym. & & & c_{55} & c_{56} \\ & & & & & c_{66} \end{bmatrix} \cdot \begin{bmatrix} k_0 & 0 & 0 \\ 0 & k_2 & 0 \\ 0 & 0 & k_1 \\ 0 & k_3 & k_2 \\ k_3 & 0 & k_1 \\ k_2 & k_1 & 0 \end{bmatrix}. \tag{2.30}$$

For a compressional wave propagating in x_3 direction is $(n_1, n_2, n_3) = (0, 0, 1)$ and $(k_1, k_2, k_3) = (0, 0, \omega(v_{33}^{phase}))$ with v_{33}^{phase} being the phase velocity of the longitudinal wave. In that case, Eq. 2.31 becomes

$$\omega(Z^{n_3})_{33} = c_{33}\, k_3. \tag{2.31}$$

Furthermore, based on Eq. 2.25, for an orthotropic material this can be developed into

$$(Z^{n_3})_{33} = \sqrt{c_{33}\,\rho}. \tag{2.32}$$

In general, if wave propagation direction and particle displacement are in the same direction x_i, the acoustic impedance Z_{ii} is directly proportional to the elastic coefficient c_{ii} and the mass density ρ:

$$Z_{ii} = \sqrt{c_{ii}\,\rho} \tag{2.33}$$

Acoustic Microscopy Impedance Mapping

Acoustic impedance mapping is the most straightforward approach to assess microelastic properties of bone by means of acoustic microscopy [138]. It is based on the detection of confocal acoustic waves reflected from the probed sample surface in amplitude or time-resolved mode. In the experiments presented in this thesis, high-frequency ultrasound based impedance mapping was conducted at the following frequencies: 200 MHz, 900 MHz and 1.3 GHz.

Acoustic Microscopy in Reflection Mode

SAM is based on directing focused acoustic waves at a target specimen (Fig. 2.8a). The ultrasound waves are generated by a piezoelectric transducer, converting radiofrequency signals into acoustic waves. A sapphire lens is employed to focus the acoustic waves. The acoustic waves are carried by a coupling fluid (e.g. water or ethanol) to the sample. As a result of the interaction between ultrasound and sample, components of the incident wave are scat-

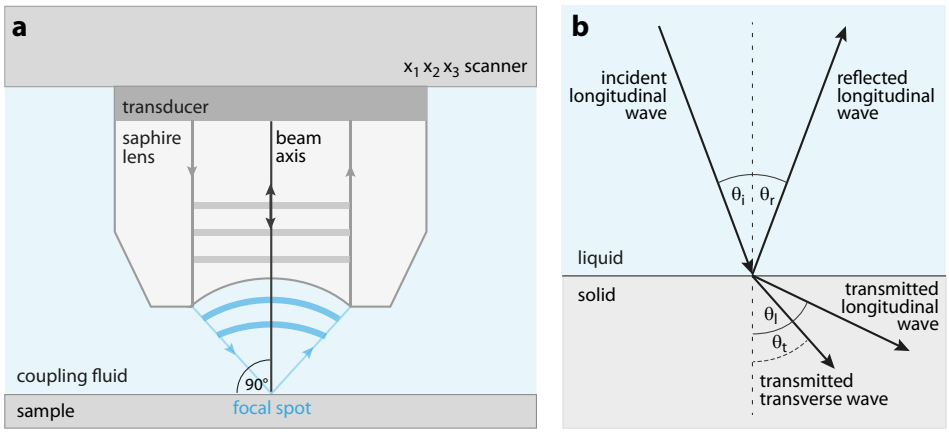

Figure 2.8: Schematic of acoustic wave transmission and reflection. a) Schematic sketch of a scanning acoustic microscope in confocal mode (normal incidence). (b) Oblique incidence of ultrasound waves.

tered, reflected, transmitted, or absorbed depending on the elastic properties and the angle of incidence between the acoustic beam and the interface of coupling fluid and sample surface. In confocal configuration, the reflected wave can be detected using the same lens. The specimen is scanned by translation of the transducer in a plane parallel to the sample surface. At each scan position, the signal of the reflected acoustic wave is recorded.

Reflection and Transmission

To understand the material characteristic signal conveyed in the reflected wave, acoustic wave reflection at the interface between liquid and solid is briefly summarized below.

Impingement of a plane wave on a smooth plane interface between two media with different acoustic impedance generates a reflected and a transmitted wave. The angles of reflected and transmitted wave with respect to the incident acoustic beam are defined by Snell's law. In confocal acoustic microscopy, the axis of the incident beam is perpendicular (normal incidence, $\theta_i = 0°$) to the interface between coupling medium (fluid) and bone sample (solid), and the focal spot is located on the sample surface (Fig. 2.8). Accordingly, both reflected and transmitted waves are normal to the interface. Under these conditions, the incoming waves are in phase and shear wave generation is diminished [139, 140]. Therefore, the reflected waves correspond to compressional waves only. The measured amplitude V of the reflected wave is proportional to the reflection coefficient R [98]

$$R = \frac{Z_S - Z_{CM}}{Z_S + Z_{CM}} \tag{2.34}$$

with Z_S and Z_{CM} representing the acoustic impedance values of the specimen under investigation and the coupling medium, respectively. Correspondingly, the transmission coefficient T describing the transmitted wave at normal incidence is defined by

$$T = \frac{2Z_S}{Z_S + Z_{CM}}. \tag{2.35}$$

Reflection and transmission coefficients are related by

$$1 + R = T. \tag{2.36}$$

In case of oblique incidence (Fig. 2.8b), both compressional and shear waves are generated in the sample.

The measured amplitude V of the reflected wave is related to the reflection coefficient R by a linear relationship determined by the experimental setup. This linear correlation can be defined by calibrating the system with homogenous, isotropic, and non-dispersive reference materials with known characteristic acoustic impedance values [67, 98].

Attenuation

Ultrasound attenuation is mainly determined by absorption and scattering processes. In general, absorption is the result of different processes, including thermal conductance, chemical and viscous effects. However, acoustic absorption in biological tissues is not yet fully understood [141]. Scattering phenomena depend on the interaction between ultrasonic waves and material inhomogeneities (particles) with different density or elasticity than their surrounding media. As a result of such interaction, the propagation direction, the frequency, the phase velocity, and the amplitude of the scattered acoustic wave may be changed in comparison with the incident one. The characteristic of single-particle scattering depends crucially on the wavelength of the incident acoustic wave λ and the dimension of the scatterer d [142]:

- **Specular reflection**, as described by the law of reflection (Eq. 2.36) is observed for $\lambda << d$.
- Small scatterers with $\lambda >> d$ lead to **Rayleigh scattering**. The intensity I of the scattered acoustic is: $\propto d^6/\lambda^4$.
- **Mie scattering** describes interaction with larger scatterers ($\lambda \sim d$), but

involves complicated mathematical description beyond the scope of this thesis.

In general, acoustic attenuation is defined by an exponential decrease of the acoustic pressure amplitude p and the acoustic intensity I with increasing distance x:

$$p = p_0\, e^{-\alpha x} I = I_0\, e^{-2\alpha x} \tag{2.37}$$

with $p_{z=0} = p_0$, $I_{z=0} = I_0$ and α being the frequency-dependent attenuation coefficient. In high-frequency acoustic measurements of bone, important attenuation mechanisms that significantly contribute to signal attenuation are: (i) scattering effects due to material inhomogeneities (e.g. porosity, elastic inhomogeneities) and (ii) compressional to shear mode conversion. It is worth noting that attenuation particularly affects measurements on trabecular bone, most likely due to increased scattering as a result of large surface-to-volume ratios [141].

As a result of reinforced attenuation at high frequencies, the tissue penetration depth of high-resolution acoustic microscopy is limited to analyses of the sample surface. In experiments with lateral resolutions in the micrometer range, as conducted in this thesis, axial penetration depths on the micron scale are achieved.

2.2.3 Synchrotron Phase Contrast Nano Tomography

X-rays are electromagnetic waves with a wavelength in the range of 10 pm - 10 nm. The interaction between X-rays and matter takes place through either attenuation or retardation processes, affecting the amplitude and phase of the X-ray beam, respectively. These interaction events can be described by the complex refractive index n [143]:

$$n = 1 - \delta_n + i\beta \tag{2.38}$$

with δ_n being the refractive index decrement (real part), related to the phase shift and β the absorption index (imaginary part), related to the attenuation of the incident X-ray beam after propagation through the sample.

X-ray imaging techniques exploit both attenuation and phase retardation events. In bone studies, X-ray imaging based on attenuation is a widely applied standard method to analyze the micro-structure of bone. Due to higher resolutions in comparison with attenuation based imaging, X-ray phase contrast methods have become more and more popular in bone research within the last years. A brief outline of the theoretical background of X-ray imaging and 3D image reconstruction is presented in the following subsection with particular focus on X-ray phase retardation-based 3D imaging as carried out in the experimental part of this thesis.

X-ray Attenuation

Three processes contribute to X-ray attenuation: Rayleigh scattering, Compton scattering and photoelectric absorption.

As mentioned in section 3.1, Rayleigh scattering is an elastic scattering event and describes the deviation of the X-ray photons from their incident trajectory after collision with an electron. The contribution of Rayleigh scattering to X-ray beam attenuation is minor and the elastic scattering intensity or the elastic cross-section $\sigma_{Rayleigh}$, estimating the likelihood of the event, is:

$$\sigma_{Rayleigh} \propto (\frac{Z}{E_i})^2 \tag{2.39}$$

where Z represents the atomic number and E_i the energy of the incident X-ray radiation.

Compton scattering is an inelastic interaction process that involves the transfer of energy from the incident photon to an electron and the scattering of a photon with decreased energy in relation to the incident one. The corresponding cross-section of inelastic scattering in the X-ray regime can be

approximated as

$$\sigma_{Compton} \propto (\frac{Z}{E_i}). \tag{2.40}$$

Photoelectric absorption is the most dominant X-ray attenuation process in the regime of hard X-rays (8 keV – 100 keV) and is highly important for synchrotron X-ray imaging. The cross-section due to photoelectric absorption corresponds with Z and E as follows

$$\sigma_{PA} \propto (\frac{Z^5}{E_i^{4.5}}). \tag{2.41}$$

The linear attenuation coefficient μ corresponds to the total contribution of all three processes

$$\mu = \frac{N_A \, \rho \, \sigma_{tot}}{A} \tag{2.42}$$

with N_A, ρ, A and σ_{tot} being the Avogadro number, the mass density, the atomic mass number, and the sum of the individual cross-sections, respectively. The attenuation coefficient μ is related to the absorption index β as follows:

$$\beta = \frac{\lambda}{4\pi} \mu \tag{2.43}$$

where λ is the wavelength. Consequently, substitution of μ by the sum of cross-section results in

$$\beta \propto (\frac{Z}{E_i})^2 + (\frac{Z}{E_i}) + (\frac{Z^5}{E_i^{4.5}}). \tag{2.44}$$

The quantifiable attenuation-determined loss in the intensity of a monochromatic incident X-ray beam traversing through a homogenous sample is described by the Lambert-Beer law, which states that the number of photons decreases exponentially as a function of the attenuation coefficient and the thickness of the sample z:

$$I = I_0 \, e^{-\mu z} \tag{2.45}$$

where I and I_0 denote the intensity of the X-ray beam before and after propagation through the sample.

X-ray Phase Shift

The propagation of X-rays through matter is accompanied not only by attenuation effects, but furthermore by a modification in the phase of the wavefront in comparison to the incident one traversing though a vacuum [144].

The phase shift is related to forward scattering events by the electrons in the sample and is predominantly determined by the electron density and the energy of the incident X-ray beam. The electron density can be approximated by the mass density of the sample. As a result, the refractive index decrement δ_n is proportional to the square of the wavelength of the incident X-ray beam and the mass density ρ of the sample [145]:

$$\delta_n \propto 1.35 * 10^{-6} \rho \lambda^2 \propto \frac{\rho}{E_i^2} \tag{2.46}$$

with ρ in g/cm^3 and λ in Å. At this point, it is important to understand that the mass density can be directly derived from the refractive index decrement δ_n related to the X-ray phase shift, but not from the attenuation-associated absorption index μ.

Comparison of Attenuation and Phase-Shift-Based Image Contrast

Comparison of the energy dependencies of the attenuation coefficient β (Eq. 2.44) and the refractive index δ_n (Eq. 2.46) illustrates that the X-ray beam is much more sensitive to phase shifts than to attenuation processes. To emphasize this fact, the ratio between β and δ_n is shown for cortical bone and X-ray energies in the range of 10 - 20 keV (as applied in the measurements presented in this thesis) in Fig. 2.9. It can be observed that the difference grows with increasing X-ray energies. Consequently, phase-sensitive imaging methods provide much higher contrasts regarding density variations than conventional absorption imaging. Moreover, because phase contrast imaging is not intrinsically coupled to the absorption of X-rays in the material, the radiation dose can potentially be reduced by using higher X-ray energies [146].

X-ray Phase Contrast Retrieval

Several methods have been applied to measure the phase shift of hard X-rays, including grating interferometry [146, 148], analyzer methods [149, 150], and propagation-based approaches [151–153]. Within the frame of this thesis, propagation-based phase retrieval was applied, which is briefly introduced in this subsection.

Propagation-based phase imaging techniques exploit interference patterns created as a result of Fresnel diffraction. The experimental setup consists of a coherent X-ray beam in line with sample and detector (Fig. 2.10). In contrast to absorption-based tomographic setups, the detector is placed some distance from to the sample, thus allowing for free space propagation and therefore for interference between refracted and non-refracted parts of the wavefront. The

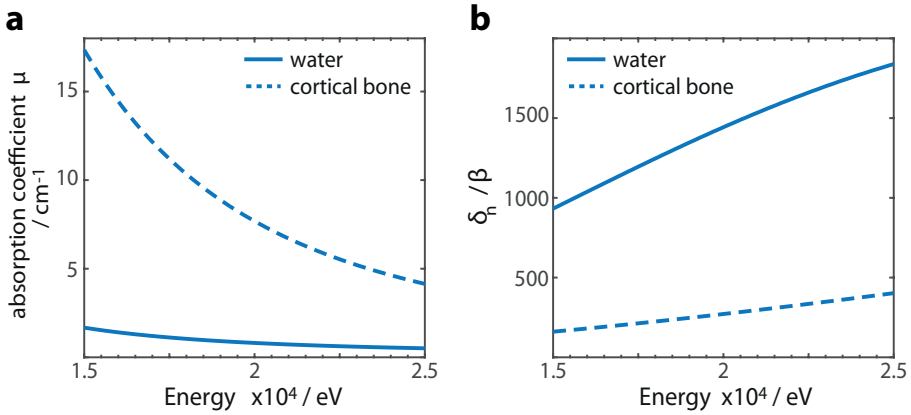

Figure 2.9: Comparison of the energy sensitivity of attenuation and phase retardation processes. (a) Attenuation coefficient for water and cortical bone as a function of X-ray energies between 15 and 25 keV (b) Corresponding ratio of the refractive index δ_n and the attenuation coefficient β in the same energy regime. Image adapted from [147].

created interference pattern contains Fresnel 'fringes' and schemes, which are proportional to the second derivative of the wavefront phase [152]. Extraction of the phase information is done using phase retrieval algorithms. However, Fresnel imaging at a specific distance d_2 between sample and detector is blind to some characteristic frequencies in the phase distribution (as explained by the Talbot effect [154, 155]). To account for this effect, several images are recorded at different distances between sample and detector, and at various angles. From each set of images, corresponding to the same rotation angle, 2D phase maps are calculated. Using a tomographic algorithm (next subsection), 3D images are reconstructed from phase maps. The reconstructed image represents the 3D distribution of the refractive index.

Another fast and straightforward method for phase retrieval is the Paganin algorithm [156] which can be applied to a propagation-induced phase contrast image recorded at a single sample-detector distance. The algorithm is based on the assumption of a linear relationship between refractive index decrement δ_n and the absorption index β. However, the method has some major drawbacks: (i) to extract quantitative information, the ratio δ_n/β needs to be estimated as input parameter. Moreover, (ii) the method can only be applied on homogenous samples.

Principles of Tomographic Reconstruction

In tomographic measurements, 3D images of an object are obtained by recording 2D object projections at multiple angles. Each object projection represents a set of line integrals and a complete set of projections corresponds to the Radon transform of the object. Hence, the inverse of the Radon trans-

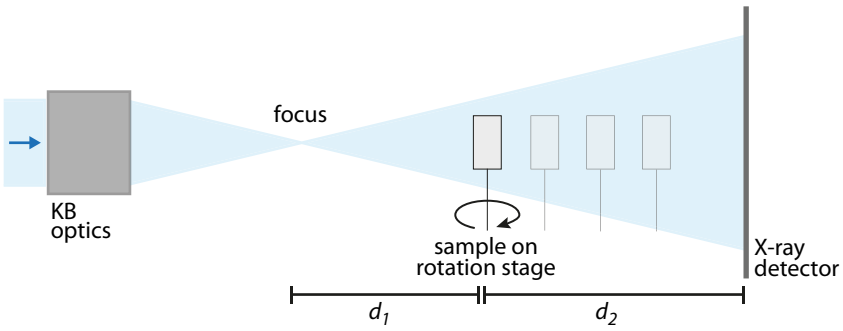

Figure 2.10: Schematic sketch of the experimental SR-nanoCT setup. d_1 and d_2 depict the distance between focus-sample and sample-detector, respectively. The image magnification is defined by d_2/d_1. Phase contrast imaging makes use of 1-4 distances according to the phase retrieval algorithm. KB is Kirkpatrick-Baez.

form can be used to reconstruct the original object from the projection data. Standard object reconstruction is done by derivation of the inverse of the Radon transform via backprojection algorithms. As a result of the image reconstruction process, 3D stacks of cross-sectional object images are generated.

In X-ray computed tomography, the recorded projections are the attenuation and phase shift of the X-ray beam induced along straight lines parallel to the X-ray propagation direction z. They are defined as:

$$B(\vec{x}, z) = \frac{2\pi}{\lambda} \int \beta(\vec{x}) dz \tag{2.47}$$

$$D(\vec{x}, z) = -\frac{2\pi}{\lambda} \int \delta_n(\vec{x}) dz \tag{2.48}$$

with $\vec{x}$ indicating a vector in a spatial coordinate system (x,y,z). Both attenuation and phase retrieved from recorded projections can be used as input to reconstruct the 3D object structure using backprojection algorithms.

The standard backprojection of the Radon transform is based on the Fourier slice theorem. The Fourier slice theorem says that the Fourier transform of a parallel projection through a 2D object for a given angle corresponds to a slice (line along θ) of the 2D Fourier transform of the object function. In other words, the 1D Fourier transform of the Radon transform corresponds to the 2D Fourier transform of the object function. However, backprojection of all object projections provides a blurred image of the original object. Therefore, a filter is applied on the projection. This efficient reconstruction algorithm is called Filtered backprojection (FBP) and is widely used in X-ray tomography and other imaging domains. In case of parallel beam geometry,

the transition from 2D to 3D object reconstruction is direct, due to straight paths of X-rays through the sample, perpendicular to the detector. Each row of the detector yields an individual 2D reconstruction which can be used to create a 3D stack. For the standard case of cone beam geometry, the extension of the FBP is known as the Feldkamp algorithm.

Synchrotron Radiation Based X-ray Computed Tomography

Phase contrast retrieval requires a coherent X-ray beam of high flux that cannot be provided by standard desktop CT devices, but can be generated in synchrotrons. Synchrotron radiation is electromagnetic radiation emitted by charged particles accelerated by magnetic fields. In synchrotron sources, high energy electrons circulate in a storage ring at constant speed, close to the speed of light. Radiation is produced when these charged particles traverse through the fields of bending magnets, employed to keep the particles in a closed orbit and in wigglers and undulators on straight insertion sections. In comparison to standard desktop CT devices, synchrotron X-ray sources provide much higher beam brilliance. The brilliance accounts for various beam characteristics including the number of emitted photons per second, the collimation of the beam and the spectral bandwidth. As a result of the increased flux, higher beam intensities are achieved. Furthermore, artefacts due to beam hardening can be avoided using monochromatic synchrotron X-ray beams.

Synchrotron X-ray Phase Contrast CT Investigations of Bone Structure

Due to its high resolution in the nanometer range and its ability to image 3D structures non-destructively in close to native state, synchrotron phase contrast nano computed tomography (SR-nanoCT) has become an attractive tool for characterization of bone ultra-structure. To date, several applications addressing structural and functional features of both the lacuno-canalicular network (LCN) and the bone matrix have been presented: imaging of the 3D LCN provided manifold insights into the geometry and distribution of osteocyte lacunae and in particular into the microarchitecture of the interconnecting canaliculi [91, 157, 158]. Due to high sensitivity and resolution of the technique, mass density gradients at the LCN were detected that support the hypothesis of functional matrix mineralization through calcium diffusion from the extracellular fluid in the LCN to the bone matrix [158]. Furthermore, based on the detailed 3D input on the LCN architecture, the magnitude and distribution of in vivo microstrains on mechanosensing osteocytes and their dendrites was estimated in an FE modeling approach [157]. Bone matrix appeared highly textured in SR-nanoCT imaging [13, 91] and characteristic arching structures were observed in measurements of lamellar bone.

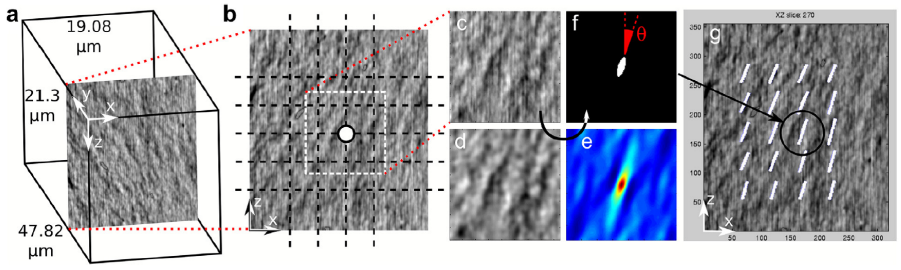

Figure 2.11: Slicewise derivation of the predominant fibril orientation of single sublamellae based on 2D ACF analysis. (a) Exemplary VOI with dimensions showing an indivual slice selected for ACF analysis. (b) Grayscale image of the selected slice. Black dashed lines indicate the analysis grid on which the ACF was applied. The white dashed box depicts one analysis section with the center marked as a white circle. (c) The unfiltered grayscale image of this section. (d) The filtered image of the section. (e) Normalized ACF outcome signal. (f) Segmented ACF signal providing the orientation in-plane fibril angle, indicated in red. (It is worth noting that the in-plane angle is marked with θ in this image, in the following the in-plane orientation of fibrils will be indicated with φ) (g) Main orientations of all grid sections of this slice, represented by white lines. Image reprinted from [13] with permission from Elsevier.

Comparison with similar arching structures provided by means of TEM [16] and qBEI [159] suggested that the matrix texture was determined by the orientation of mineralized collagen fibrils. Based on these observations, a texture analysis enabling direct derivation of quantitative 3D collagen fibril orientation from tomographic phase contrast slices was developed by Varga et al. [13]. This analysis represents one of the reference tools applied in this thesis. Therefore, a brief summary of the methodology is presented in the next subsection.

Investigation of the Collagen Orientation

The major advantage of SR-nanoCT based analysis of the collagen orientation in lamellar bone proposed by Varga et al. [13] is the ability of the technique to visualize internal structures in 3D, enabling an analysis of the fibril orientation from any angle by virtually slicing the 3D data in arbitrary directions. In sharp contrast, the majority of techniques applied in investigations of the collagen microarchitecture so far, either probed the tissue surface of bulk samples in reflection mode or thin sample sections in transmission. In any case, disassembly of the specimen is obligatory and orientation information is deduced from 2D sections.

In their approach, Varga et al. [13] intended to align volumes of interest (VOI) with the lamellar plane (xz slices of VOI) and the long axis of osteons (z-axis of VOI). Lamellae were virtually divided in sublamellae, each imaged on an individual slice (Fig. 2.11a). The fibril orientation of every slice was

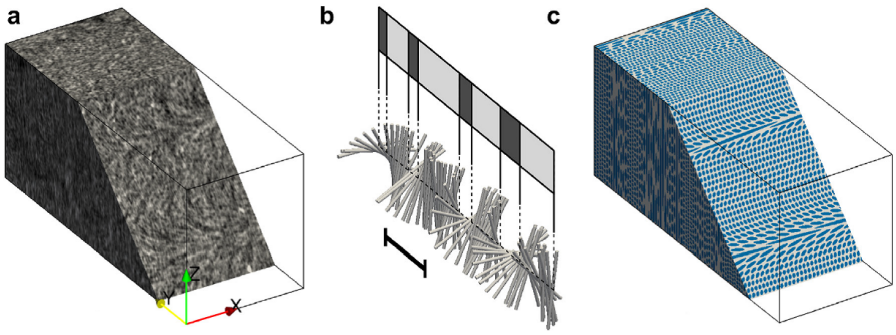

Figure 2.12: 3D fibril orientation derived by means of the SR-nanoCT ACF based analysis. (a) Raw data of an exemplary VOI, virtually cropped obliquely to the lamellar plane. The characteristic arching structures of the lamellar plywood patterns are clearly visible. (b) Corresponding fibril orientations illustrated as cylinders. Scale bar 10 µm. (c) 3D virtual model indicating the fibrils of the VOI and their orientation as blue cylinders embedded in extrafibrillar white matrix. Image reprinted from [13] with permission from Elsevier.

independently quantified using an autocorrelation function (ACF), defined in the Fourier domain as:

$$ACF = \left| F_d^{-1} \left(F_d(I)\, conj\left(F_d(I)\right)\right)\right| \tag{2.49}$$

with F_d and F_d^{-1} representing the discrete Fourier and discrete inverse Fourier transforms of the image intensity I, respectively. The FWHM of the normalized ACF was fitted with an ellipse (Fig 2.11 e,f). The major axis of this ACF ellipse was considered to represent the direction with least periodicity in the slice. This direction was defined as dominant fibril orientation angle φ in the lamellar plane (Fig 2.11g). The ratio of minor and major axis lengths was considered to represent the degree of anisotropy in the sublamellar slice.

Using this approach, Varga et al.[13] demonstrated that mineralized collagen fibrils of sublamellar slices were uniaxially aligned (Fig. 2.12). Furthermore, they provided evidence of two dominant plywood structures in human lamellar bone, namely twisted and oscillating plywood pattern (Sec. 2.1.2). Interestingly, these patterns were found to coexist within the same osteon. Infrequently, disorganized sublamellar regions were observed, corroborating recent findings from Reznikov et al. [21, 63].

3

Experimental studies

3.1 3D Raman mapping of the collagen fibril orientation in lamellar bone

This chapter is based on a study published by S. Schrof et al. [160]. The study was also presented as a talk [1] and a poster [2] [3] at national and international conferences. Several figures, selected paragraphs, and considerations presented in this section were part of the publication.

3.1.1 Introduction

A multitude of analytical techniques have been applied so far to investigate the structural organization of collagen fibrils in lamellar bone, including polarized light microscopy [14, 15], confocal laser scanning microscopy (CLSM) [76, 77], transmission electron microscopy (TEM) and scanning electron microscopy (SEM) [16–19], Fourier transformed infrared spectroscopy (FTIR) [80], small angle X-ray scattering (SAXS) and wide angle X-ray diffraction (WAXD) [22, 161], dual beam electron microscopy (FIB-SEM) [20, 21] and synchrotron X-ray phase nano-tomography (SR-nanoCT) [13]. Major drawbacks of these methodologies were the requirement of complex sample preparation, the inability to investigate bone samples in native hydrated state, and the limited field of view. Moreover, the majority of these approaches were limited to structural imaging only and failed to provide a more comprehensive picture of interplaying compositional aspects. In contrast, PRS is a non-destructive imaging tool qualified for effective and concurrent assessment of chemical and structural information of bone tissue. The aim of this study was demonstrate that PRS is capable of elucidating the intricate 3D arrangements of collagen fibrils in human lamellar bone.

[1] S.Schrof et al.: *Assessment of collagen fibril orientation in human lamellar bone with scanning acoustic microscopy and polarized Raman microscopy*; 5th European Symposium on Ultrasonic Characterization of Bone (ESUCB), 05/2013 Granada, Spain; oral presentation

[2] Schrof et al.: *3D Raman Mapping of Collagen Molecule Orientation in Human Lamellar Bone*; The World Molecular Imaging Congress (WMIC), 09/2014, Seoul, Korea; poster presentation

[3] Schrof et al.: *3D Raman Mapping of Collagen Molecule Orientation in Human Lamellar Bone*. Euro Bio-inspired Materials, 03/2014, Potsdam, Germany; poster presentation

3.1.2 Materials and Methods

Sample Preparation

Four human femoral bone samples (samples A-D) were obtained from four body donors. None of the body donors had a reported bone pathology. Ethical approval was granted by the Ethics Commission of the Martin Luther University Halle. The donors or their legal guardians provided informed written consent to donate their tissue for investigation. One cross-sectional sample was prepared from the femoral mid-diaphysis of each body donor using a diamond-coated band saw (Fig. 3.1). The samples were dehydrated in series of ethanol (70%, 80%, 96% and 100%, immersion for 24 h in each solution). After dehydration, samples were embedded in polymethylmethacrylate (PMMA). In order to prepare plane, smooth sample surfaces, specimens were ground using silicon carbide abrasive papers (grit size 4000; Phoenix 4000, Buehler, Düsseldorf, Germany). Subsequently, the surface was polished with a hard synthetic cloth, ethylene glycol suspension, and diamond particles with a diameter of 1 µm as an abrasive.

The sample surface was scanned by means of 50 MHz and 0.9 GHz SAM as explained elsewhere [8], to provide an overview image of the bone matrix and select single osteons for PRS analysis based on their size, shape, and lamellar structure.

Confocal Raman Setup

A schematic sketch of the standard confocal microscope setup (CRM200, WITec, Ulm, Germany) used for Raman spectroscopic measurements is depicted in Fig. 3.2. The confocal microscope included a laser source, an optical system, and a spectrograph. For excitation, a diode pumped linearly polarized continuous 785 nm near infrared laser (Toptica Photonics AG, Graefelfing, Germany) was chosen to minimize sample fluorescence. The laser power was set to 30 mW and the exciting beam was focused onto a spot approximately 10 µm underneath the sample surface by means of a water immersed objective (60x, NA = 1.0, Nikon, Tokyo, Japan). The back-scattered Raman photons were collected with the same objective and focused through a pinhole in front of the detection module to limit out-of-focus light and optimize the spatial resolution of the instrument. To reject the elastically scattered Rayleigh photons, a notch filter was introduced into the optical pathway.

The detection module included an air cooled CCD (PI-MAX, Princeton, Instruments Inc., Trenton, NJ, USA) behind a grating (300 g mm^{-1}) spectrograph (Acton, Princeton Instruments Inc., Trenton, NJ, USA) with a spectral resolution of 6 cm^{-1}, allowing for intensity registry with respect to the wave-

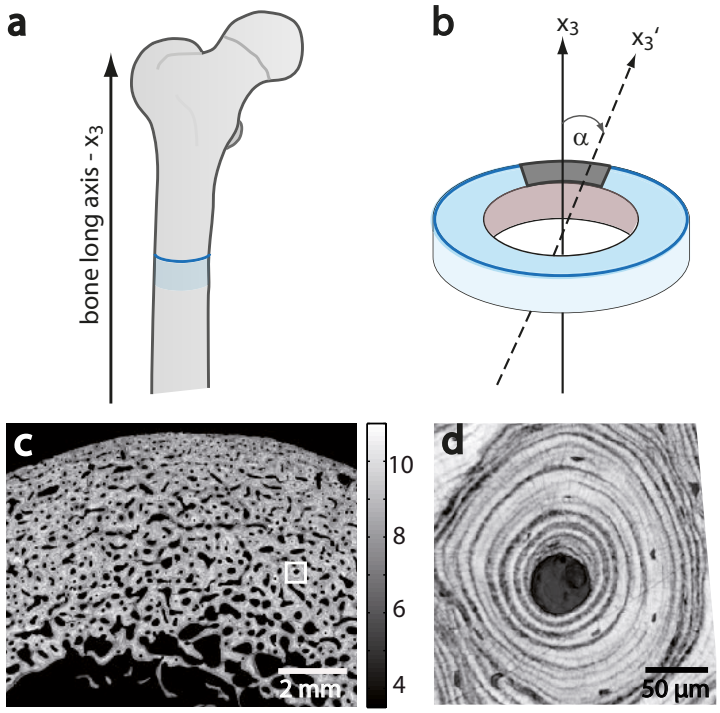

Figure 3.1: Schematic drawing illustrating the sample preparation. (a) Proximal femur, the location of the sample section in the diaphyseal region is marked. (b) Schematic of the cortical bone cross-sectional sample. The investigated sample surface plane (x_1x_2 plane) is depicted in blue. The gray area indicates the location of the 50 MHz acoustic microscopy image in panel (c). The 50 MHz acoustic impedance map was used for selection of single osteons for PRS analysis (marked with white rectangle). (d) Marked osteon from (c) imaged using 0.9 GHz SAM. The characteristic lamellar structure is clearly visible.

length. To enable polarized measurements, the polarization angle β of the incident laser was rotated by means of a half-wave plate. For mapping, a piezoelectric table moving the sample in x_1 and x_2 directions was employed. The sample surface was scanned in mapping mode in steps of 1 µm. Spectra acquisition speed was balanced with the laser excitation power and the spatial resolution. Acquisition times of 0.3 - 0.5 s per scan point were found to be well suited for collagen orientation mapping of bone tissue.

Theoretically, according to the diffraction limit, a lateral resolution of $\Delta x = 0.61\,\lambda/NA$ is expected in Raman microspectroscopy. However, in bone analysis, the resolution is strongly influenced by scattering processes and the focal volume is significantly increased due to diffuse light of single and multiple scattering events. In this thesis, a spatial resolution of approximately 1 µm in lateral and 4 µm in axial directions was achieved in Raman experiments on the bone matrix.

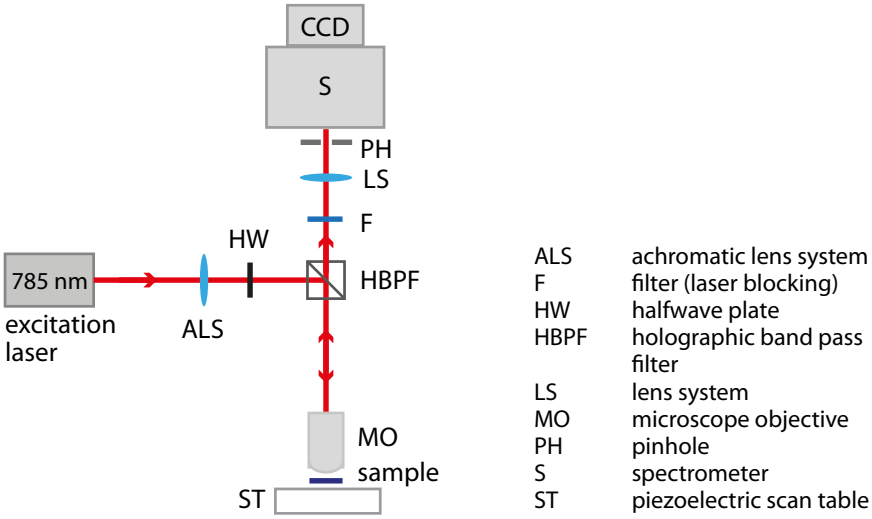

Figure 3.2: Schematic sketch of the confocal Raman setup illustrating the optical pathway. The laser is coupled into an optical fiber and focused onto the sample by means of the objective lens. Reflected Raman photons are collected with the same objective lens and focused through the pinhole into a multimode fiber. This fiber delivers the Raman scattered laser light to the detection system consisting of spectrometer and CCD. A halfwave plate is introduced into the optical pathway to change the angle of polarization β of the incident laser beam.

Derivation of Collagen Orientation Maps

The amide I intensity variation, measured at every scan point as a function of the polarization angle β of the incident laser, was fitted using the following equation:

$$I = a\left(1 + b\left(\cos\left(2\left(\beta - c\right)\right)\right)\right) \tag{3.1}$$

with I representing the amide I intensity, a the average amide I intensity of all polarization angles at every scan position, and c the phase shift. Based on this, collagen orientation maps displaying the three fit parameters at every pixel were calculated. In these maps, parameters a, b, and c are represented by the color code of the pixel, length, and orientation of the black arrows, respectively [35]. An illustration of this fitting method and the corresponding derivation of the collagen orientation map is depicted in Fig. 3.3.

Theoretical Modeling

To estimate the effect of the limited resolution and the misalignment between the incident laser beam and the lamellar plane of the osteon on the amide I intensity due to oblique sample cutting, experimental data were compared to theoretical models of ideal lamellar fibril arrangements. In these theoretical models, single lamellae were assumed to consist of 25 sublayers, each consist-

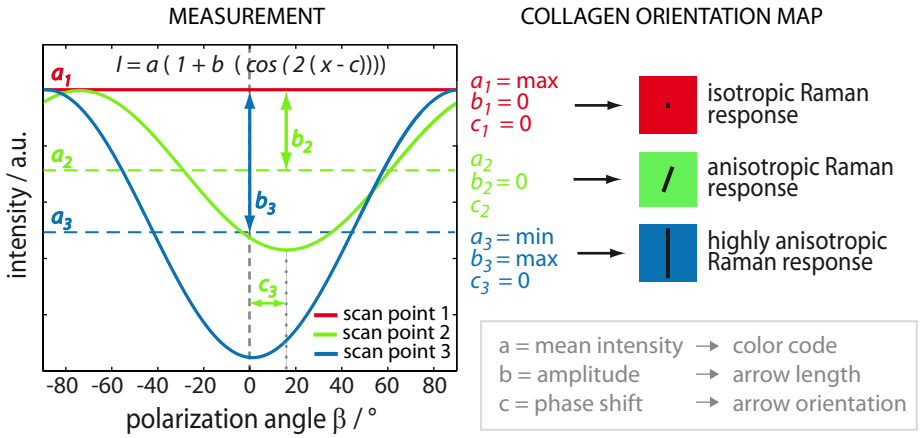

Figure 3.3: Illustration of the amide I intensity fitting procedure and the corresponding visualization of the fit parameters in collagen orientation maps of three hypothetical scan points. The theoretical graph shows the intensity of the amide I Raman band of three hypothetical scan points measured at increasing angles of polarization β of the incident laser. Parameter a (dashed lines), is the average amide I intensity at each scan location. In collagen orientation maps, a is represented by the color code. Parameter b, the amplitude of the fit, is determined by the degree of anisotropy of the Raman response. Parameter b is depicted by the length of the black arrows in collagen orientation maps. Finally, fit parameter c, the phase shift, is represented by the orientation of the black arrows. Image adapted from [160] with permission from Elsevier.

ing of unidirectional aligned fibrils with a distinct angle of twist φ. Furthermore, based on the results of earlier studies [13], a lamellar thickness of 7 µm was defined. According to the findings of previous studies, the lamellar sublayer arrangement was simulated as (i) twisted plywood pattern [16] and (ii) oscillating plywood structure [13]. A continuous fibril rotation was assumed for the idealized twisted plywood model with a twist rate of 25° per µm and an angle of twist $\Delta\varphi$=7.5° between fibrils of adjacent sublayers. The twisted plywood model was characterized by a full rotation from φ=0° to φ=180°. In contrast, lamellae with an oscillating plywood arrangement were defined by fibrils following a sinusoidal oscillation between φ=0° and φ=30°. Schematics of both patterns are depicted in Fig. 3.9.

Moreover, due to the limited spatial resolution of the confocal setup, averaging of the Raman signal of several sublayers with different fibril orientations was expected. To estimate this effect, the volume of the focus of the setup was simulated as a three-dimensional Gaussian function with a full-width-at-half-maximum (FWHM) in lateral direction (x_1 and x_2) of 1 µm and a FWHM in axial direction (x_3) of 4 µm. Weighted mean signals of the sublayers within this volume were calculated.

3.1.3 Results and Discussion

Chemical Mapping

Several osteons with characteristic lamellar structure were selected for PRS analysis on each sample. A subsection of these osteons was scanned in Raman mapping mode. As indicated in chapter 2.2.1, it is crucial in Raman spectroscopy to distinguish between structural- and chemical-associated peak modulations. To separate compositional and organizational effects on the amide I peak modulation, amide III, phosphate ν_1 PO_4^{-3}, and phosphate ν_2 PO_4^{-3} Raman bands were analyzed as well. Fig. 3.4 displays chemical maps of all four bands recorded at fixed laser polarization. Confirming the findings of Kazanci et al. [24], amide I and phosphate ν_1 PO_4^{-3} were found to reflect the lamellar character of cortical bone, whereas amide III and phosphate ν_2 PO_4^{-3} did not exhibit lamellar modulations. Consequently, it was concluded that amide I intensity variations in lamellae with homogeneous amide III intensity distribution were determined by structural effects only, the composition of these lamellae was considered uniform. Therefore, further analysis of collagen orientation information was done solely on osteonal lamellae with homogenous amide III value distribution.

3D Orientation of the Collagen Fibrils in Osteonal Bone Lamellae

Following the protocol presented in literature [35, 36], the amide I peak was analyzed as a function of the laser polarization to calculate collagen orientation maps of the scanned osteonal subsections. An example of such a measurement is illustrated in Fig. 3.5. A schematic illustration of the investigated osteon is provided in Fig. 3.5a, indicating the location of the scanned tissue region with respect to the central Haversian canal. The collagen orientation map (Fig. 3.5b) depicts several osteonal lamellae and one osteocyte lacuna. A comprehensive signal analysis revealed that the amide I signal at every scan position in the osteonal lamellae exhibited a sinusoidal intensity modulation with respect to the angle of polarization β of the laser. The amplitude of this sinusoidal signal function (parameter b) reflected the local degree of anisotropy of the amide I scattering. A variation of the degree of anisotropy as a function of the location within the lamellae was observed. Comparison of the average degree of anisotropy of single scan lines, parallel to the lamellar plane (Fig. 3.5c), demonstrated that the degree of anisotropy was highest in regions of minimal mean amide I intensities (ROI 1a). In contrast, the degree of anisotropy was found to be minimal and the amide I intensity variation close to isotropic, in regions of maximal mean amide I intensity (ROI 1b). Pixelwise analysis of the amide I response in osteonal lamellae in the direction perpendicular to the lamellar plane (Fig. 3.5d) provided evidence

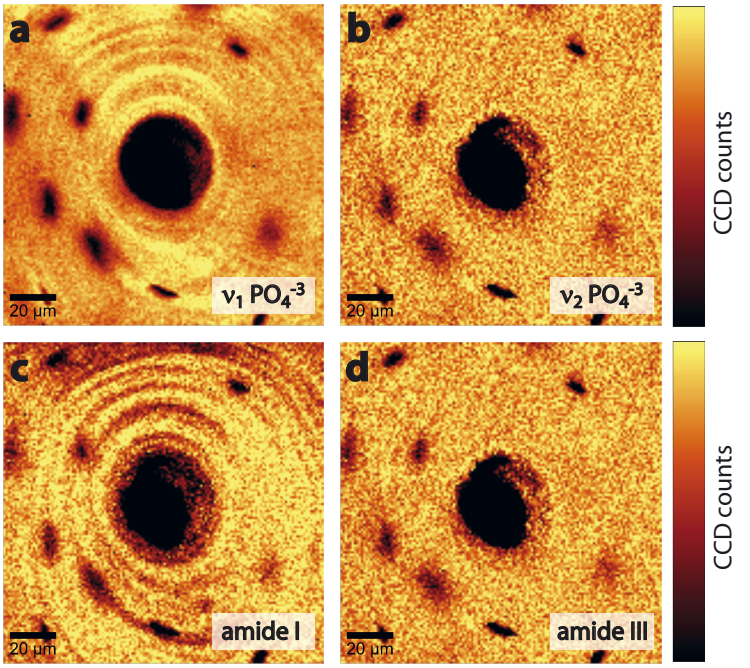

Figure 3.4: PRS chemical mapping of a single osteon. Contrast images of (a) phosphate ν_1 PO_4^{-3} (CCD counts: 220–420), (b) phosphate ν_2 PO_4^{-3} (CCD counts: 50–160), (c) amide I (CCD counts: 40–155), and (d) amide III (CCD counts: 25–80) Raman bands are displayed. The angle polarization of the incident laser light is β=90° in all images. Phosphate ν_1 PO_4^{-3} and amide I Raman band mirror the characteristic lamellar structure of the tissue, whereas phosphate ν_2 PO_4^{-3} and amide III exhibit relatively homogeneous intensity distributions across the osteon. Scalebar is 20 µm.

of a periodic and gradual transition of the degree of anisotropy from close to isotropic to highly anisotropic as a function of the distance.

Recently, Galvis et al. [36] presented a theoretical approach, simulating the amide I scattering of small collagen-like molecules as a function of the molecular orientation with regard to the orientation and polarization of the incoming laser beam (summarized in Sec. 3.1). The authors of the study demonstrated that the degree of anisotropy of the amide I response at varying laser polarization angles was determined by the molecular orientation. For molecule rotations in the plane perpendicular to the incident laser (in-plane rotations) a sinusoidal anisotropic response was observed. The sinusoidal response was maximal if the molecular orientation was perpendicular to the laser polarization. Minimal scattering intensity was observed when both the laser polarization and the molecule were parallel. It is worth noting that the degree did not vary for in-plane rotations of the molecules.
In sharp contrast, for rotations in the plane parallel to the incidence direction of the laser (out-of-plane rotations), a varying degree of anisotropy was ob-

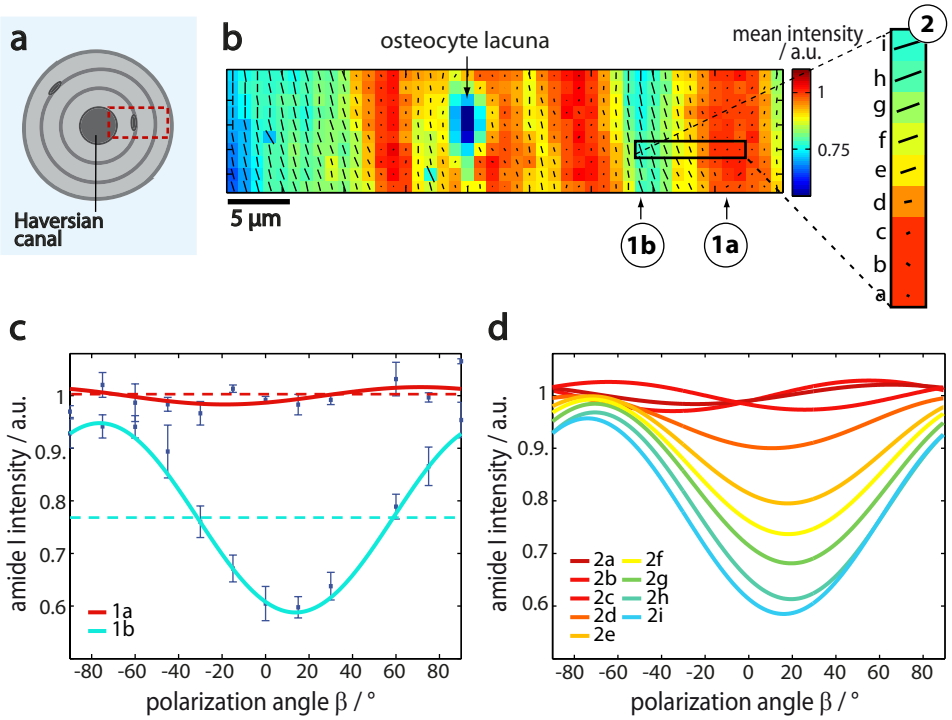

Figure 3.5: Amide I Raman response in osteonal lamellae. (a) Schematic of the investigated osteon, the location of the osteonal subsection scanned with PRS is marked in dashed lines. (b) Collagen orientation map derived from fitting the amide I signal recorded at 12 angles of polarization of the incident laser light. The collagen orientation map shows several osteonal lamellae and an osteocyte lacuna. Three representative ROIs (1a, vertical scan line; 1b, vertical scan line; 2, horizontal scan line) that were analyzed in close detail are marked. (c) Mean amide I intensity of ROI 1a and b as a function of the angle of laser polarization β. Dashed lines indicate the mean amide I intensity of these scan lines. In regions with maximal amide I intensities such as ROI 1a, an isotropic amide I signal (parameter b close to zero) can be observed. In contrast, in regions with minimal mean amide I intensities (parameter b maximal), the amide I signal is highly anisotropic. (d) Comparison of the amide I intensities of adjacent scan points in the direction perpendicular to the lamellar plane (ROI 2). A gradual change of the amide I response from close to isotropic to highly anisotropic can be observed.

served. The amide I scattering was fully isotropic if the molecules were parallel to the incidence direction of the laser beam (Fig. 2.6). However, the degree of anisotropy increased with augmenting out-of-plane angles. (The global coordinate system, in-plane, and out-of-plane moleculce rotations with respect to incident laser are defined in Fig. 3.6.)

Galvis et al. [36] verified their theoretical findings with experimental data measured on rat tail tendon (RTT), consisting of highly oriented, parallel aligned collagen molecules. These experiments provided evidence that the measured degree of anisotropy is determined by the projection of the fibril orientation to the x_1x_3 plane.

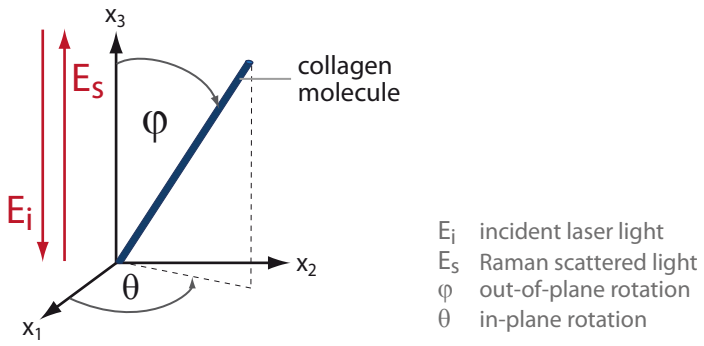

Figure 3.6: Definition of the global coordinate system. The angles describing the orientation of the collagen molecules with respect to the incidence direction of the laser are defined. The direction of incident laser and Raman scattered light are represented by the red arrows. The lamellar plane of the investigated osteonal lamellae is displayed.

Based on the findings of Galvis et al. [36], it can be inferred that the gradual transition of the degree of anisotropy and the simultaneous variation of the mean amide I intensity in osteonal lamellae is a consequence of collagen molecules incrementally changing their orientation in the lamellar plane. However, it is worth noting that even though this change in orientation can be recognized, it is not possible to assign specific angles of twist φ to concrete values of the mean amide I intensity or the degree of anisotropy based on these data sets only.

To gain specific information on the 3D orientation of the collagen fibrils from the amide I signal, the fit parameters *a* (mean amide I intensity) and *b* (amplitude of the fit function) were examined in closer detail. A second collagen orientation map derived from measurements of another osteon on a different sample is presented in Fig. 3.7. Several representative ROIs with sufficient distance to the osteocyte lacunae and the Haversian canal were selected for correlative analysis of the fit parameters. A sinusoidal modulation of both, parameter *a* and parameter *b*, was found in all investigated lamellae (Fig. 3.7b). A strong negative correlation between the parameters was observed and quantified in linear regression analysis (R^2=0.89). Moreover, using fast Fourier transformation (FFT) analysis (Fig. 3.7c), a mean phase shift of 178.3 ± 6.4 ° was determined between maximum points of the two sinusoidal parameters in nine investigated lamellae. Thus, it can be concluded that parameters *a* and *b* were in antiphase. These experimental findings were well in line with the theoretical simulations provided by Galvis et al. [36]. The experimental results demonstrated that the correlation between the mean amide I intensity and the degree of anisotropy theoretically predicated and verified in systems of low complexity such as RTT were also applicable to

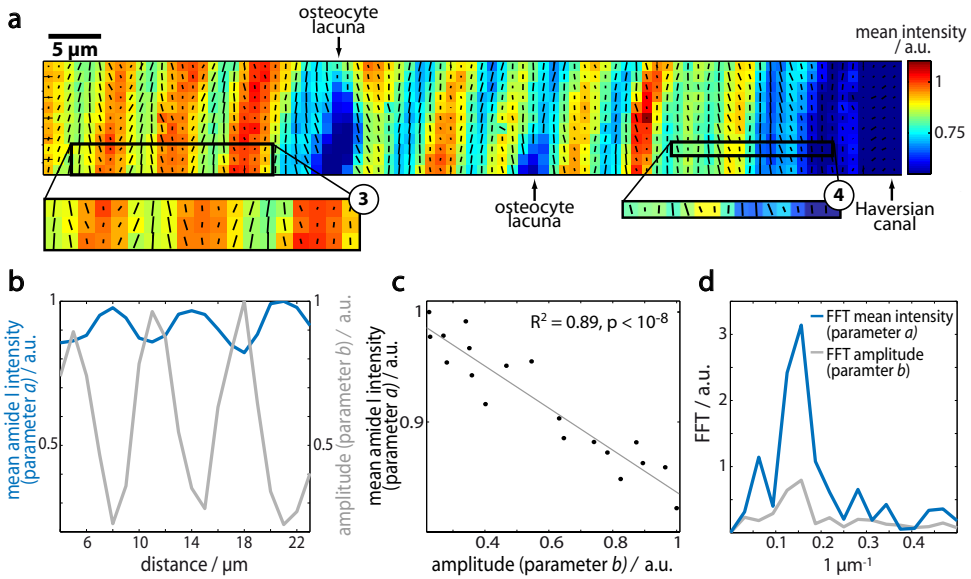

Figure 3.7: Correlative analysis of parameters a and b in the lamellar structure. (a) The collagen orientation map shows several osteonal lamellae, part of the central Haversian canal and two osteocyte lacunae. Two representative ROIs (3 and 4) are marked. (b) Mean values of the amide I intensity (parameter *a*) and amplitude of the fit (parameter *b*) of ROI 1 in panel a are shown as a function of the distance in the direction perpendicular to the lamellar plane. The graph visualizes the sinusoidal regression and negative correlation of the two parameters. (c) Linear regression analysis between the amide I intensity (blue) and the amplitude of the fitting curve (gray) of ROI 1 revealed a strong negative correlation (R^2=0.89). (d) Fast Fourier transformation of the amide I intensity (blue) and the amplitude of the fit (gray) of ROI 1 shows that the main components of the Fourier transforms of the two parameters are in good agreement. The oscillation period of both parameters in ROI 1 is 6.5 µm. The phase shift between the local maxima of the two sinusoidal signals in ROI 1 is 178.3±6.4 °.

complex structures with changing orientation like osteonal lamellae.

There are several conclusions that may be drawn regarding these findings:

- Firstly and most relevantly is that parameter *b*, the degree of anisotropy, is a stable indicator of the collagen inclination in the plane parallel to the incoming laser beam in highly organized biological tissues of both low and high complexity. In the case of lamellar bone as investigated in the presented experiments, parameter *b* reflects on the modulation of the angle of twist of collagen fibrils in the lamellar plane. Furthermore, as the degree of anisotropy is highly correlated with the mean amide I intensity (parameter *a*), the latter may be analyzed as a marker of the orientation of collagen fibrils in cortical bone lamellae with unvarying amide III intensities as well.

- Previous studies [35] have provided proof that the phase shift, parameter *c*, quantifies the collagen orientation in the plane perpendicular to the incidence direction of the laser, which corresponds to the sample surface plane in the presented experiments. Hence these findings clarify that PRS-based analysis of the amide I intensity modulation is capable of providing 3D orientation information in a complex structured and mineralized biological tissue such as cortical bone.
- As pointed out in chapter 3.1, PRS-based analysis of the amide I intensity may also be applied to native, fully hydrated samples, thus qualifing the approach for concurrent examination of several parameters related to the composition and structure of samples in a close to physiological condition.

Identification of Specific Plywood Patterns

Interestingly, several osteons were observed that exhibited lamellae characterized by fibrils rotated out of the lamellar plane (e.g. marked in ROI 2 in Fig. 3.5 b, ROI 3 and 4 in Fig. 3.7 a). So far, none of the idealized fibril organization models reported in literature (Sec. 2.1.2) has described a rotation of collagen fibrils out of the lamellar sublayers. However, similar patterns have been observed in bone lamellae by Giraud-Guille [15, 16] using SEM and TEM (Fig. 3.8 a), by Kingsmill and Boyde [159] using qBEI (Fig. 3.8 b), and by Langer et al. [91] by means of SR-nanoCT (Fig. 3.8 c). Giraud-Guille described these patterns as arching structures and referred to them as obliquely sectioned twisted plywood arrangements. These arching structure sresemble the periodic out-of-lamellar-plane tilts found in PRS-based collagen orientation maps.

To better clarify this phenomenon, experimental PRS results of the fibrillar orientation in bone lamellae were compared to theoretical 3D models of prominent, idealized fibril arrangements, namely twisted and oscillating plywood patterns. In these simulations, twisted and oscillating plywood patterns were characterized by a full continuous twist and an oscillating fibril orientation with a maximal angle of deflection φ=30°, respectively. Multiple views of these 3D models from different perspectives are depicted in Fig. 3.9. The illustrations visualize that even though the two models may be clearly distinguished between from the side view (Fig. 3.9a, d), their projections to the top view perspective appear very similar (Fig. 3.9 b, e). It is worth noting that the top view projections of both 3D models exhibit parallel-aligned fibrils only, no rotations of the fibrils out of the lamellar plane can be observed. However, this is just the case for the ideal situation where the lamellar plane and the osteon axis are perfectly parallel to the incidence direction of the laser beam. In reality, a tilt between the lamellar plane and the incidence direction

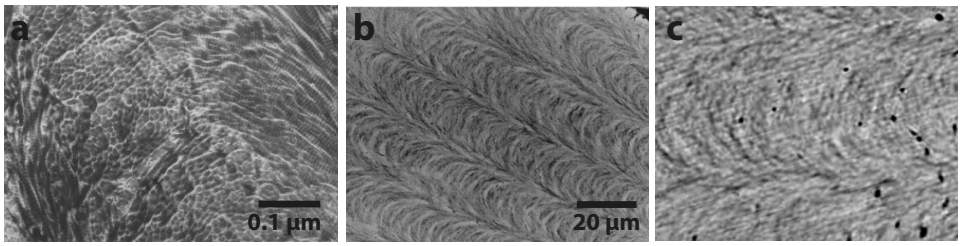

Figure 3.8: Observations of arched patterns in bone lamellae. (a) Collagen fibril orientation in osteon forming arching structures, imaged by means of TEM on ultra thin section from decalcified compact human bone. Image reprinted from [15] with permission from Elsevier. (b) Collagen fiber arrangement of human interstitial bone lamellae from the mental foramen region measured using qBEI. Image reproduced from [159] with permission from Wiley. (c) Human femoral lamellae imaged by means of SR-nanoCT. Image reproduced from [91].

of the laser is to be expected, as a perfect cutting of the bone specimen with respect to the osteonal axis is unlikely. Slightly oblique specimen cutting, defined by a small angle of tilt α between the osteonal axis (the bone long axis) and the sample surface normal can easily occur (Fig. 3.1b). Therefore, 3D models with a tilt in the x_1x_2 plane α=10° , corresponding to an obliquely cut sample, were simulated as well (Fig. 3.9 c, f). Interestingly, the projections of the fibrils models of obliquely cut lamellae appeared to be rotated out of the lamellar plane from a top view perspective. These theoretical simulations confirm the conclusions of Girauld-Guille [15, 16] that the arching structures imaged with different techniques are the result of oblique specimen sectioning. Furthermore, oblique twisted and oscillating plywood models featured varying directions of rotation out of the lamellar plane (indicated with gray and blue arrows in Fig. 3.9), thus allowing for differentiation from a top view perspective. Whereas the fibrils of the oblique twisted plywood lamellae were rotated in both directions with respect to the lamellar plane, the fibrils of the oblique oscillating plywood model were all inclined in the same direction.
Similar out-of-lamellar-plane rotation patterns were observed in the experimentally analyzed lamellae imaged in collagen orientation maps, suggesting a slightly oblique sectioning of the samples. Lamellae corresponding to both oblique 3D models were identified in the maps (Fig. 3.9 g, h). The majority of the investigated lamellae displayed a rotation pattern corresponding to the twisted plywood arrangement and a small number of lamellae in close proximity to the Haversian canal featured a fibril rotation pattern comparable to the oscillating plywood pattern.

Confirming earlier studies using different technical approaches on human femoral bone [13, 63], murine tibia [20], and equine metacarpal bone [162], single lamellae were observed with individual sublayers of significantly in-

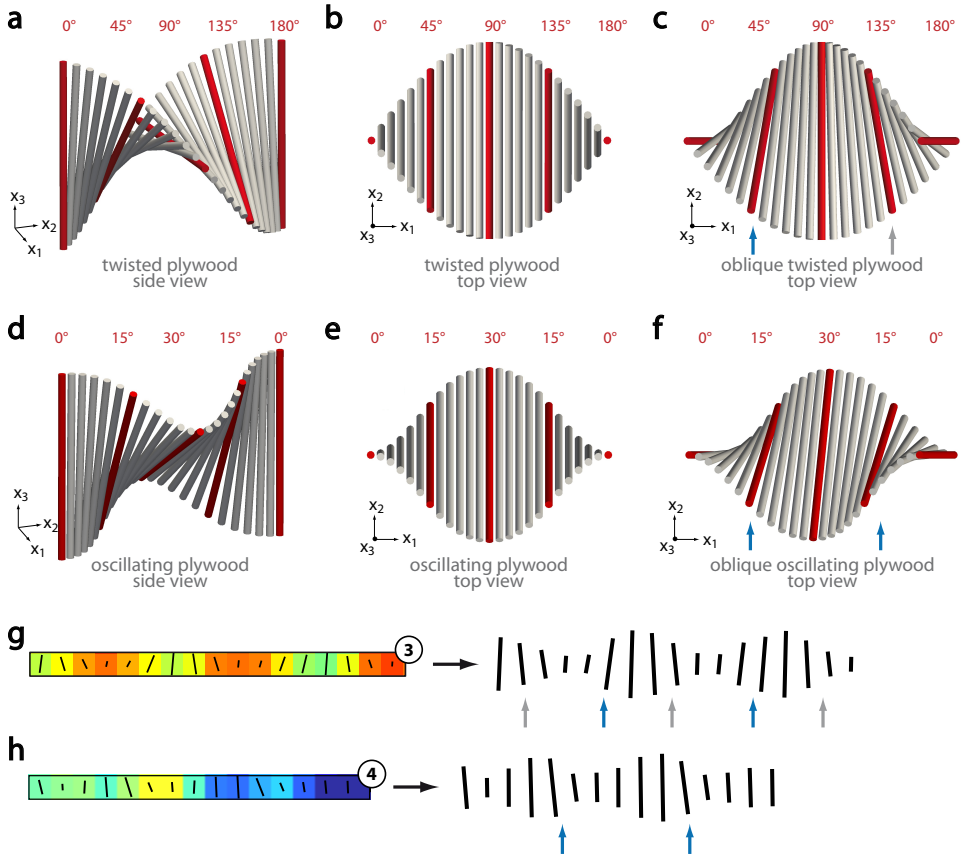

Figure 3.9: Comparison of theoretical simulations of idealized lamellar models to experimental data. 3D illustrations of the theoretical models represented from different perspectives are depicted in panels (a-f). Each cylinder represents a lamellar sublayer of unidirectional aligned collagen fibrils. (a) Twisted plywood pattern from side view perspective. (b) Corresponding top view of the twisted plywood pattern with an ideal cut perpendicular to the lamellar plane. The projections of the individual sublayers are parallel to the lamellar plane. (c) Simulation of a top view perspective on the twisted plywood pattern cut obliquely (α=10°) with respect to the lamellar plane. The projections of individual sublayers are rotated out of the lamellar plane (indicated by the blue and gray arrows). (d) Side view of the oscillating plywood model. (e) Side view of an oscillating plywood pattern with an ideal cut perpendicular to the lamellar plane. (f) Top view of an oscillating plywood pattern in an obliquely cut sample. The projections of the fibrils are rotated out of the lamellar plane (blue arrows). In contrast to the oblique twisted plywood pattern, the direction of the rotation out of the lamellar plane is the same for all sublayers. (g) Experimental PRS data (extracted from ROI 3, Fig. 3.7). The fibril orientations are periodically rotated out of the lamellar plane as a function of the location within the lamellae. The experimental data are well in line with the simulations of an oblique twisted plywood pattern (blue and gray arrows). (h) Experimental PRS data (extracted from ROI 4, Fig. 3.7). The out-of-lamellar-plane rotation is consistent with the oblique oscillating plywood pattern (blue arrows).

creased thickness (3-4 µm) of nearly unidirectional fibrils, aligned close to parallel with the osteonal axis (e.g. Fig 3.5 b).

PRS-based Indications of Disordered Collagen Fibrils in the Lamellar Structure

Ultimately, to explore the intrinsic heterogeneity of the osteonal tissue with respect to ordered and disordered fibril fractions in the lamellar structure, the degree of anisotropy of the amide I intensity was compared to the theoretical anisotropy predictions of single collagen molecules and experiments on RTT provided in earlier studies [35, 36] (Fig. 3.10). In contrast to lamellar bone tissue, these reference data sets result from unidirectional aligned collagen molecules only. To allow for such comparison, each data set was normalized to its maximum value.

Fig. 3.10a displays the amide I intensity of collagen-like peptide molecules oriented parallel (φ=0°) and perpendicular (φ=90°) to the incidence direction of the laser as a function of the laser polarization β [36]. Fig. 3.10b shows experimental data of wet non-stretched and dry pre-stretched RTT. Like the theoretical collagen molecules, RTT were parallel and perpendicular to the incidence direction of the laser positioned [35, 36]. The degree of anisotropy of the amide I Raman signal of theoretical collagen molecules and experimental pre-stretched RTT exhibited very similar values (Fig. 3.10c). Non-stretched wet RTT oriented perpendicular to the laser incidence direction featured a maximum degree of anisotropy that was slightly smaller. This difference may be explained by the bending of collagen molecules in the gap region of collagen fibrils, predicted by means of X-ray scattering and diffraction experiments, and molecular modeling [163, 164]. In sharp contrast, the maximum degree of anisotropy observed in osteonal lamellae was considerably lower (Fig. 3.10b, c) than the anisotropy of pre-stretched dry (~45% loss in anisotropy) and non-stretched wet RTT (~30% loss in anisotropy).

There are several possibilities that potentially provide an explanation for the loss of anisotropy observed in osteonal lamellae:

- As the fibril orientation information derived by means of PRS was not quantitative, the possibility cannot be excluded that there were no fibrils with a configuration perpendicular (φ=90°) to the incidence direction of the laser. However, this explanation could be excluded for the lamellae with identified twisted plywood arrangement (Sec. 3.1.3).

- The limited spatial resolution of the Raman microscope (~1 µm in lateral and ~4 µm in axial direction) represents a likely explanation for

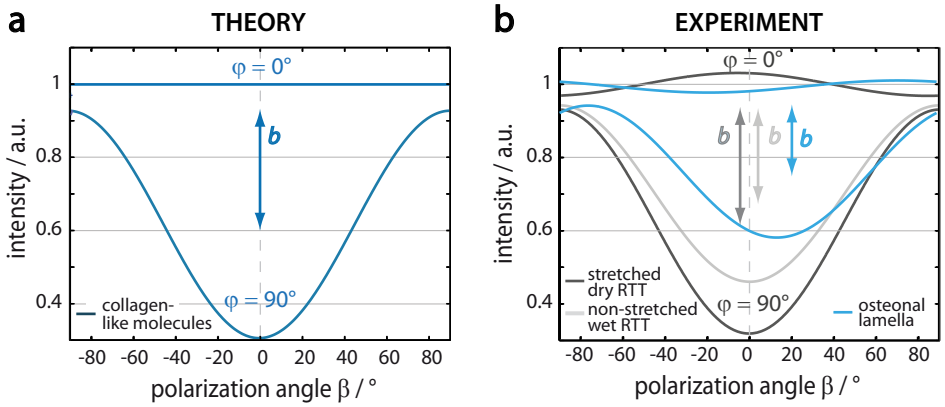

c

	collagen-like peptide molecules	stretched dry rat tail tendon	non-stretched wet rat tail tendon	osteonal tissue
parameter *b* / *a.u.*	0.31	0.31 ± 0.03	0.24 ± 0.03	0.17 ± 0.01

Figure 3.10: Comparative analysis of the degree of anisotropy of the amide I signal. (a) Theoretically estimated, average amide I intensity of four collagen-like peptide molecules with φ=0° (parallel configuration to the incoming laser beam) and φ=0° (perpendicular configuration to the incoming laser beam) as a function of the laser polarization β [36]. (b) Experimentally assessed data of wet pre-stretched and dry non-stretched rat tail tendon oriented parallel (φ=0°) and perpendicular (φ=90°) to the incoming laser beam [35, 36]. Furthermore, average and normalized experimental amide I response of the two regions in osteonal lamellae with the highest and lowest amide I intensity (Fig. 3.5, ROI 1a and 1b) are shown.

the loss of anisotropy in osteonal lamellae. In the case of a sublayer thickness ≤ 1 µm, the spectroscopic Raman measurements are the result of several lamellar sublayers interacting with the incident laser light within the focal volume. Hence the recorded Raman signal at every scan position comprises the signal of various fibrils with different orientations.

- Furthermore, an intrinsic disorder of the collagen fibrils within the lamellar structure is conceivable.

To estimate the impact of the limited spatial resolution on the loss of anisotropy, the interaction between laser light and osteonal lamellae in the confocal setup was theoretically simulated. For this simulation, an average lamellae arranged in an ideal twisted plywood pattern was assumed. Furthermore, based on the oscillation periods of parameter *a* and *b* presented in the previous subsection and the results reported by Varga et al. [13], a lamellar thickness of 7 µm was defined. As PRS estimates the projection of the fibril

orientation in the x_1x_2 plane, discrimination between different twist directions is not feasible. To account for this fact, the twisted plywood pattern was simulated as a continuous twist, characterized by fibrils rotating gradually from φ=0° to φ=90° and back to φ=0°. The focal volume of the experimental Raman setup was estimated by means of a 3D Gaussian distribution, characterized by a FWHM in lateral x_1 and x_2 directions of 1 µm and a FWHM in axial x_3 direction of 4 µm (Fig. 3.11a). To predict the effective twist angle φ^{eff} measured with the Raman setup, the focal volume was shifted step-by-step across the lamellae and weighted mean values of the sublayer-specific fibril orientations within the focal volume were calculated at each location (Fig. 3.11b). The simulation demonstrated that this averaging effect of the Raman setup affected particularly the measurements of maximal and minimal twist angles in the lamellar plywood structure. As a consequence, the effective measured twist angles of the sublayers with φ_1=0° and φ_2=90° predefined in the model were φ_1^{eff}=8° and φ_2^{eff}=82°, respectively.

Additionally, the impact of the limited resolution on an obliquely cut twisted plywood lamella was estimated (Fig. 3.11b). The simulation showed the same trend as for the case of straight cut lamellae: the maximal and minimal angles twist in the fibrillar arrangement were most affected. In comparison with the straight cut lamellae, the impact was even more pronounced.

Based on these calculations, the averaging effect of the limited resolution caused approximately two thirds of the loss in anisotropy of osteonal lamellae with respect to wet non-stretched RTT. Consequently, these estimations provide evidence that the limited spatial resolution is the major determinant of the loss in anisotropy of osteonal lamellae in comparison to measurements on RTT and theoretical predictions on collagen molecules. Note that these estimations hold true for an ideal twisted plywood arrangement only. The effect may be significantly stronger in thinner lamellae or generally different for lamellae with irregular sublayer thickness.

Nonetheless, the limited spatial resolution could not account for the observed total loss in anisotropy. Another reasonable explanation is the contribution of disordered collagen fibrils in the lamellar structure. Recently, Reznikov et al. [20, 63] reported the presence of thin lamellar sublayers exhibiting a increased level of fibrillar disorder in bone lamellae. Similarly, Varga et al. [13] reported regions consisting of less ordered fibrils within bone lamellae. On the other hand, both studies consistently also observed sublamellar regions of highly organized collagen fibrils. In such regions of high fibril order, a lower level of anisotropy loss would be expected in PRS analysis. However, in none of the examined osteonal lamellae did the degree in anisotropy feature values comparable to the ones of wet non-stretched RTT. This might potentially

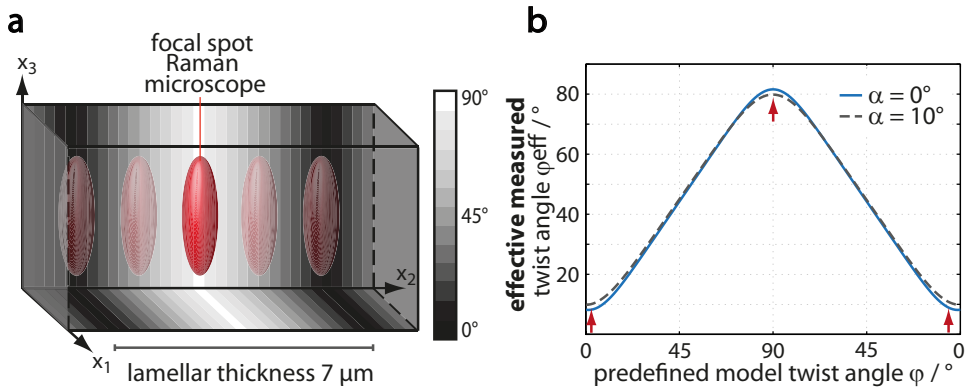

Figure 3.11: Theoretical estimation of the impact of the limited spatial resolution of the Raman microscope on the measurement of the fibril orientation. (a) Schematic sketch of the theoretical twisted plywood model. The lamella consists of 25 sublayers, each characterized by a distinct angle of twist φ of the collagen fibrils. The angles of twist of the lamellar sublayers are represented by the gray values. The focus volume of the Raman microscope is depicted in red. It is clearly visible that due to the limited spatial focal dimensions, each spectral measurement is the result of the focal interaction with several sublayers of the lamella. (b) Comparison of the predefined angles φ of the theoretical plywood model with the effectively assessed angles φ^{eff} of the setup. φ^{eff} was simulated as weighted average orientation of the fibrils within the focal volume. φ^{eff} was estimated for a perfectly perpendicular cut (α=0°) and an obliquely cut twisted plywood arrangement (α=10°). Due to the limited resolution, the effectively measured angles are larger and smaller at the minimum and maximum angles of twist of the model, respectively. The effect is further reinforced in the case of oblique cutting.

be explained by disordered collagen fibril evenly distributed over the entire lamellae, or by resolution determined averaging of ordered and disordered sublayers. Finally, the limited spatial resolution of the PRS approach makes the precise quantification of the contribution of disordered collagen fairly intricate and error-prone.

3.2 Multimodal correlative investigation of multiscalar bone matrix parameters

This chapter is based on a study published by Schrof et al. [165]. The study was also presented as a talk [4] and a poster [5] at national and international conferences. Several figures, selected paragraphs, and considerations presented in this section were part of the publication.

3.2.1 Motivation for a Multimodal Analysis

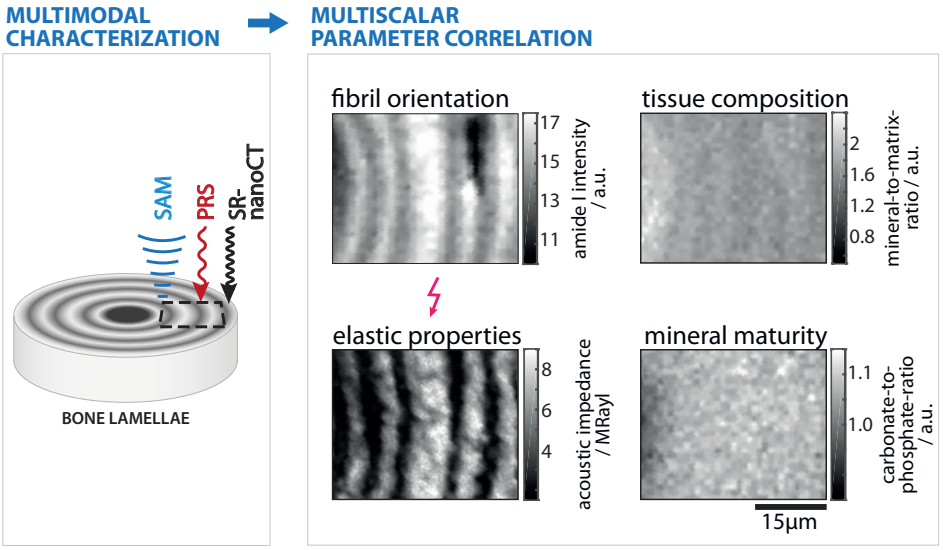

Figure 3.12: Schematic overview of the multimodal correlative investigation. Bone lamellae were imaged by means of SR-nanoCT, PRS, and SAM in a site-matched manner. Parameter maps were spatially correlated to analyze the interplay of lamellar structure, composition and elasticity. Image adapted from [165] with permission from Elsevier.

There are several key factors that determine the mechanical competence of lamellar bone on the micron scale: the complex 3D arrangement of its main components, namely collagen fibrils and mineral particles, the chemical composition, the tissue mineralization and mass density, and the the state of maturation of the hAP particles. To gain further insight into the complex interplay between material composition, structure, and resulting mechanical

[4] Schrof et al.: *Three-dimensional investigation of the relationship between orientation and microelastic properties of mineralized collagen fibrils in human osteonal bone.* 6th European Symposium on Ultrasonic Characterization of Bone (ESUCB), 06/2015 Corfu, Greece; oral presentation. ESRF users meeting 2015, 02/2015; oral presentation.

[5] Schrof et al.: *Multi-modal investigation of the interplay between three-dimensional fibrillar microarchitecture, tissue composition and microelastic properties of human cortical bone tissue.* Euro Bio-inspired Materials, 03/2016, Potsdam, Germany; poster presentation.

properties at the level of entire tissue domains and individual bone lamellae, SR-μCT, SR-nanoCT, PRS, and SAM were combined in this study to concurrently describe the diverse material characteristics and their correlations.

3.2.2 Materials and Methods

Sample Preparation

Four samples were prepared from four femoral bones of four human body donors (donor IDs A-D) that were obtained from the Center of Anatomy and Cell Biology, Medical University Vienna. Ethical approval for the sample collection was granted by the Human Ethics Committee of the Medical University of Vienna. The body donors or their legal guardians provided informed written consent to donate their tissue for research purposes. Bone sections were characterized in two preceding studies. First areal bone mineral density (aBMD) was determined using Dual-energy X-ray Absorptiometry (DXA) on the entire proximal femur [166] (Table 3.1). Second, in another study [157], SR-nanoCT measurements of the specimen were analyzed with regard to the morphology of the lacunar–canalicular network.

Cross-sections with a thickness of 10 mm were cut perpendicular to the bone long axis from the femoral shaft at a distance of approximately 1/3 of the total bone length from the proximal end using a diamond-coated band saw (Exakt 300, EXAKT Advanced Technologies GmbH, Norderstedt, Germany). A schematic sketch indicating the location of the sample dissection and illustrating the individual steps of the sample preparation and subsequent imaging procedure is displayed in Fig. 3.13. Immediately after dissection, the bone cross-sections were stored at -20°C until further preparation. Next, cubical sections of 5 mm thickness, aligned with the long bone axis, were sawn from the anterior–medial side of the cross-sections. Finally, using a high-precision lathe, cylindrical samples with a diameter of 500 μm and a length of approximately 5 mm (Fig. 3.13a-c) were prepared. The cylindrical samples were stored in 70 % ethanol until data acquisition.

Serial Multimodal Measurement Protocol

The bone specimens were characterized in serial measurements of SR-μCT, SR-nanoCT, PRS, and SAM. A schematic illustration of the serial measurement protocol and the imaged sample volumes and planes is displayed in Fig. 3.13c.

1. Low dose SR-μCT measurements were performed to provide 3D overviews of the entire sample volume. These overview scans were used to select

Table 3.1: Biometric information of human body-donors and summary of methodologies applied on the specimen. Areal bone mineral density (aBMD) was assessed by means of DXA in a previous study [166]. Two ROIs were imaged in a site-matched manner on sample A, one ROI was analyzed on samples B-D. Individual ROIs contained varying numbers of osteonal and interstitial tissue domains.

Donor ID	Donor age	Donor Sex	aBMD [g/cm^2]	applied methodologies
A	64	F	0.735	• ROI1: SR-µCT, SR-nanoCT, SAM, PRS • ROI2: SR-µCT, SAM, PRS
B	60	M	0.655	• SR-µCT, SR-nanoCT , SAM, PRS
C	68	F	0.822	• SR-µCT, SAM, PRS
D	71	M	1.18	• SR-µCT, SAM, PRS

volumes of interest (VOIs) suitable for further analysis, i.e. regions with sufficient distance to Haversian canals and minimal number of osteocyte lacunae.

2. These VOIs were scanned at nanometer resolution (~250 nm) using SR-nanoCT.

3. Subsequently, samples were fixed and dehydrated in a graded series of alcohol (70%, 96% and 100% ethanol, immersion for 24 h in each solution) and embedded in polymethylmethacrylate (PMMA).

4. The specimens were carefully ground off and polished in steps of approximately 10 µm in the direction perpendicular to the x_3-axis to a region 50-100 µm above and/or below the region scanned by means of SR-nanoCT. In this way, data acquisition on tissue regions potentially damaged by high radiation doses were avoided in subsequent SAM and PRS experiments.

5. PRS and SAM were performed on the same tissue regions of the polished sample surfaces.

6. Finally, tomographic, spectroscopic and acoustic data were registered and site-matched data correlated.

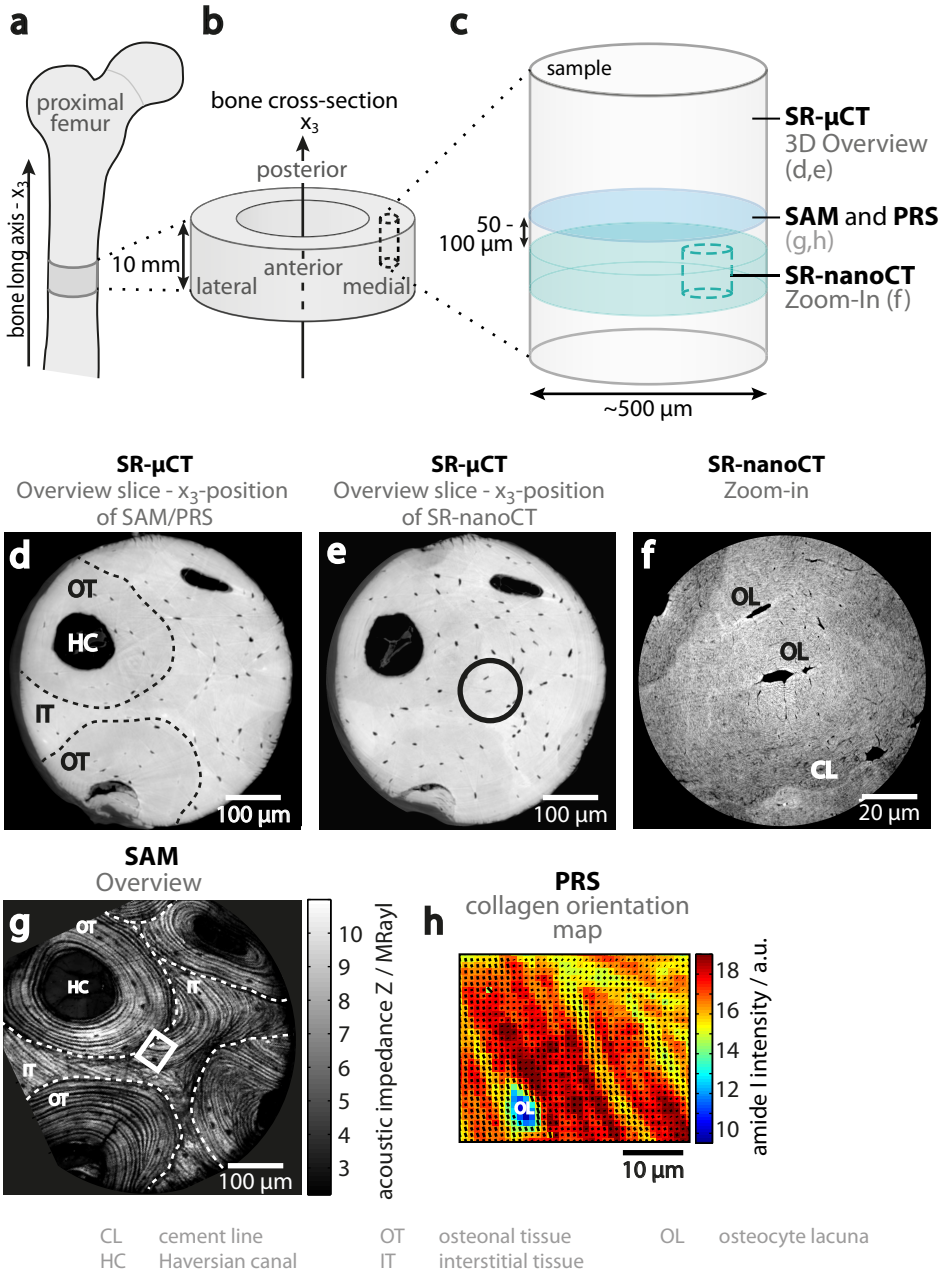

Figure 3.13: Sample preparation and measurement protocol. (a) Schematic of the proximal end of the human femur. The approximate location of the sample dissection within the diaphysis of the femur is indicated. (b) Illustration of the cortical bone cross-section with the cylinder displaying the final sample selected for imaging. (c) Overview of the locations of serial SR-µCT, SR-nanoCT, SAM and PRS imaging measurements on the final sample. (d) Exemplary SR-µCT overview image slice at the x_3-position of acoustic and Raman spectroscopic imaging. Osteonal and interstitial tissue domains are marked. (e) SR-µCT image slice at the x_3-position of SR-nanoCT. The black circle indicates the location of the SR-nanoCT image slice shown in (f). (g) SAM overview image of the sample slice shown in (d). The white rectangular indicates the location of the subsequent PRS measurement. (h) Collagen orientation map derived by means of PRS indicating the orientation of the collagen fibrils. Color code, length and orientation of the black arrows represent the average, normalized intensity of the amide I band, the fibril orientation in the lamellar plane and in the surface plane, respectively. Image adapted from [165] with permission from Elsevier.

Image Acquisition

Synchrotron X-ray Phase Contrast Micro and Nano Tomography

SR-µCT and SR-nanoCT experiments were carried out at the nano-imaging beamline ID22-NI at the European Synchrotron Radiation Facility (ESRF, Grenoble, France). Data acquisition and image reconstruction were performed as previously described by Langer et al. [91] (Image reconstruction courtesy of Bernhard Hesse.). Image processing, i.e. analysis of the fibrillar orientation, was done as described by Varga et al. [13]. (Quantitative 3D fibrillar orientation analysis courtesy of Peter Varga.)

Briefly, a X-ray beam energy of 16.874 keV was selected for phase contrast tomography experiments, enabling sufficient transmission and high mass density contrast. As indicated above, SR-µCT overview scans with a cylindrical field of view of 715 µm in diameter and height, imaging the whole sample cross-section, were first acquired at an isotropic voxel size of 350 nm (Fig. 3.13d,e). To minimize the delivered radiation dose, the number of projections was limited to 1200, each with 0.2 s exposure time. A spatial resolution of ~2 µm was achieved in SR-µCT scans. The resolution was estimated based on lined profiles across several sharp interfaces between mineralized and nonmineralized bone tissue regions on grayscale images. The FWHM of the first derivatives of these line profiles was considered to represent the spatial resolution of 3D overview scans.

Subsequently, overview scans were examined to select VOIs for SR-nanoCT analysis. SR-nanoCT imaging was performed by recording a series of tomographic radiographs at 2999 projection angles, each with an exposure time of 0.2 s, at four different distances between sample position and focal spot (Fig.2.10). Next, X-ray phase maps were retrieved from the corresponding projections of the four distances. By means of the filtered back projection algorithm, the distribution of the refractive index decrement δ_n was reconstructed and stored in units of $2\pi/\lambda$ (with λ =0.735 Å). 3D SR-nanoCT scans with an isotropic voxel size of 50 nm and a cylindrical field of view of about 100 µm in diameter and height were collected (Fig. 3.13f). As indicated in Sec. 2.2.3, the refractive index decrement δ_n is proportional to the electron density. It can be converted into mass density values by means of the following approximation:

$$\delta_n \approx 1.3 \cdot 10^{-6} \rho \lambda^2 \tag{3.2}$$

with λ in units of Åand ρ in units of g/cm^3 [91]. The spatial resolution was estimated by calculating the first derivative of several line profiles across sharp interfaces between mineralized and nonmineralized tissue regions (Fig. 3.14). Accordingly, a spatial resolution of ~250 nm was achieved in SR-

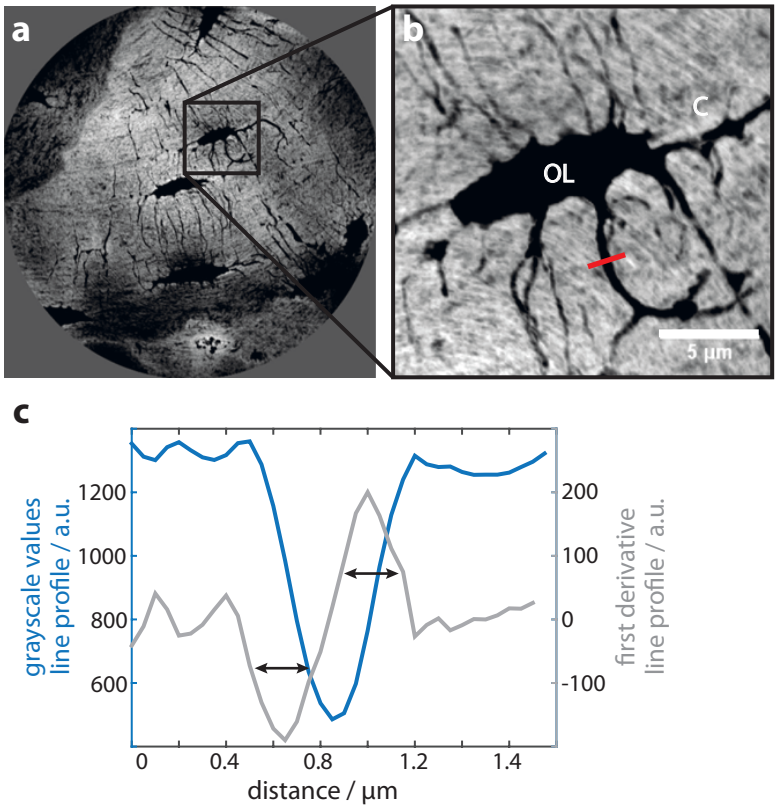

Figure 3.14: Upper limit estimation of the spatial resolution of SR-nanoCT measurements. (a) Maximum intensity projection of 100 SR-nanoCT slices. The image shows various osteocyte lacunae interconnected by canaliculi. Three tissue domains can be distinguished. (b) Zoom-in section showing a single osteocyte lacuna (marked with OL) and canaliculi (marked with C) marked. The red line indicates the location of an exemplary line profile. The line profile (blue) and the corresponding first derivative (gray) are displayed in (c). In this study, the spatial resolution of the SR-nanoCT measurement was defined as the FWHM of the first derivative, which is indicated with the black arrows.

nanoCT measurements. The 3D SR-nanoCT data sets provided sufficient spatial resolution and sensitivity to mass density fluctuations that characteristic fibrillary patterns could be identified, even though single mineralized collagen fibrils could not be resolved [13, 158]. As increased crack occurrence and propagation was observed in close proximity to the Haversian canal, SR-nanoCT measurements were conducted in interstitial tissue domains with sufficient distance to Haversian canals.

Polarized Raman Spectroscopy

Raman spectroscopic measurements were conducted as described in Sec. 3.1.2 using the same experimental confocal Raman setup. The laser power was set to 45 mW. To exclude surface topography-related artefacts, the laser beam

was focused to a spot approximately 5-10 µm beneath the sample surface. The tissue regions imaged beforehand by means of SR-nanoCT and SAM were scanned in mapping mode. Mapping was performed in steps of 1 µm, each with a signal integration time of 0.2 s. Each ROI was scanned repeatedly at varying angles of polarization β of the incident laser from $\beta = 90°$ to $\beta = -90°$ with $\Delta\beta = 15°$. Experimental control and spectral data processing were done using the ScanCtrlSpectroscopyPlus (version 1.38, WITec, Ulm, Germany) and WitecProjectPlus (version 2.02, WITec, Ulm, Germany) software packages, respectively.

Background fluorescence was subtracted from PRS bone spectra. Five Raman bands were analyzed: (i) the phosphate band ν_1 (PO_4^{-3} symmetric stretch at 960 cm^{-1}), (ii) the phosphate band ν_2 (PO_4^{-3} symmetric bending at 440 cm^{-1}), (iii) the carbonate band (CO_3^{-2} symmetric stretch at 1075 cm^{-1}), (iv) the amide I band (C=O stretch at 1660 cm^{-1}), and (v) the amide III band (C-N vibration at 1250 cm^{-1}) (illustrated in Fig. 2.4). Based on the analysis of these bands, four tissue properties were investigated: (a) the collagen orientation was derived by analysis of the anisotropic intensity variation of the amide I band intensity as a function of angular polarization modulation of the incident laser, following the protocol presented in Sec. 3.1, (b) the compositional mineral-to-matrix-ratio (MTMR) reflecting on the relative tissue mineralization, (c) the carbonate-to-phosphate-ratio (CTPR) associated to type-B carbonate substitution, and (d) the mineral crystallinity related to the crystal lattice order. A detailed list of the tissue parameters and their spectral derivation is summarized in Table 3.2. Note that the spectroscopic data of all Raman bands at every image pixel were average values of 13 Raman spectra recorded at different angles of polarization of the incident laser.

Scanning Acoustic Microscopy

The principles of SAM are described in detail in Sec. 2.2.2. In this study, SAM measurements were conducted following the protocol presented by Raum et al. [40]. Imaging was performed using a KSI SAM 2000 (Krämer Scientific Instruments, Herborn, Germany) equipped with a broadband lens (1.3 - 2 GHz) characterized by a semi-aperture angle of 50°. The acoustic lens was excited at a frequency of 1.3 GHz and a burst length of 20 ns. Distilled, degassed water was used as a coupling fluid. The water temperature was controlled and fixed at 23°C. Using this confocal setup, an interaction volume of approximately 1 µm and 3.3 µm between focused ultrasound and sample surface in lateral and axial directions was achieved, respectively. 15-20 two-dimensional (2D) scans (C-scans) parallel to the sample surface were acquired stepwise at gradually decreasing transducer-sample distances at a step increment of 1 µm. Each C-scan was recorded by displacing the transducer

Table 3.2: Assessment of fiber orientation, compositional and physicochemical tissue properties from PRS bone spectra.

Parameter	Analyzed spectral range [cm^{-1}]	Parameter calculation and description
collagen orientation	~ 1610-1700 (amide I band)	**Amide I anisotropy analysis** as a function of the laser polarization as introduced in Sec. 3.1. The amide I peak at every polarization angle was fitted (Gauss) and normalized to the intensity of the amide III band to account for slight fluctuations of the laser power. The average amide I signal is maximal for a fibril conformation parallel to the laser and minimal when the fibrils are oriented perpendicular to the laser. Note that the average amide I intensity investigated in this section, refers to the mean amide I value of all spectra collected at varying polarization at a specific location.
mineral-to-matrix-ratio (MTMR)	~ 410 - 460 ($\nu_2\ PO_4^{3-}$) ~ 1215 - 1290 (amide III)	**Intensity ratio of $\nu_2\ PO_4^{-3}$ / amide III** Information about the degree of mineralization of the collagen matrix (Sec. 2.2.1). An increasing MTMR indicates an augmenting local mineral content per amount of collagen. The MTMR was calculated from the ratio of the integrated peak areas of the $\nu_2\ PO_4^{3-}$ band to the amide III band.
carbonate-to-phosphate-ratio (CTPR)	~ 1060 – 1100 $\nu_1\ CO_3^{-2}$ ~ 410 – 460 ($\nu_2\ PO_4^{3-}$)	**Area ratio of carbonate $\nu_1\ CO_3^{-2}$ / $\nu_2\ PO_4^{-3}$** Type-B carbonate substitution (Sec. 2.2.1). An increasing CTPR reflects on a growing number of carbonate ions in hydroxyapatite crystallites. The CTPR was determined by calculation of the ratio of the integrated peak areas of the $\nu_1\ CO_3^{-2}$ band to the $\nu_2\ PO_4^{3-}$ band.
crystallinity	~ 930 - 980 ($\nu_1\ PO_4^{3-}$)	**Inverse FWHM of $\nu_1\ PO_4^{-3}$** Measure of the crystal lattice order (Sec. 2.2.1). A decreasing bandwidth indicates greater crystallinity. The crystallinity was calculated as the FWHM of the Gaussian fitted $\nu_1\ PO_4^{3-}$ peak.

over the specimen surface in steps of 0.4 µm. At each scan point, the amplitude $V(x_1, x_2, x_3)$ of the reflected acoustic signal was registered. Like this, a 3D data set $V(x_1, x_2, x_3)$ was formed, enabling reconstruction of the confocal reflection amplitude at every scan point using the Multi-Layer-Analysis software introduced by Raum et al. [40]. The acoustic microscope was calibrated using homogeneous reference samples (polymethylmethacrylat, titanium). Based on the calibration, the confocal reflection amplitude measured from the investigated bone sample surface was converted into acoustic impedance values Z (Fig. 3.13).

Data Analysis and Image Registration

The measurements from the four imaging modalities were acquired at different voxel and pixel sizes, i.e. 350 nm voxel size for SR-µCT, 50 nm voxel size for SR-nanoCT, 1 µm pixel size for PRS, and 0.4 µm pixel size for SAM. In order to facilitate pixelwise comparison between PRS and SAM, PRS maps were upsampled to a pixel size of 0.4 µm. PRS and SAM data were compared to SR-nanoCT images by means of site-matched line profiles. For this comparative analysis, pixel sizes of PRS and SAM and SR-nanoCT were 0.4 µm and voxel sizes of SR-nanoCT were 50 nm.

Spatial image registration of PRS, SAM, and SR-nanoCT data was done using ImageJ (National Institutes of Health, Bethesda, MD, USA) and custom-developed scripts in Matlab (Math-Works Inc., Natick, MA, USA). Prominent bone tissue features, visible with all modalities, such as the Haversian canals, cement lines, osteocyte lacunae, and the geometric shape and dimension of the specimen were considered reference points in the registration procedure. The registration-based data transformation was based on relative translation, rotation, and scaling between the images.

Statistics

Average tissue parameters of osteonal and adjacent interstitial tissue domains were compared by means of statistical analysis. The statistical analysis was carried out using Matlab (Math-Works Inc., Natick, MA, USA). Student's t-test was applied to compare the outcomes of all investigated domains. Statistical results were considered significant for p-values less than 0.05.

3.2.3 Theoretical Simulations

Lamellar Distribution of Acoustic Impedance Values

Previous studies [167] have provided proof that the mineralized collagen fibrils in bone exhibit a transverse isotropic elastic behavior. Therefore the ap-

parent stiffness of the collagen fibril is crucially determined by local fibril orientation. At a specific angle of fibril inclination φ with respect to the osteonal axis x_3, the apparent stiffness of the mineralized collagen fibrils can be derived by rotation of the transverse isotropic stiffness tensor (Eq. 2.20) in the x_1x_3 plane [138, 168]

$$c(\varphi) = c_{11}\cos^4(\varphi) + 2\,(c_{13} + c_{44})\sin^2(\varphi)\cos^2(\varphi) + c_{11}\sin^4(\varphi). \tag{3.3}$$

Recalling Eq. 2.36, the acoustic impedance is defined as the square root of the local mass density and the local apparent stiffness $c(\varphi)$. Consequently, the acoustic impedance tensor is also expected to exhibit a transverse isotropic behavior. In tissues with homogeneous mass density distribution, relative variations of the acoustic impedance values are determined by alterations of the apparent stiffness $c(\varphi)$. Within the frame of this thesis, the complete set of elastic stiffness coefficients c_{ii} could not be directly measured at a resolution of 1 µm. Therefore, the following non-linear empiric regression function, determined by Preininger et al. [169], was used for the conversion of apparent stiffness and acoustic impedance Z values:

$$c(\varphi) = 0.608 * (Z(\varphi) \,/\, 1\,MRayl)^{1.923} * 1\,GPa. \tag{3.4}$$

For the theoretical simulations of the apparent acoustic impedance Z, a set of four independent elastic stiffness coefficients ($c_{11} = 15.6\,GPa$, $c_{33} = 25.6\,GPa$, $c_{13} = 8.8\,GPa$, and $c_{44} = 3.4\,GPa$) determined by means of high frequency SAM by Raum et al. [98] were used. Eqs. 3.3 and 3.4 were employed to estimate the the apparent acoustic impedance Z as a function of varying fibril orientation φ in lamellae organized as twisted and oscillating plywood pattern (Fig. 3.15a). By means of non-parametric smoothing kernel density estimation [6], the probability density functions of the acoustic impedance values of the two lamellar patterns were estimated (Fig. 3.15b). More precisely, estimated cumulative density functions (cdfs) of the acoustic impedance Z were simulated for twisted, oscillating, and coexisting twisted and oscillating plywood patterns with constant sublayer thickness. The analysis showed that both twisted and oscillating plywood patterns exhibited bimodal density functions (indicated by black and gray arrows). Interestingly, coexisting oscillating and twisted motifs featured a trimodal shaped density function (indicated by blue arrows).

[6] Related to standard histogram analysis, kernel density estimation allows for determination of the probability distribution of a data set. In contrast to standard histogram analysis, kernel density estimation provides smooth and continuous probability distributions.

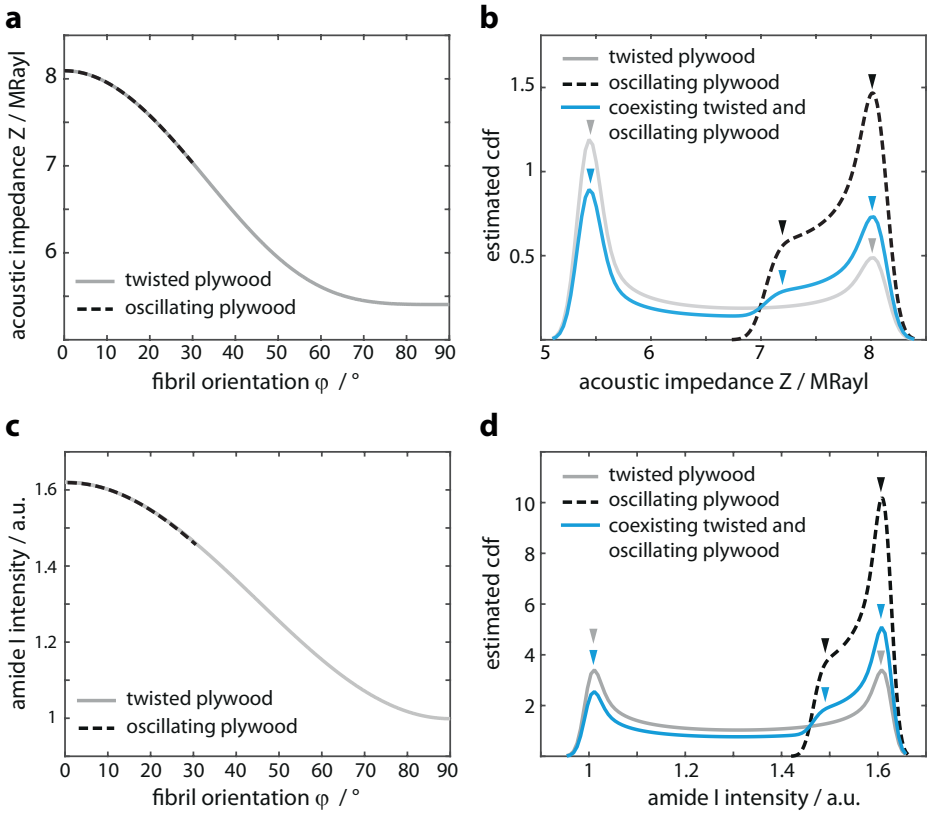

Figure 3.15: Theoretical simulation of the apparent acoustic impedance and the average amide I intensity values of different lamellar organizations. (a) Theoretical apparent acoustic impedance as a function of the fibrillar orientation φ. (b) Estimated cumulative density function (cdf) of the apparent acoustic impedance values for lamellae organized as twisted, oscillating, and coexisting twisted and oscillating fibril patterns. (d) Theoretical average amide I intensity as a function of the fibrillar orientation φ. (d) Estimated cumulative density function (cdf) of the average amide I intensity values for lamellae organized as twisted, oscillating, and coexisting twisted and oscillating fibril patterns. Image reprinted from [165] with permission from Elsevier.

Lamellar Distribution of Amide I Values

Similar to the acoustic impedance, the amide I intensity value probability distribution was estimated for lamellae with different organization patterns. Based on the theoretical simulations of Galvis et al. [36] (summarized in detail in Sec. 3.1), the average amide I intensity was theoretically approximated as a function of the fibril orientation φ (Fig. 3.15c). Using this relation, non-parametric smoothing kernel density estimation was applied to derive the estimated cdf of the average amide I intensity for lamellae with different fibrillar organization patterns (Fig. 3.15d). The theoretical simulation predicted a bimodal value distribution for oscillating and twisted plywood patterns (indicated by black and gray arrows) and a trimodal shaped cumulative

density distribution for coexisting oscillating and twisted plywood patterns (indicated by blue arrows).

3.2.4 Results and Discussion

Synchrotron X-ray Phase Contrast Micro and Nano Tomography

The specimen volumes were completely scanned using SR-μCT to provide 3D overview scans. The 3D images allowed for identification of typical structural bone features such as Haversian canals and osteocyte lacunae. Different gray values enabled for discrimination of osteonal and interstitial tissue domains (exemplary marked in Fig. 3.13d). Within single tissue domains, relatively homogeneous gray values were found and lamellar patterns were not observed. Subsequently imaged 3D SR-nanoCT data sets could be allocated to the corresponding tissue regions within SR-μCT overviews (Fig. 3.13e and f). SR-nanoCT scans resolved structural details including osteocyte lacunae, canaliculi, and cement lines (Fig. 3.13f). Mass density ρ distribution were derived for two interstitial tissue domains (Table 3.3). Mass density variation and cement lines allowed for allocation of osteonal and interstitial tissue domains. Moreover, using the analysis based on the autocorrelation function proposed by Varga et al. [13], the lamellar patterns of the quantified interstitial tissue regions were investigated (ROI of sample A shown in Fig.3.20c, d). The analyzed interstitial lamellae were organized in two patterns: (i) a smooth oscillatory pattern closely around the x_3 axis, with an oscillation amplitude $\varphi = -22.7 \pm 7.5°$ (sample A) and $\varphi = 28 \pm 3.9°$ (sample B) and (ii) a continuous 180° rotation (sample A). These observations were in good agreement with the findings of Varga et al. [13]. Accordingly, the fibrillar twists were identified as oscillating and twisted plywood patterns, respectively.

Scanning Acoustic Microscopy

Similar to SR-μCT overviews, acoustic impedance maps displayed characteristic structural bone features such as Haversian canals and osteocyte lacunae (Fig. 3.13g and Fig. 3.13). In contrast to SR-μCT overviews, acoustic images exhibited the characteristic concentric bone lamellae, characterized by oscillating high and low acoustic impedance values (Fig. 3.13g, Fig. 3.16b, d). Mean values of all imaged osteonal and interstitial tissue domains were determined and converted into stiffness values c according to Eq. 3.4 (Table 3.3). Clearly, osteons featured significantly smaller mean acoustic impedance values than directly adjacent interstitial tissue domains ($p < 0.01$). These findings were in well agreement with earlier studies investigating the microelastic tissue properties of human cortical tissue domains with respect to the tissue age using SAM [67, 127] and nanoindentation [44]. Similar to the presented results, the authors of these studies found significantly elevated elastic stiff-

Table 3.3: Average tissue parameters of all investigated osteonal (OT) and interstitial (IT) tissue domains. P-values of Student's t-test comparison between osteonal and interstitial regions are listed.

Sample ID / ROI	Acoustic Impedance Z [MRayl]	Apparent stiffness C [GPa]	Mineral-to-Matrix-ratio (MTMR) [a.u.]	Carbonate-to-Phophate-ratio (CTPR) [a.u.]	Crystallinity [cm]	Mass density ρ [g/cm³]
sample A / OT-1	5.4 ± 1.2	15.6	1.71 ± 0.08	1.00 ± 0.05	0.0416 ± 0.0004	-
sample A / OT-2	4.7 ± 1.7	16.7	1.70 ± 0.08	1.08 ± 0.03	0.0409 ± 0.0003	-
sample A / IT-1	6.8 ± 2.2	24.3	1.92 ± 0.08	0.98 ± 0.04	0.0424 ± 0.0004	1.81 ± 0.16
sample A / IT-2	7.2 ± 1.8	27.1	2.39 ± 0.17	0.98 ± 0.04	0.0424 ± 0.0004	-
sample B / IT-1	7.2 ± 1.2	27.1	2.40 ± 0.14	0.80 ± 0.07	0.0412 ± 0.0005	2.00 ± 0.16
sample B / IT-2	7.0 ± 0.7	25.6	-	-	-	-
sample B / IT-3	6.7 ± 0.9	23.6	-	-	-	-
sample C / OT-1	4.9 ± 1.2	13.0	1.88 ± 0.09	1.06 ± 0.05	0.0427 ± 0.0003	-
sample C / IT-2	7.6 ± 2.5	30.0	2.34 ± 0.10	1.03 ± 0.03	0.0438 ± 0.0002	-
sample D / OT-1	5.8 ± 1.4	17.8	1.71 ± 0.11	1.10 ± 0.64	0.0270 ± 0.0004	-
sample D / OT-2	5.6 ± 1.5	16.7	-	-	-	-
sample D / OT-3	7.2 ± 1.8	27.1	-	-	-	-
p-value	< 0.01 **		0.01 *	0.10	0.28	

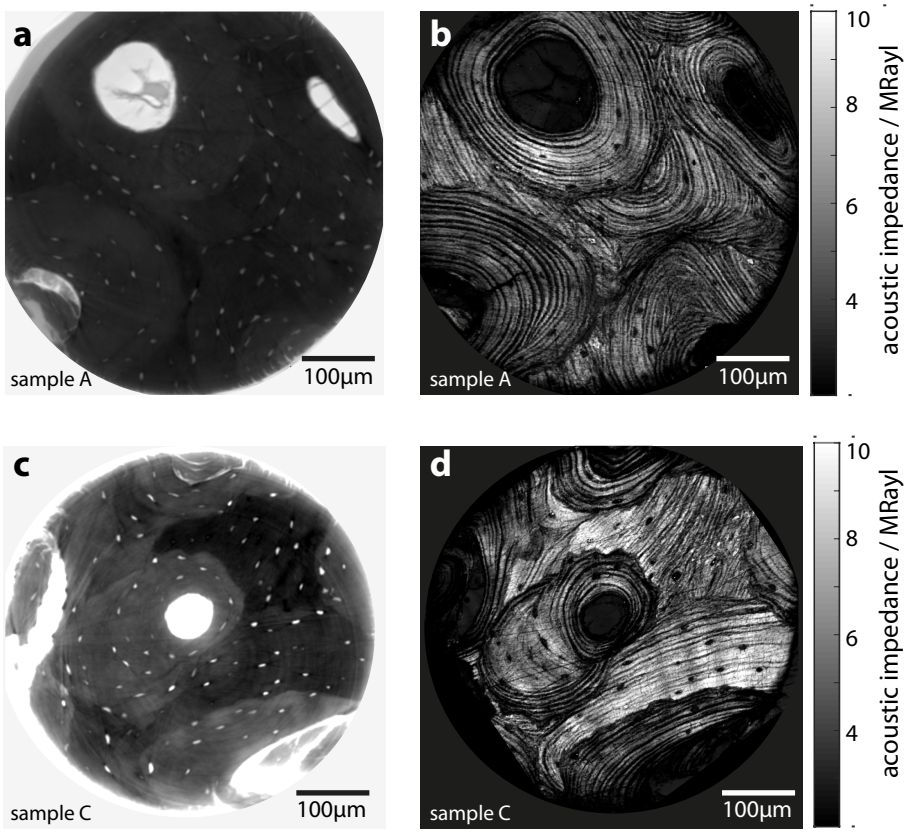

Figure 3.16: Corresponding SR-µCT and acoustic overview images. Exemplary SR-µCT image slices (a, c) and corresponding acoustic impedance overview maps (b, d) of sample A and C, respectively.

ness values in interstitial tissue domains in comparison to osteons.
It is worth noting that several interstitial tissue regions of different samples were imaged that were characterized by relatively high acoustic impedance Z values, but exhibited lamellar patterns that were much less pronounced and not clearly recognizable.

Allocation of acoustic images to corresponding SR-µCT image slices was done based on the location of Haversian canals and osteocyte lacunae as well as the contour of osteonal and interstitial domains. Fig. 3.16 exemplarily shows the result of the image registration process of two samples. The image registration enabled identification of the lamellae analyzed by means of SR-nanoCT in the acoustic images.

Polarized Raman Spectroscopy

The tissue regions analyzed by means of SAM were further analyzed using PRS to investigate the fibril orientation, the MTMR, the CTPR and the min-

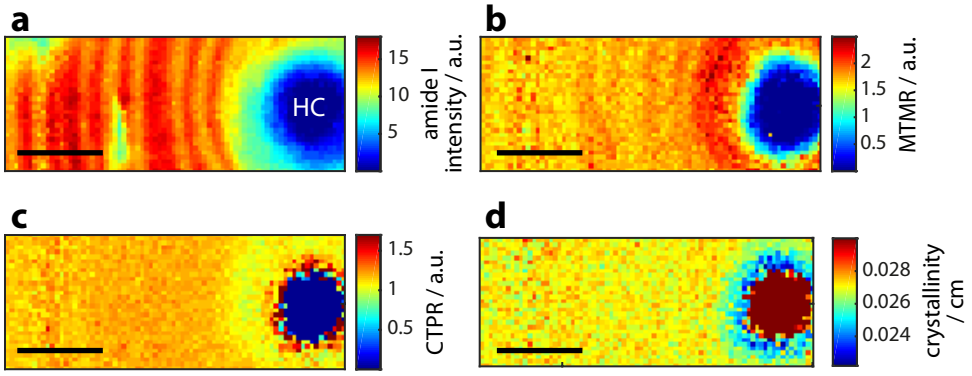

Figure 3.17: Raman tissue parameter maps. Exemplary parameter maps of the same osteonal tissue region (sample D). (a) Average amide I intensity, displaying the lamellar tissue character of cortical bone; In contrast, mineral-to-matrix ratio (MTMR) (b), carbonate-to-phosphate-ratio (CTPR) (c), and crystallinity (d) displayed relatively homogeneous value distributions. Scale bar is 20 µm. Image reprinted from [165] with permission from Elsevier.

eral crystallinity. Fig. 3.17 depicts an example of corresponding parameter maps of the same tissue region, displaying the four PRS parameters. The average amide I intensity map exhibited periodically oscillating value distributions (Fig. 3.13h, Fig. 3.17a, Fig. 3.18b). In sharp contrast, MTMR, CTPR, and crystallinity showed relatively homogeneous value distributions and did not reflect the lamellar character of the tissue (Fig. 3.17c, d, e). Average values of MTMR, CTPR and crystallinity of all analyzed tissue domains were determined (Table 3.3).

In comparison, interstitial tissue domains were characterized by significantly higher MTMR values than adjacent osteonal regions ($p = 0.01$). The elevated levels of the MTMR indicate a higher degree of mineralization in interstitial domains than in osteons. This finding is in good agreement with several other studies analyzing the MTMR with respect to the tissue age by means of vibrational spectroscopy [68, 69]. Furthermore, these findings are in line with the higher degree of mineralization in relation to increased tissue age as demonstrated by means SR-µCT [67] and qBEI [39].

CTPR were slightly but consistently elevated in osteons in comparison to adjacent interstitial tissue regions. Nevertheless, the difference between osteonal and interstitial domains was statistically not significant ($p = 0.10$). In relation to the local tissue age, the type-B carbonate substitution in bone mineral crystals remains contradictory in literature. In contrast to the presented analysis, Boskey et al. [68] and Petra et al. [170] reported higher CTPR values with increasing tissue age based on FTIR measurements. However, in line with the results presented in this thesis, a decrease of the ratio as a function

of tissue age was described by Paschalis et al. [80] also using FTIR. These results are furthermore confirmed by Kazanci et al. [42], reporting higher CTPR in osteons than in directly adjacent interstitial domains by means of PRS imaging at single laser polarizations. Moreover, reviewing several FTIR based studies, Fratzl et al. [51] provided the proposition that the relative amount of carbonate in hAp particles reflects the mineral maturity. According to their review, decreasing levels of carbonate are to be expected with increasing mineral maturity.

Finally, analysis of the crystallinity demonstrated a consistent trend of moderately higher crystallinity values in interstitial tissue domains compared to directly adjacent osteons. This difference was not considered statistically different ($p=0.28$). As indicated in Sec. 3.1, bone mineral crystallinity is related to both, the apatite crystal size and the perfection in the apatite unit cell, as carbonate may substitute for phosphate in the lattice structure [78]. Therefore, bone crystallinity is closely related to the CTPR. The presented results were in line with several studies reporting a positive correlation of crystallinity and tissue age in human and baboon bone using FTIR [68, 69]. Similarly, a study on synthetic carbonated apatites reported increased mineral crystallinity accompanied by reduced carbonate substitution [115]. These observations on synthetic carbonated crystals were in good agreement with the presented results of CTPR and crystallinity in lamellar bone.

Finally, it can be assumed that not only the degree of mineralization, but also the size and / or the degree of crystallinity of mineral particles are increased in older interstitial tissue domains in comparison to adjacent younger osteonal regions. In summary, the presented findings illustrate the different levels of mineralization and mineral maturity that coexist in the individual tissue domains, i.e. osteonal and interstitial regions of cortical lamellar bone. In other words, not only the amount of mineral, but also the state of mineral maturity, defined by the size and purity of the apatite crystals, depend on the local tissue age and vary within cortical lamellar bone.

Point-by-Point Correlation Analysis

To determine the mutual relationships between the acoustic impedance Z and the PRS tissue parameters, parameter maps were site-matched and underwent a point-by-point correlation analysis. As an example, a pair of registered acoustic and PRS maps and the corresponding correlation analysis are displayed in Fig. 3.18. Panels a and b show the acoustic impedance Z and the amide I intensity of the same osteonal tissue region. Comparison between both maps highlights that the imaged lamellar patterns visible in both parameter maps coincide. In particular, this consistency is apparent in the

zoomed-in images (Fig. 3.18a-I, b-I). For quantitative parameter correlation analysis, osteocyte lacunae and obvious surface defects in the acoustic image (such as scratches or cracks) were excluded. The analysis demonstrated a positive correlation between acoustic impedance Z and amide I intensity (Fig. 3.18c).

As mentioned in the previous subsection, MTMR, CTPR, and crystallinity did not reflect the lamellar tissue character, but exhibited relatively homogeneous value distributions. No substantial correlation was found between acoustic impedance Z and PRS-based MTMR, CTPR, and crystallinity, respectively (Fig. 3.18 d-f). In line with these findings, lack of correlation was observed between amide I intensity and MTMR, CTPR, and crystallinity, respectively (Fig. 3.18 g-i). Additionally, proof was found that MTMR, CTPR, and crystallinity were not correlated within single tissue domains (Fig. 3.18j, k).

The mutual parameter correlation presented in Fig. 3.18 was confirmed by the analysis of the other investigated osteonal tissue regions. The correlation between acoustic impedance Z and amide I intensity of pooled data sets from three osteons of different samples is presented in Fig. S4.1 of the supplementary materials.

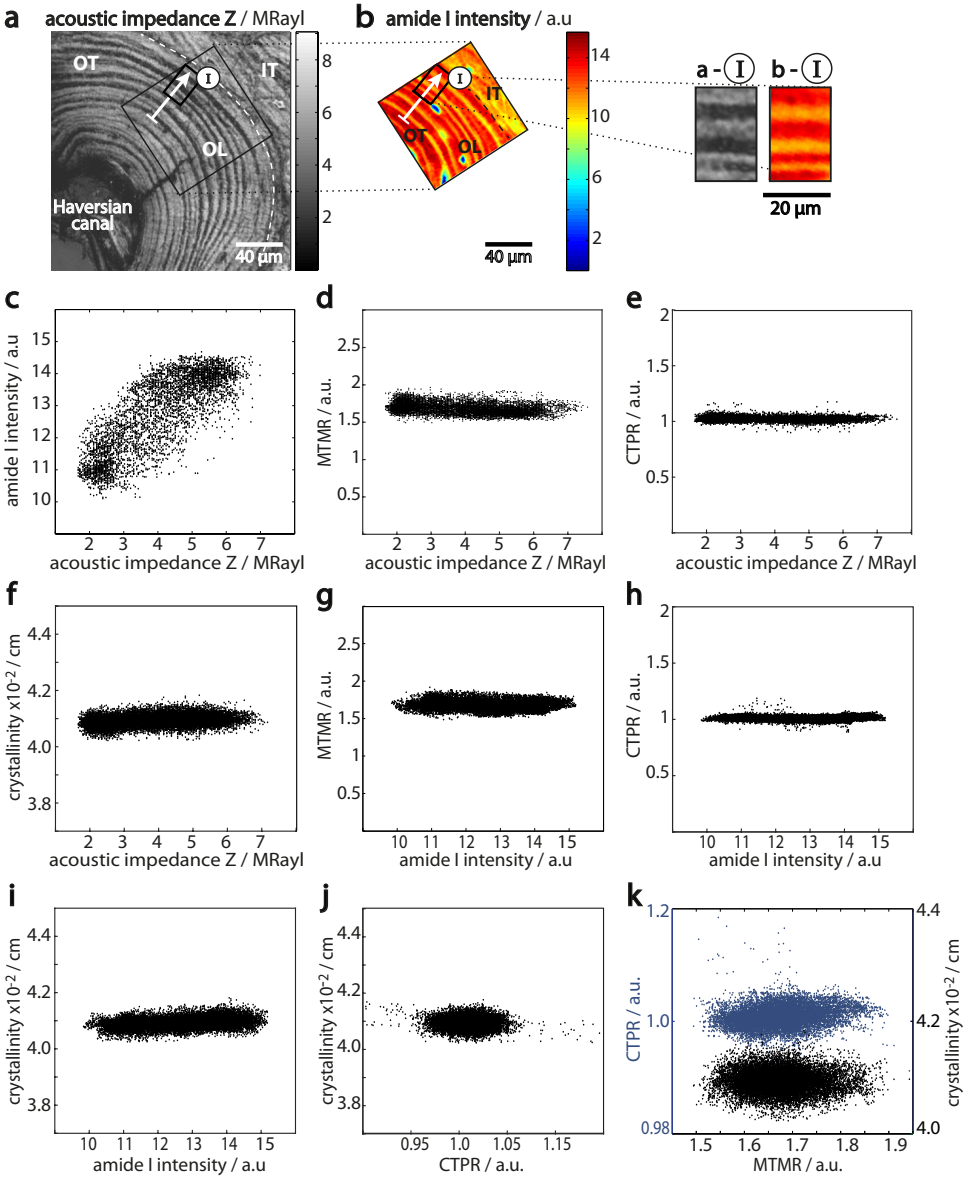

Figure 3.18: Spatial point-by-point correlation analysis. Example of an osteonal tissue region (sample A). (a) Acoustic impedance map. Osteonal and adjacent interstitial tissue region, Haversian canal and osteocyte lacunae are marked. A circumferential oscillating lamellar pattern of high and low impedance values Z is visible. (b) Site-matched amide I intensity image of the black rectangular ROI marked in (a). The osteonal lamellar pattern is also recognizable. (c-f) Correlation analysis between acoustic impedance Z and PRS tissue parameters. (f-k) Mutual correlation between different PRS tissue parameters. (k) Carbonate-to-phosphate-ratio (CTPR) vs. mineral-to-matrix-ratio (MTMR) (blue) and crystallinity vs. mineral-to-matrix-ratio (MTMR) (black). Image reprinted from [165] with permission from Elsevier.

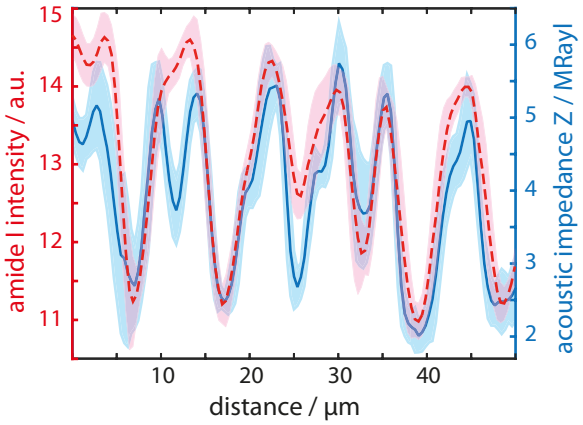

Figure 3.19: Comparative oscillation analysis of amide I intensity and acoustic impedance. Line profiles across several osteonal lamellae were analyzed. Each line profile represents mean values of 10 parallel profiles oriented perpendicular to the lamellar plane. Standard deviations are depicted. The location of the profiles is marked with the white arrows in Fig. 3.18a, b. Amide I intensity (red dashed line) and acoustic impedance Z (blue line) oscillated in phase and with very similar oscillation periods. Image reprinted from [165] with permission from Elsevier.

Lamellar Oscillation Analysis

By means of a comparative line profile analysis (Fig. 3.19) the lamellar oscillation characteristics of amide I intensity and acoustic impedance Z were further analyzed. The location of the line profiles is marked with the white arrows in Fig. 3.18a, b. Line profiles were derived as mean values of 10 parallel, adjacent profiles. The depicted profiles further demonstrated the matching oscillating characteristics of the two parameters. Very similar oscillation periods were observed for amide I intensity and acoustic impedance Z. Moreover, the oscillations were found to be in phase, though a slight, varying difference of oscillation amplitudes was observed in some lamellae.

The strong positive correlation and in-phase oscillation of the fibril orientation indicating amide I intensity and the acoustic impedance Z demonstrated in the presented parameter analysis suggested a high impact of the fibril orientation on the local elastic stiffness.

In sharp contrast, within single tissue domains the acoustic impedance Z was neither substantially correlated to the compositional MTMR, nor to the markers of mineral maturity, CTPR, and crystallinity. Consequently, these findings suggest that at the lamellar level, the impact of mineralization and mineral maturity on the undulating elastic properties may be negligible.

Comparative Line Profile Analysis

To provide further insight into the tissue characteristics of single bone lamellae, a comparative profile analysis on single bone lamellae on site-matched SR-nanoCT, PRS, and SAM data was conducted. The aim of this analysis was not only to investigate the tissue parameters on the level of single lamellae, but also to compare the fibril orientation analysis of SR-nanoCT and SAM. Two interstitial tissue domains were investigated. Fig. 3.20 (sample A / IT-1) exemplarily displays the site-matched profiles. Amide I intensity and acoustic impedance Z maps are depicted in Fig. 3.20a and b. The analyzed lamellae are marked with black and white rectangles, respectively. Fig. 3.20c shows a 3D simulation of the mineralized collagen fibril orientation of the analyzed lamellae derived by means of SR-nanoCT from two perspectives. The depicted line profiles (Fig. 3.20 d-i) were mean values of 15 line profiles oriented perpendicular to the lamellar plane and located within the rectangles.

SR-nanoCT-based orientation analysis revealed two fibrillar patterns in the investigated lamellae, an oscillating and a twisted plywood motif (Fig. 3.20 c, d). Whereas the oscillating plywood pattern was defined by fibrils smoothly oscillating between $\varphi = 0 \pm 2°$ and $\varphi = -22 \pm 7.5°$, the twisted plywood motif was defined by fibrils continuously twisting from $\varphi = 0 \pm 2°$ to $\varphi = 180 \pm 1°$. At this point it is important to recall that PRS and SAM test tissue properties on the sample surface. Therefore, amide I intensity and acoustic impedance Z reflect on the projection of the fibril orientation φ in the x_1x_2 plane (sample surface plane). Hence, as shown in the theoretical considerations (Sec. 3.2.3, Fig. 3.15a, c), a discrimination of the fibrillar twist direction cannot be provided by amide I and acoustic impedance Z data. To simplify the comparison of the 3D fibril orientation assessed by SR-nanoCT with the other tissue parameter line profiles provided by PRS and SAM, SR-nanoCT angles φ were projected to a range of $\varphi = 0°$ to $\varphi = -90°$ (Fig. 3.20d, red line). Analysis of the quantitative mass density values demonstrated a relatively homogeneous distribution of mass density across the investigated lamellae of $\rho = 1.8 \pm 0.2$ g/cm^{-3}. Mass density values did not reflect on the lamellar tissue character (Fig. 3.20e).

In contrast, the amide I intensity of the same lamellae featured periodic signal variations (Fig. 3.20f), characterized by four local intensity maxima and minima on a distance of 25 µm. In line with the results of the previous subsection, MTMR (Fig. 3.20g), CTPR, and crystallinity (Fig. 3.20i) were characterized by relatively uniform values across the lamellae (MTMR = 1.9 ± 0.3; CTPR = 0.98 ± 0.03; crystallinity = 0.042 ± 0.001 cm).

The acoustic impedance line profile exhibited periodically oscillating values. Maximum and minimum values of the acoustic impedance values along the profile were Z_{max} = 9.4 ± 0.4 MRayl and Z_{min} = 3.6 ± 0.5 MRayl, respectively. In good agreement with the amide I intensity variations, four local maxima and minima were detected along the profile of 25 µm length (Fig. 3.20h) that were colocalized with the local maxima and minima of the amide I intensity. Furthermore, the local maxima of amide I intensity and acoustic impedance Z coincided with the inflection points of the quantitative SR-nanoCT fibril orientation, i.e. $\varphi = 0°$. In other words, maximum amide I intensity and acoustic impedance values were measured for fibrils oriented parallel to the osteonal axis and perpendicular to the sample surface. Local minima of amide I intensity and acoustic impedance Z were colocalized with fibril orientations of $\varphi = -22.7°$ and $\varphi = -88°$ in oscillating and twisted lamellar segments, respectively. Consequently, the local minima of amide I intensity and acoustic impedance reflected on the fibrils with maximum deflection in each lamellar pattern. The comparative profile analysis of several lamellae in a second interstitial tissue domain (sample B / IT-1) confirmed the presented findings and is provided in the supplementary information (Fig. S4.2).

In summary, the comparative parameter profile analysis further confirmed that the compositional markers MTMR, CTPR, crystallinity, and local mass density were not affected by lamellar modulations. Based on these consistent findings, derived by means of two independent methodologies, a homogeneous tissue composition on the lamellar level is clearly demonstrated. However, it should be noted that in other studies using qBEI [39, 41] slight lamellar variations of the calcium content in human lamellar bone were reported.

The quantitative fibrillar orientation φ, the amide I intensity, and the acoustic impedance Z were periodically modulated in the analyzed line profiles. Moreover, the oscillation characteristics of amide I intensity and acoustic impedance Z exhibited comparable oscillation periods in phase with each other and with those of the quantitative fibril orientation φ. These findings clearly demonstrate the close relation of fibrillar orientation and local elastic properties. In line with the theoretical predictions of Galvis et al. [36], local maxima of the amide I intensity coincided with fibril orientations of approximately $\varphi = 0°$, parallel to the incident laser light and the osteonal axis x_3. As expected, these fibril orientations exhibited maximal acoustic impedance values. In line with theory, minima of the amide I intensity were allocated with the local maximal angular deflection angles within oscillating and twisted plywood patterns.

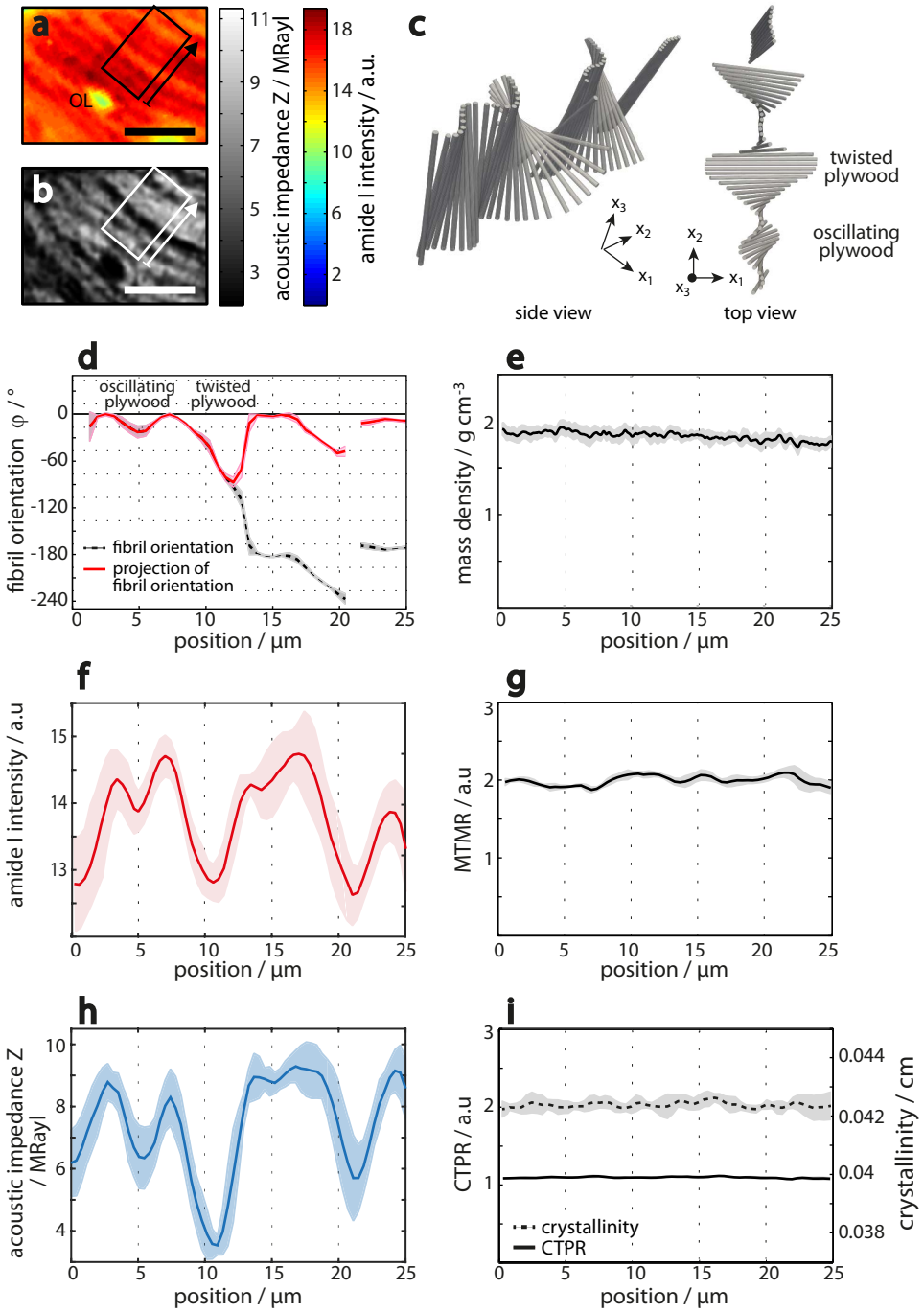

Figure 3.20: Comparative line profile analysis of several interstitial tissue lamellae by means of SR-nanoCT, PRS, and SAM. (a) PRS amide I intensity map. The black rectangle marks the investigated lamellae. The black arrow indicates the direction of the line profile analysis. (b) Corresponding acoustic image. Scalebar: 20 µm. (c) 3D illustration of the SR-nanoCT derived fibril orientation φ of the investigated lamellae. (d) Profile analysis of the ROI displaying mean and standard deviation of the 3D quantitative fibril orientation φ (black line) and the corresponding projection (red line). (e) Line profile of the mass density distibution of the investigated lamellae. Corresponding profiles of PRS tissue parameters of the same lamellae (f,g,i) and acoustic impedance Z (h). Image reprinted from [165] with permission from Elsevier.

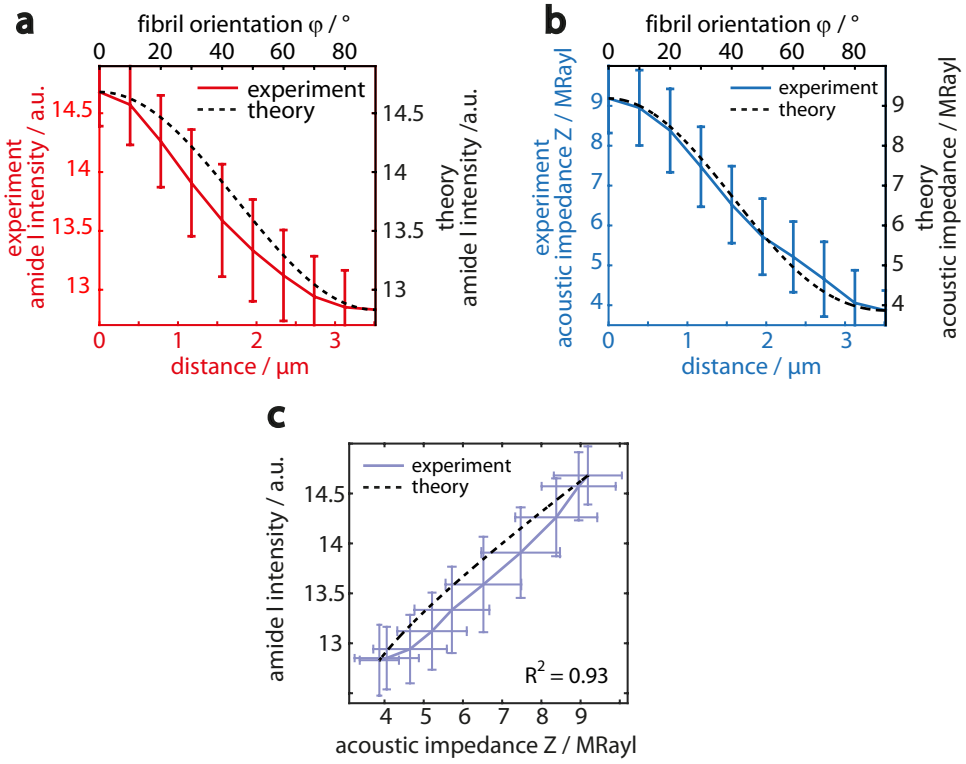

Figure 3.21: Comparison of experimental and theoretically simulated amide I intensity and acoustic impedance of a continuous and full fibril rotation in a twisted plywood motif. Experimental and theoretical amide I intensity (a) and acoustic impedance (b) value variation of a twisted plywood fibril arrangement. (c) Experimentally derived and theoretically predicted correlation of amide I intensity and acoustic impedance of a twisted plywood lamella. Image reprinted from [165] with permission from Elsevier.

Comparison of Theory and Experiment

Using quantitative SR-nanoCT characterization, a bone lamella organized as twisted plywood motif was selected to compare experimental amide I and acoustic impedance variations to theoretically expected value variations (as presented in Sec. 3.2.3). Based on the comparative line profile analysis presented in the previous subsection, segments of the amide I intensity and acoustic impedance profiles, corresponding to twisted plywood motifs as identified by SR-nanoCT, were selected. The local maximum and minimum values of the amide I intensity corresponding to fibril confirmations $\varphi = 0°$ and $\varphi = 90°$ served as input for the theoretical predictions of the amide I intensity as a function to the fibril orientation (Sec. 3.2.3), respectively. Note that a constant thickness of sublamellae was assumed in theoretical simulations. The results of the comparison between experimental and theoretical amide I intensity variations are depicted in Fig. 3.21a. Obviously, experimental data was consistent with theoretical considerations.

Similarly, acoustic impedance value variations were theoretically estimated for the same lamella. The local maximum and minimum values that corresponded to fibril confirmations $\varphi = 0°$ and $\varphi = 90°$ were assumed to reflect on the local Z_{11} and Z_{33} values of the acoustic impedance tensor, respectively. Theoretical and experimental acoustic impedance variations were found to be in excellent agreement (Fig. 3.21b).
Finally, experimental amide I intensity and acoustic impedance Z of the twisted plywood lamella were correlated and compared to the theoretical correlation of the two parameters (Fig. 3.21c). Experimental data and computational simulation were found to be in line ($R^2 = 0.93$).

Ultimately, these findings strongly suggest that the observed elastic modulations in osteonal and interstitial tissue domains are the result of changing fibrillar orientation, rather than compositional variations or modulations in the state of mineral particle maturity. This is in line with earlier conducted studies by Hofmann et al. [7] and Granke et al. [8]. Contrary to the presented propositions of this thesis are the findings of Spiesz et al. [75]. In their combined qBEI, nanoindentation, and quantitative polarized light microscopy study no substantial correlation of the measured indentation modulus with the degree of mineralization or the fiber arrangement was found. However, nanoindentation and polarized light microscopy may not have provided sufficient lateral resolution to investigate the correlations of composition, fibril orientation, and elastic properties at sublamellar level.

Tissue Domain Specific Value Probability Distribution Analysis

Next, a probability distribution analysis of osteonal and interstitial tissue domains was conducted. Note that in contrast to the comparative line profile analysis presented in the previous subsection, which focused on single lamellae, this analysis intended to characterize of entire tissue domains. As introduced in the theory subsection (Sec. 3.2.3), non-parametric kernel density analysis was applied to estimate the cumulative density functions (cdf) of amide I intensity and acoustic impedance Z of the investigated site-matched tissue domains (Fig. 3.22). Both parameters, amide I intensity and acoustic impedance Z, exhibited trimodal-shaped density distributions in the majority of the analyzed tissue domains (7 out of 7 and 5 out of 7 tissue domains, respectively). Fig. 3.22a and b depict the results of the kernel density analysis of the two parameters in a typical osteonal tissue region. The trimodal shape of the density distribution functions are emphasized with the black arrows.

To interpret these findings, theoretical and experimental considerations were taken into account. Theoretically, the estimated cumulative density functions were compared to the computationally simulated density functions de-

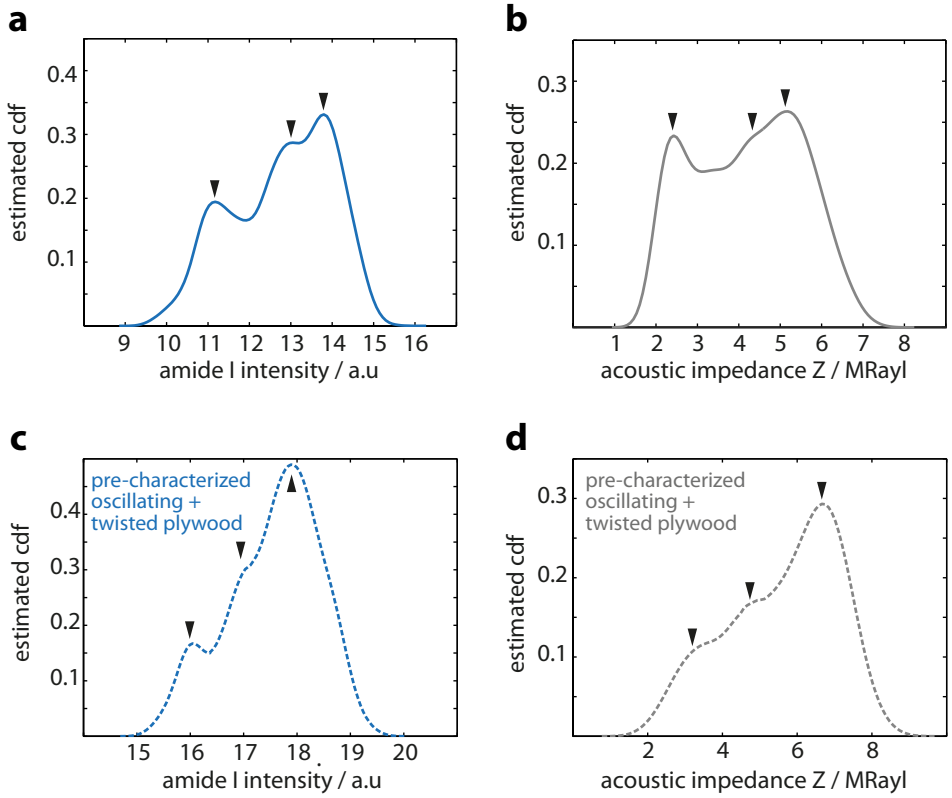

Figure 3.22: Value probability distribution analysis of amide I intensity and acoustic impedance of site-matched tissue domains. Exemplary cdfs of amide I intensity and acoustic impedance of an osteonal tissue region. The trimodal shaped density distribution is highlighted with the black arrows. (c,d) Estimated cdfs of an interstitial ROI comprising lamellae exhibiting oscillating and twisted plywood patterns identified by means of pre-characterization using SR-nanoCT. Image adapted from [165] with permission from Elsevier.

rived from various lamellar organization motifs presented in Sec. 3.22. Good agreement was found between the experiment-based density functions and theoretically simulated cumulative density functions of coexisting oscillating and twisted plywood patterns, as both exhibited trimodal shaped cdfs (Fig. 3.15). This match indicated that twisted and oscillating plywood organizations coexist in the majority of tissue domains. To experimentally verify these interpretations, a ROI comprising lamellae with twisted and oscillating plywood pattern identified by means of SR-nanoCT was selected for kernel density estimation. In line with the theoretical expectations, amide I intensity and acoustic impedance Z of this pre-characterized ROI exhibited a trimodal shaped cumulative density function (Fig. 3.15 c, d).

In summary, kernel density analysis of theoretically predicted and experimentally characterized oscillating and twisted plywood pattern consistently

featured trimodal shaped density functions. Consequently, it can be concluded that the majority of investigated tissue domains comprised lamellae organized in twisted and oscillating plywood arrangements. Note that lamellae organized as asymmetrical rotated plywood, in particular the 5-sublayer fibril arrangement pattern proposed by Weiner et al. [4], also provided a potential explanation for the observed trimodal shaped density functions, but was not consistent with the observations of the ROI experimentally characterized by means of SR-nanoCT.

Generally, the trimodal shaped amide I density function clearly indicated that the possible fibril conformations, i.e. fibril orientations in the range from $\varphi = 0°$ to $\varphi = 90°$, were not equally represented in the analyzed bone tissue domains. However, the presented findings provided evidence of predominant fibril orientations in lamellar bone. In particular, small angles ($\varphi \leq 30°$) were found to be notably well represented.

The similarity of shape and modality of amide I and acoustic impedance Z cumulative density function further confirm the close relationship between fibril orientation and local elastic tissue properties not only on the level of individual bone lamellae, but also on the level of entire tissue domains.

From a micromechanical point of view, these results provided a reasonable explanation for the anisotropic elastic properties of single bone lamellae reported by Franzoso et al. [130]. The evidence of coexisting plywood patterns in the majority of tissue domains may account for the different degrees of anisotropy observed by the authors. In future studies, the presence of predominant fibril orientations and the resulting apparent microelastic properties should be taken into account for computational modeling of the anisotropic elastic stiffness tensor.

Ultimately, in this study, the presented kernel density estimation of PRS-based amide I intensity maps emerged as a interesting and valuable tool, enabling a prompt overview of the fibril orientations and an easy identification of predominant orientations in a relatively large field of view. The main advantage of this method is availability and accessibility of PRS compared to SR-nanoCT. The PRS approach may be easily adapted for the analysis of other collagen-based biomaterials.

Study Limitations

At this point, several limitations of this study need to be mentioned, as they may have impacted data acquisition and interpretation of the reported results.

First, the presented study was limited by the small sample size and particularly by the low number of tissue domains analyzed by means of SR-nanoCT. As a result, comparative line profile analysis of the quantitative fibril orientation angles φ with the PRS-based tissue markers and the acoustic impedance Z was restricted to a low number of lamellae. Consequently, it could not be confirmed that the above reported results hold generally for a larger set of specimens. Moreover, it is likely that the small sample size may have had an impact on the statistical comparison of tissue domain specific parameters.

Second, there were several steps in the serial sample preparation and data acquisition protocol that may have potentially altered the bone tissue.
(i) The repetitive application of high dose synchrotron radiation required for SR-nanoCT tomographic phase reconstruction may have had a significant impact on the tissue structure and its mechanical properties [171]. To account for potential radiation damage to the tissue, PRS and SAM data acquisition was conducted 50-100 µm above and/or underneath the VOI imaged by means of SR-nanoCT. The limit of 100 µm in x_3-direction was chosen based on the findings of Varga et al.[13], who reported invariant fibril orientation angles in a range of 100 µm along the osteonal axis x_3 in their SR-nanoCT study. Nevertheless, the fibril orientation angles φ at the x_3 location of serial PRS and SAM measurements may have been slightly different than at the x_3 location of SR-nanoCT imaging (Fig. 3.13).
(ii) It was mandatory for specimen conservation to embed the native samples after the tomographic SR-µCT and SR-nanoCT characterization. Even though embedding was performed following a standard protocol, ethanol fixing and PMMA embedding process may have altered the elastic tissue properties. In an earlier study using nanoindentation, Busby et al. [172] demonstrated that PMMA embedded bone tissue exhibited increased indentation moduli in comparison to native bone tissue. The authors speculated that this observation may be explained by the replacement of water molecules by ethanol during dehydration and subsequently by PMMA molecules. Based on these findings, it can be assumed that PMMA embedding carried out in the presented study resulted in increased acoustic impedance values. However, it should be noted that in this thesis project, all specimens underwent the same preparation procedure and potential tissue alterations would have equally affected all samples. Therefore, relative comparison between samples, single tissue domains, and especially adjacent lamellae was considered reasonable. Still, the tissue embedding protocol should be taken into account for comparison of absolute acoustic impedance values with literature. The potential effects of tissue embedding on the Raman analysis of bone have been summarized in detail by Morris and Mandair [78].
(iii) To access the sample volume for PRS and SAM imaging, the sample sur-

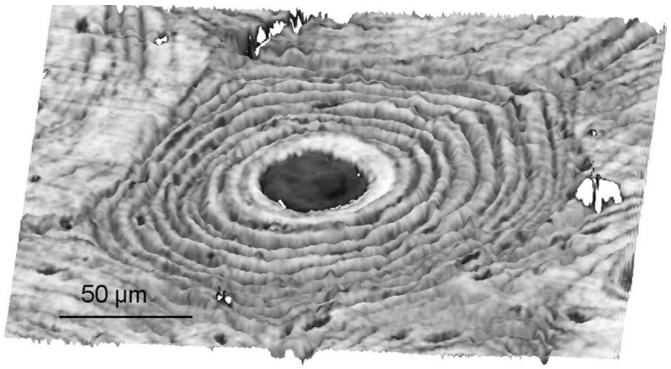

Figure 3.23: Surface topography of a lamellar bone sample created by the mechanical polishing procedure. The image displays a 3D reconstruction of the remaining surface topography of an osteonal tissue domain after polishing. The topography was reconstructed by analyzing the confocal distance in x_3 direction between ultrasound transducer and sample surface using the MLA software (Sec. 2.2.2). It is worth noting that higher acoustic impedance values in the image were well correlated with elevations in the topography map. The topographic differences of the lamellar tissue have a significant impact on the reflectivity of the ultrasound waves and the corresponding acoustic impedance values. Image reprinted from [40] with permission from IEEE.

faces were successively polished off to specific x_3 locations (Fig. 3.13). It is worth noting that the mechanical polishing process consumes softer material components more easily than stiffer ones. Therefore polishing of heterogeneous materials involves imbalanced material removal, creating a surface with a certain level of roughness. The corresponding topographical differences of the surface may have had an effect on the result of SAM measurements. Raum et al. [40] have investigated this effect in closer detail in a SAM-based study. The authors provided proof that the topographical differences (Fig. 3.23) created during polishing were on a comparable scale to the depth of the focus of the ultrasound waves of the used high-frequency SAM. As a result, the reflectivity of acoustic waves, in particular due to oblique incidence reflections, was impaired and acoustic impedance values significantly decreased locally. Accordingly, it can be assumed that the absolute acoustic impedance values reported in this study were most likely considerably reduced due to surface polishing. Though again, this effect equally affects all investigated specimens. Therefore, relative comparison between adjacent lamellae and different tissue domains on the same samples, and also between different samples, seemed legitimate. However, relative maximum and minimum values of the acoustic impedance of individual lamellae might be impaired by the mechanical polishing. An effect of the polishing procedure on PRS-based estimation of the fibril orientation and tissue composition could not be excluded, but was assumed to be unlikely. To avoid any topography-related artefacts in PRS scanning, the laser was focused underneath the sample surface in all measurements.

Lastly, the presented study design was restricted by the differences in spatial resolution of the site-matched imaging modalities. PRS and SAM featured a lateral resolution of approximately 1 µm, whereas SR-nanoCT allowed for imaging at a spatial resolution of ~250 nm. In other words, the probing volumes of PRS and SAM are relatively large in comparison to individual collagen fibrils. Therefore, corresponding parameter maps represent average values of all sublamellae within the probing volume. As demonstrated in Sec. 3.1.3, the result of this resolution-determined averaging is an image blurring effect that might be a limiting factor for one-to-one comparisons to SR-nanoCT data, assessed at a much smaller probing volume.
Ultimately, the planar registration of the different images had a finite accuracy that may have shifted ROIs with respect to each other and weakened the sought parameter correlation.

3.3 Impact of Nf1 Mutation on the Development of Bone Matrix Elasticity

The results of the study presented in this chapter were published as one part of a comprehensive multimodal characterization of Nf1 mutants published by Kühnisch et al. [173]. Several figures and considerations presented in this section were part of that publication.

3.3.1 Neurofibromatosis Type 1

Neurofibromatosis type 1 (NF1) is a common, inherited genetic disorder caused by a functional mutation of the neurofibromin 1 gene (Nf1). Nf1 is a tumor suppressor gene and plays a part in cell division control [174]. During fetal development, Nf1 is expressed in a variety of mesenchymal- and neural crest-derived tissue types. In particular, osteoblasts, osteoclasts, chondrocytes, vascular endothelial cells, and fibroblasts express the Nf1 gene and may be potentially impaired by Nf1 mutation [175].

NF1 has an incidence of 1 per 3000-4000 individuals [174, 176]. NF1 patients are primarily affected by benign tumor development along peripheral and optical nerves (neurofibromas) derived from nerve sheath (Schwann) cells. Additionally, NF1 is associated with a wide range of relatively common non-tumor manifestations. These include diverse skeletal abnormalities, such as short stature, bowing and/or pseudarthrosis of the tibia, osteopenia, osteoporosis, or debilitating focal skeletal dysplasias, amongst others [177–179]. To date, the mechanisms underlying the cellular and molecular pathogenesis of these skeletal defects are still poorly understood, and current therapeutic options are limited [180, 181]. In general, a reduced bone mineral density (BMD) was reported in most NF1 patients [181]. Regarding the skeletal phenotype, poor bone quality and a generalized alteration of the bone tissue, can be suspected.

In order to study the role of Nf1 in skeletal formation with respect to the mechanical properties of the bone matrix, two genetically engineered knock out mouse models characterized by Nf1 inactivation at different stages of the skeletal development were analyzed by means of acoustic microscopy within the frame of this thesis:

- **Nf1**^{Prx1} knock-out mice were characterized by conditional ablation of Nf1 in mesenchymal progenitor cells of developing mouse limbs, leading to efficient Nf1 inactivation in osteoblasts, chondrocytes, endothe-

lial cells, adipocytes, and myocytes. Similar to NF1 affected patients, $Nf1^{Prx1}$ mice displayed diminished long bone growth. and tibial bowing. Moreover, hip joint fusion and delayed bone defect healing were observed [178, 182]. As a potential cause of the defective bone tissue development that also included hypo-mineralization and increased porosity, altered proliferation and differentiation of the osteoblasts were identified in these knock-out mice[178].

- In contrast, $\mathbf{Nf1}^{Col1}$ knock-out mice featured Nf1 ablation at the pre-osteoblast stage. The Nf1 mutation was therefore restricted to bone forming cells. Other mesenchymal cells and their derivatives were not impaired by the mutation. Specifically, the osteoblast organic matrix synthesis and mineralization were affected in these animals [180, 181]. In comparison to $Nf1^{Prx1}$, $Nf1^{Col1}$ mice exhibited a milder phenotype.

3.3.2 Materials and Methods

Sample Preparation

Bone samples were prepared from three-month old mice. $Nf1^{Prx1}$ mutants displayed fused hip joints, therefore hind limb movement was compromised and the animals mainly moved using their fore-limbs. To avoid the measurements of tissue properties, influenced by the absence of mechanical loading, and to assess only the genetic phenotype, analysis focused on mouse humeri.

The entire bone humeri of (i) 4 $Nf1^{Prx1}$ mutants plus 4 corresponding controls and (ii) 4 $Nf1^{Col1}$ mutants plus 5 corresponding wildtypes were investigated. Longitudinal sections at the medial level, displaying a complete and open bone marrow cavity and separated anterior and posterior cortex were prepared. Next, plane and smooth sample surfaces were prepared by means of a grinding procedure using silicon carbide abrasive papers (grit size 4000; Phoenix 4000, Buehler, Düsseldorf, Germany). Subsequently, sample surfaces were polished with a hard synthetic cloth, ethyleneglycol suspension, and 1 µm diamond particles as an abrasive.

Scanning Acoustic Microscopy

The entire mice humeri were measured by means of a custom-developed scanning acoustic microscope (SAM200Ex, Q-BAM, Halle, Germany) employing a spherically focused ultrasound transducer exhibiting a nominal center frequency of 200 MHz (FHI 200/60°: Frauenhofer Institut für Biomedizinische Technik, St. Ingbert, Germany) as described by Raum et al. [183]. The experimental setup achieved a lateral resolution of approximately 8 µm. The specimens were placed in a tank filled with distilled and degassed water,

temperature controlled at 26±0.3°C. For acoustic measurements, the specimen surface was aligned perpendicular to the focal plane of the transducer. For specimen mapping, the transducer was stepwise translated in the x_1x_2 plane with a scan increment of 4 µm. At every scan position, the acoustic pulse echo signal $V_{x_1,x_2}(t)$ was recorded. Subsequently, to allow for focus correction, a line scan in x_1 direction was conducted on every sample at decreasing transducer-sample distances in x_3 direction within the same bone area. The microscope was calibrated using homogeneous reference samples (polymethylmethacrylate, titanium). Based on these calibration measurements, the confocal reflection amplitude measured at every scan position was converted into values of the reflection coefficient R and consequently into acoustic impedance values Z as described by Lakshmanan et al. [168].

Statistics

Multiple factor ANOVA was applied to compare the mean acoustic impedance values of different ROIs on the anterior and posterior sides and towards proximal and distal ends of the mouse humerus. Statistical results were considered significant for p-values less than 0.05.

3.3.3 Results and Discussion

To investigate the elastic properties of the $Nf1^{Prx1}$ and $Nf1^{Col1}$ mutants in comparison to their wildtypes, SAM measurements with a frequency of 200 MHz were performed and the entire mouse humeri were scanned. Thus, the elastic properties of mutants and controls could be compared. Fig. 3.24 shows the acoustic impedance maps of the humeri at three months of age of a representative pair of $Nf1^{Prx1}$ mutant and control animal. Clearly, an altered shape of the $Nf1^{Prx1}$ humerus can be observed in comparison to the control. The $Nf1^{Prx1}$ mutants displayed bowing of the humerus, whereas the control animals had a straight shape. Moreover, $Nf1^{Prx1}$ humeri were considerably smaller than corresponding controls. These observations are in line with earlier findings of Kolancyk et al. [178, 182].

Corresponding analysis was performed on $Nf1^{Col1}$ mice, characterized by Nf1 ablation in osteoblasts, and their wildtypes. Fig. 3.25 depicts the acoustic impedance maps of the humeri of a representative pair of $Nf1^{Col1}$ mutant and wildtype. The humeri of both genotypes featured similar size and shape.

To study the distribution and heterogeneity of acoustic impedance values, various ROIs on the humerus cortex were selected and differences between Nf1 mutants and control animals were analyzed. As indicated in Figs. 3.24b and Figs. 3.25b, these ROIs were located on the anterior (A) and posterior (P) sides of the cortex, at the proximal end of the humerus (E1), in the vicinity of

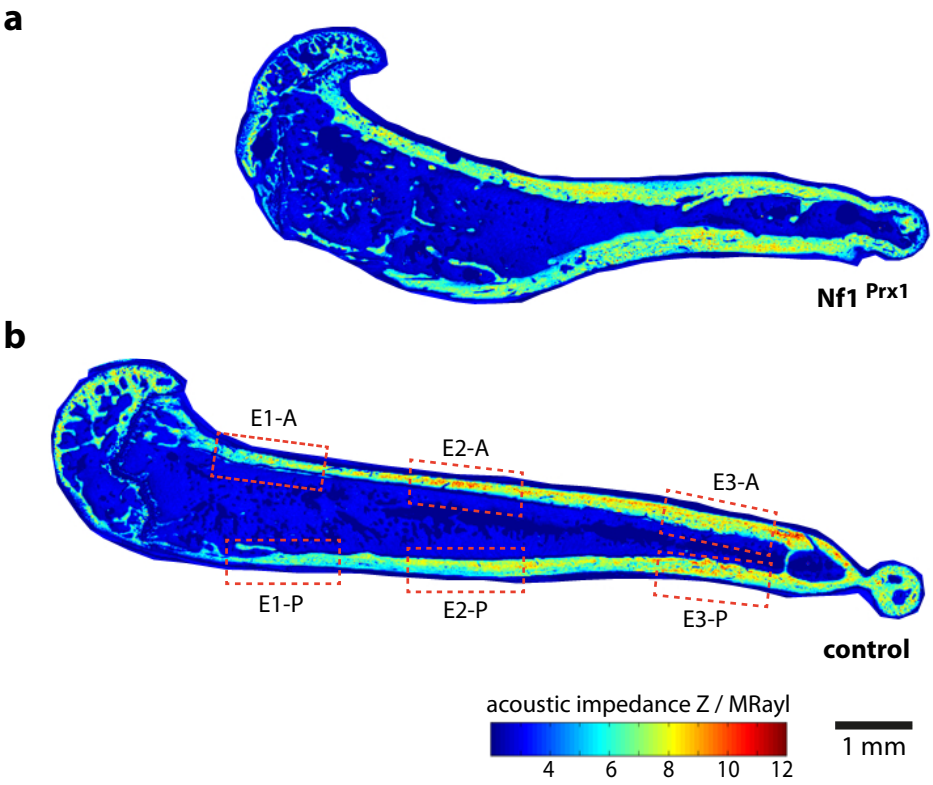

Figure 3.24: Acoustic impedance maps of an entire Nf1^{Prx1} humerus and a corresponding control. Nf1^{Prx1} mutants (a) were clearly smaller, displayed bowing, and exhibited diminished acoustic impedance values in comparison with the control displayed in panel (b). As indicated with the red rectangles in (b), six ROIs (E1A–E3P) on the anterior and posterior bone cortex of Nf1-Prx-Cre and controls were compared for further analysis.

the shoulder, in the midshaft region (E2), and at the distal end of the humerus (E3), next to the elbow. Quantitative comparison of the mean values of all ROIs revealed a significant reduction ($p \leq 0.001$) in acoustic impedance values of Nf1^{Prx1} in comparison with controls (Fig. 3.26a). On average, Nf1^{Prx1} mice and corresponding controls exhibited mean values $Z_{Nf1^{Prx1}} = 5.96 \pm 0.70$ MRayl and $Z_{controls} = 6.83 \pm 0.59$. Moreover, Nf1^{Prx1} mutants exhibited reduced impedance values in ROIs E2 and E3 (Fig. 3.27a) in comparison to controls, indicating a softening of the mineralized organic matrix in the midshaft and distal end of the humerus. Anterior and posterior cortex of Nf1^{Prx1} mice exhibited both significantly smaller impedance values than corresponding sides on control humeri, though the difference was more pronounced on the posterior side of the humerus cortex (Fig. 3.27b). A more detailed statistical analysis is summarized in Table 3.4.

In contrast, no significant difference between Nf1^{Col1} mice humeri and corresponding wildtype bones could be detected. Mean acoustic impedance values of $Z_{Nf1^{Col1}} = 5.90 \pm 0.73$ MRayl and $Z_{wildtype} = 5.92 \pm 0.69$ were ob-

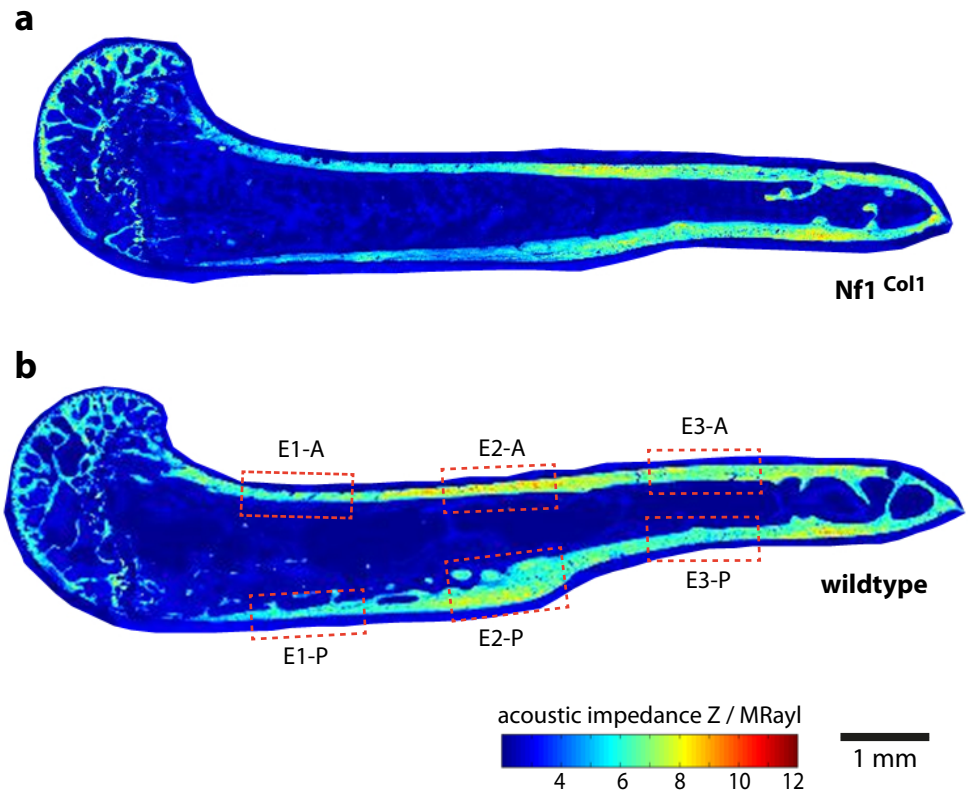

Figure 3.25: Mean acoustic impedance maps of an entire Nf1^{Col1} humerus and a corresponding wildtype. The Nf1^{Col1} genotype (a) exhibited similar acoustic impedance values to the wildytpe displayed in panel (b). As indicated with the red rectangles in (b), six ROIs E1A–E3P on the anterior and posterior bone cortex of Nf1^{Col1} and controls were compared for further analysis.

tained (Fig. 3.26b). No differences between the ROIs E1-E3 or anterior and posterior sides of Nf1^{Col1} mice with respect to corresponding wildtypes were found. The results of the statistical analysis are listed in Table 3.5

In conclusion, the analysis provided clear proof that loss of neurofibromin 1 in mesenchymal progenitor cells of the developing limbs of Nf1^{Prx1} knock-out mice induced impairment of the bone matrix stiffness of the limbs of adult mice. The impact of the mutation was found to be most pronounced in the bowed part of Nf1^{Prx1} humeri. In particular, specific ROIs on the humerus cortex, i.e. on the posterior side, in the midshaft region, and towards the distal end of the humerus, exhibit a significant reduction of acoustic impedance values and consequently of stiffness values. Interestingly, Nf1^{Col1} humeri do not display significant reduction in acoustic impedance values in comparison with corresponding wildtypes. Since Nf1^{Col1} are characterized by Nf1 inactivation in pre-osteoblasts but not in other cells of the musculoskeletal system, the normal elastic properties measured in Nf1^{Col1} mice suggested that only

disturbance of early osteoblast progenitor cell differentiation critically determined bone strength.

There are various physical and biological aspects that should be considered as potential determinants of Nf1^{Prx1} mutant matrix stiffness loss. As stated in the previous subsections, bone mass, chemical composition and in particular degree of mineralization, fibrillar architecture, and porosity are physical properties that crucially influence bone matrix stiffness.
Earlier studies demonstrated that the activities of osteoblast and osteoclasts are imbalanced upon early functional inactivation of Nf1. As a result, high turnover of the bone matrix, reduced bone mass, and low mineral content were observed in Nf1 mutants [180, 182, 184, 185]. Furthermore, Kühnisch and co-authors [173] also found alterations in the collagen matrix organization of Nf1^{Prx1} mutants. In specific regions in proximity to blood vessels traversing through the cortex, collagen with reduced thickness and packing was observed. Though it is worth noting that the overall mineral orientation measured by means of SAXS was found to be unaffected in Nf1^{Prx1} mutants [173]. Hence it can be assumed that collagen orientation was not disturbed. Finally, the authors of the study demonstrated that Nf1^{Prx1} mutants exhibited increased micro-porosity in cortical bone, associated with increased osteocyte lacunae size with respect to corresponding controls [173].

In summary, the defective collagen matrix formation, low mineralization, and increased microporosity outlined by others represent probable determinants of the diminished stiffness values of Nf1^{Prx1} mutants observed in the presented study. Currently, estimation of the most dominant factor, affecting the matrix stiffness, remains speculative. In general, in combination with the decreased stiffness values observed in this thesis, the physical and biological factors, outlined by Kühnisch et al. [173] indicated that neurofibromin 1 mutation in an early development stage of murine long bones induced a generalized and fundamental defect in bone tissue function.

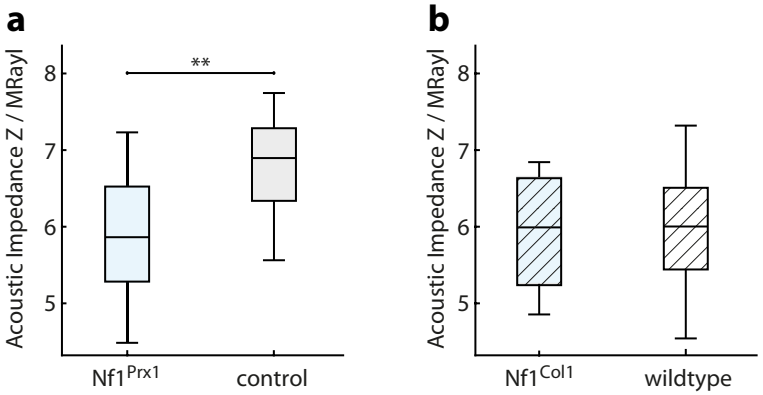

Figure 3.26: Genotype-specific boxplot analysis of acoustic impedance values of Nf1 mutants and corresponding controls for all ROIs. (a) Nf1^{Prx1} humeri exhibited diminished impedance values in comparison to corresponding controls. (b) No statistically significant difference was found between Nf1^{Col1} and corresponding wildtypes.

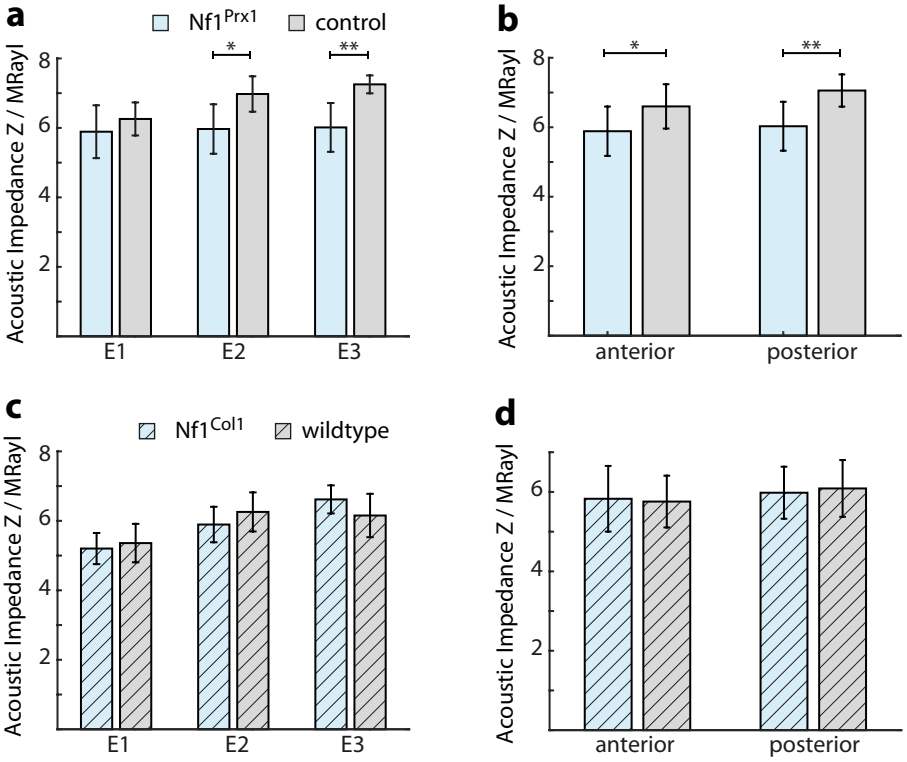

Figure 3.27: Genotype-specific analysis of acoustic impedance values of Nf1 mutants and corresponding controls with respect to the anatomical location. Comparison of the individual ROIs E1-E3 with respect to proximal and distal ends (a), (c) and anterior and posterior cortex side (b), (c) of Nf1^{Prx1} and Nf1^{Col1} humeri in comparison to their corresponding controls, respectively.

Table 3.4: Acoustic impedance measurement of Nf1^{Prx1} and control mice humeri measured by ultrasound microscopy. Statistical analysis showed that acoustic impedance values were significantly affected by the mouse genotype. Statistical significance calculated by multiple factor ANOVA of Nf1^{Prx1} mice vs. controls.

	Nf1-Prx1 / MRayl	control / MRayl	ANOVA
E1+E2+E3	5.96 ± 0.70	6.83 ± 0.59	p ≤ 0.001 (F=21.8)
Anterior	5.89 ± 0.71	6.60 ± 0.64	p ≤ 0.05 (F=6.7)
Posterior	6.03 ± 0.70	7.06 ± 0.46	p ≤ 0.001 (F=17.9)
E1	5.89 ± 0.76	6.26 ± 0.48	n.s.
E2	5.97 ± 0.71	6.98 ± 0.51	p ≤ 0.01 (F=10.6)
E3	6.18 ± 0.57	7.25 ± 0.26	p ≤ 0.001 (F=21.9)
E1 - A	5.70 ± 0.82	5.92 ± 0.33	n.s.
E2 - A	5.89 ± 0.83	6.69 ± 0.45	n.s.
E3 - A	6.06 ± 0.63	7.19 ± 0.30	p ≤ 0.05 (F=10.5)
E1 - P	6.08 ± 0.76	6.59 ± 0.34	n.s.
E2 - P	6.04 ± 0.70	7.26 ± 0.44	p ≤ 0.05 (F=8.8)
E3 - P	5.97 ± 0.86	7.32 ± 0.23	p ≤ 0.05 (F=9.0)

Table 3.5: Acoustic impedance measurement of Nf1^{Col1} and control mice humeri measured by ultrasound microscopy. Multiple factor ANOVA showed that acoustic impedance was not affected by the genotype, but was significantly lower in region E1 than in regions E2 and E3 (F=18.8). Statistical significance calculated by ANOVA of Nf1^{Col1} vs. control. All values are given as mean ± standard deviation.

	Nf1-Col1 / MRayl	control / MRayl	ANOVA
E1+E2+E3	5.90 ± 0.73	5.92 ± 0.69	n.s.
Anterior	5.83 ± 0.83	5.76 ± 0.65	n.s.
Posterior	5.98 ± 0.66	6.09 ± 0.72	n.s.
E1	5.20 ± 0.45	5.36 ± 0.55	n.s.
E2	5.89 ± 0.51	6.26 ± 0.56	n.s.
E3	6.62 ± 0.40	6.15 ± 0.62	n.s.
E1 - A	5.09 ± 0.51	5.19 ± 0.50	n.s.
E2 - A	5.80 ± 0.67	6.06 ± 0.46	n.s.
E3 - A	6.60 ± 0.53	6.02 ± 0.65	n.s.
E1 - P	5.31 ± 0.42	5.53 ± 0.61	n.s.
E2 - P	5.99 ± 0.36	6.45 ± 0.63	n.s.
E3 - P	6.64 ± 0.31	6.28 ± 0.65	n.s.

4

Conclusion

The objective of this thesis was the concurrent assessment of compositional, structural, and mechanical bone properties on the micron length scale with the aim of shedding light on the intricate link between these tissue characteristics. This objective and additional research questions were addressed using novel experimental approaches.

The aim of the first experimental study (Sec. 3.1) was to demonstrate the potential of PRS in deciphering the 3D structure of collagen fibrils in lamellar bone. By analyzing the anisotropic response of the amide I Raman signal as a function of the incident laser polarization, evidence about the correlation of the anisotropic amide I Raman scattering and the orientation of collagen fibrils in bone lamellae was provided. Specifically, the study revealed that the degree of anisotropy of the amide I signal reflected the directionality of the collagen fibrils in the lamellar plane. Hence, in combination with the results of earlier studies [35, 36], orientation information in 3D could be derived from Raman spectra. Across osteonal bone lamellae, a gradual change of the amide I Raman response from isotropic to highly anisotropic was observed. This signal transformation was attributed to lamellar fibril arrangements with continuously changing twist angles φ, gradually rotating in the lamellar plane.
The major drawback of the structural PRS analysis was its inability to precisely quantify the twist angle φ of the collagen fibrils at a specific point within the lamella. Interestingly, apparent tilts of the collagen fibrils out of the lamellar plane were observed. By supporting the experimental data with theoretical models, these tilts eventually enabled identification of specific lamellar organization patterns. Finally, twisted and oscillating plywood patterns could be distinguished. Both patterns were found to coexist in the same osteon, corroborating earlier findings [13]. In addition, spectral analysis provided evidence of decreased anisotropy levels in osteonal lamellae compared to theoretical predictions [36] and experimental data on RTT [35]. By means of computational simulations, this anisotropy loss was associated with (i) the averaging of sublamellar twist angles as a result of the limited spatial resolution of the PRS microscope and (ii) the potential presence of disordered collagen fibrils within the lamellar organization reported in earlier studies [20, 63].

Subsequently (Sec. 3.2), the analytical PRS approach was extended by combining it for the first time with SR-μCT, SR-nanoCT, and SAM experiments in a site-matched manner. By means of these high-resolution and non-destructive methods, complementary and spatially site-matched data of mass density, fibrillar orientation, composition of mineral and collagen phase, mineral maturity, and acoustic impedance were provided at two structural levels of bone hierarchy, i.e entire tissue domains and single lamellae.
Compositional parameters, measures of mineral maturity, and elastic properties were found to be determined by the local tissue age, confirming earlier findings [44, 67–69, 127]. These parameters were independent of lamellar modulations and exhibited relative homogeneous distributions across bone lamellae. In contrast, fibril orientation and elastic tissue properties exhibited periodic oscillations and cross-correlation revealed a strong positive correlation between local orientation and elastic properties. Based on the spatial data analysis, the twisting fibril orientation was identified as the major determinant of the undulating elastic properties at the lamellar level, rather than compositional variations, modulations of the mineral particle maturity, or mass density deviations.
Additionally, histogram-related kernel density estimation analysis of PRS data of entire tissue domains indicated predominant fibril orientations in bone structural units which could be associated with the coexistence of oscillating and twisted plywood patterns within the same structural units. Corresponding analysis of the resulting micromechanical properties directly reflected on these principal fibril orientations. In conclusion, the presented multiscalar analysis highlights the dominant impact of the fibrillar architecture on the local micromechanical competence of lamellar bone.

Finally, regarding the information on fibril orientation, a good agreement between the applied methodologies was observed. Even though PRS did not allow for quantitative determination of the fibril inclination, the results of the site-matched SR-nanoCT and PRS analyses were clearly consistent. Method comparison demonstrated that discrimination between different organization patterns was feasible using PRS. Finally, important tissue characteristics including the predominant fibril orientations in vast tissue areas were easily accessible by means of PRS, overcoming the small field of view and highly limited access to synchrotron sources. In future, the presented results on healthy bone specimens may serve as a reference for investigations of various pathologic bone conditions.

Besides the investigations into healthy bone tissue, the last experimental approach of this thesis was dedicated to the investigation of the genetically caused bone disorder NF1 (Sec. 3.3). To elucidate the role of the Nf1 gene

mutation in the impairment of the mechanical competence of long bones, a quantitative SAM study was conducted. Two genetically engineered knock-out mouse models were analyzed, characterized by Nf1 inactivation at different stages of the skeletal development. It could be demonstrated that only early stage mutation, affecting all mesenchymal pregenitor cells, impaired the development of long bone matrix stiffness critically.

4.1 Outlook

In this thesis the versatility of the analytical PRS approach to obtain 3D structural information of collagen fibrils in a highly complex biological tissue, and to concurrently map chemical information associated with collagen or mineral phase was proven (Sec. 3.1). Furthermore, it was demonstrated that PRS analysis can not only be applied to investigate the microarchitecture of single lamellae, but can also be used for rapid estimation of predominant fibril orientations in vast tissue areas. As PRS allows for the analysis of full mineralized and hydrated tissues in a close to native state, the presented PRS analysis opens up promising new perspectives for the complementary description of a wide range of collagen-based biological tissues. In future studies, the PRS approach may be further extended to detailed analysis of other orientation-sensitive Raman peaks, such as the phosphate associated ν_1 PO_4^{-3} Raman band, enabling combined collagen and mineral orientation analysis and concurrent structure-compositional analysis of biomaterials materials like tooth.

The introduced multimodal approach (Sec. 3.2) presented various fundamental tissue parameter correlations on two levels of bone structural hierarchy. Furthermore, information on coexisting fibril organization patterns, resulting predominant fibril orientations and correlated microelastic properties were provided. These findings may serve as valuable input for computational hierarchical modeling of bone's mechanical performance.
In future studies on bone, the technical multimodal approach can be applied to analyze if the presented parameter correlations vary regarding: (i) aging processes, loading mode and magnitude or anatomical location of healthy bone tissue and (ii) bone pathologies.

Ultimately, the combined PRS and SAM approach is not ony qualified for characterization of a broad range of other structured biological materials, but might also be a suitable imaging tool for the development of new synthetic fiber composite materials.

4

Bibliography

[1] S. C. Cowin: Bone Mechanics Handbook, Second Edition *CRC Press* (2001). Cited on page 1

[2] J. D. Currey: Bones: Structure and Mechanics *Princeton University Press* (2002). Cited on pages 1 and 12

[3] P. Fratzl and R. Weinkamer: Nature's hierarchical materials *Progress in Materials Science* **52** 1263–1334 (2007). Cited on pages 1 and 12

[4] S. Weiner, W. Traub and H. D. Wagner: Lamellar bone: structure-function relations *Journal of structural biology* **126** 241–255 (1999). Cited on pages 2, 12 and 88

[5] J.-Y. Rho, L. Kuhn-Spearing and P. Zioupos: Mechanical properties and the hierarchical structure of bone *Medical Engineering & Physics* **20** 92–102 (1998). Cited on pages 2, 8 and 10

[6] J. Seto, H. S. Gupta, P. Zaslansky, H. D. Wagner and P. Fratzl: Tough Lessons From Bone: Extreme Mechanical Anisotropy at the Mesoscale *Advanced Functional Materials* **18** 1905–1911 (2008).

[7] T. Hofmann, F. Heyroth, H. Meinhard, W. Fränzel and K. Raum: Assessment of composition and anisotropic elastic properties of secondary osteon lamellae *Journal of Biomechanics* **39** 2282–2294 (2006). Cited on pages 3, 16, 26, 28 and 86

[8] M. Granke, A. Gourrier, F. Rupin, K. Raum, F. Peyrin, M. Burghammer, A. Saïed and P. Laugier: Microfibril Orientation Dominates the Microelastic Properties of Human Bone Tissue at the Lamellar Length Scale *PLoS One* **8** e58043 (2013). Cited on pages 2, 3, 16, 28, 46 and 86

[9] H. Wagner and S. Weiner: On the relationship between the microstructure of bone and its mechanical stiffness *Journal of Biomechanics* **25** 1311–1320 (1992). Cited on page 2

[10] A. G. Reisinger, D. H. Pahr and P. K. Zysset: Principal stiffness orientation and degree of anisotropy of human osteons based on nanoindentation in three distinct planes *Journal of the Mechanical Behavior of Biomedical Materials* **4** 2113–2127 (2011). Cited on pages 16 and 28

[11] D. Rohrbach, S. Lakshmanan, F. Peyrin, M. Langer, A. Gerisch, Q. Grimal, P. Laugier and K. Raum: Spatial distribution of tissue level properties in a human femoral cortical bone *Journal of Biomechanics* **45** 2264–2270 (2012).

[12] K. J. Koester, J. W. Ager and R. O. Ritchie: The true toughness of human cortical bone measured with realistically short cracks *Nature Materials* **7** 672–677 (2008).

[13] P. Varga, A. Pacureanu, M. Langer, H. Suhonen, B. Hesse, Q. Grimal, P. Cloetens, K. Raum and F. Peyrin: Investigation of the three-dimensional orientation of mineralized collagen fibrils in human lamellar bone using synchrotron X-ray phase nano-tomography *Acta Biomaterialia* **9** 8118–8127 (2013). Cited on pages 2, 3, 8, 11, 12, 15, 42, 43, 44, 45, 49, 56, 59, 60, 67, 68, 74, 89 and 101

[14] A. Ascenzi and E. Bonucci: The compressive properties of single osteons *The Anatomical Record* **161** 377–391 (1968). Cited on pages 2, 11 and 45

[15] M.-M. Giraud-Guille, L. Besseau and R. Martin: Liquid crystalline assemblies of collagen in bone and in vitro systems *Journal of Biomechanics* **36** 1571–1579 (2003). Cited on pages 2, 45, 55 and 56

[16] M. M. Giraud-Guille: Twisted plywood architecture of collagen fibrils in human compact bone osteons *Calcified tissue international* **42** 167–180 (1988). Cited on pages 2, 11, 15, 43, 45, 49, 55 and 56

[17] G. Marotti: A new theory of bone lamellation *Calcified Tissue International* **53** S47–55; discussion S56 (1993). Cited on pages 11 and 14

[18] S. Weiner, T. Arad and W. Traub: Crystal organization in rat bone lamellae *FEBS letters* **285** 49–54 (1991). Cited on page 14

[19] S. Weiner, T. Arad, I. Sabanay and W. Traub: Rotated plywood structure of primary lamellar bone in the rat: orientations of the collagen fibril arrays *Bone* **20** 509–514 (1997). Cited on pages 7, 12, 15 and 45

[20] N. Reznikov, R. Almany-Magal, R. Shahar and S. Weiner: Three-dimensional imaging of collagen fibril organization in rat circumferential lamellar bone using a dual beam electron microscope reveals ordered and disordered sub-lamellar structures *Bone* **52** 676–683 (2013). Cited on pages 12, 15, 45, 56, 60 and 101

[21] N. Reznikov, R. Shahar and S. Weiner: Bone hierarchical structure in three dimensions *Acta Biomaterialia* **10** 3815–3826 (2014). Cited on pages 2, 8, 12, 44 and 45

[22] W. Wagermaier, H. S. Gupta, A. Gourrier, M. Burghammer, P. Roschger and P. Fratzl: Spiral twisting of fiber orientation inside bone lamellae *Biointerphases* **1** 1 (2006). Cited on pages 2, 12, 15 and 45

[23] A. Boskey and R. Mendelsohn: Infrared analysis of bone in health and disease *Journal of Biomedical Optics* **10** 031102–0311029 (2005). Cited on pages 2, 23 and 24

[24] M. Kazanci, P. Roschger, E. P. Paschalis, K. Klaushofer and P. Fratzl: Bone osteonal tissues by Raman spectral mapping: orientation-composition *Journal of structural biology* **156** 489–496 (2006). Cited on pages 3, 14, 23, 24, 25, 26 and 50

[25] A. Roschger, S. Gamsjaeger, B. Hofstetter, A. Masic, S. Blouin, P. Messmer, A. Berzlanovich, E. P. Paschalis, P. Roschger, K. Klaushofer and P. Fratzl: Relationship between the v2po4/amide III ratio assessed by Raman spectroscopy and the calcium content measured by quantitative backscattered electron microscopy in healthy human osteonal bone *Journal of Biomedical Optics* **19** 065002–065002 (2014). Cited on pages 2, 14 and 23

[26] A. Carden and M. D. Morris: Application of vibrational spectroscopy to the study of mineralized tissues (review) *Journal of Biomedical Optics* **5** 259–268 (2000). Cited on pages 2 and 23

[27] O. Akkus, A. Polyakova-Akkus, F. Adar and M. B. Schaffler: Aging of microstructural compartments in human compact bone *Journal of Bone and Mineral Research* **18** 1012–1019 (2003). Cited on pages 2, 23 and 24

[28] A. Bonifacio and V. Sergo: Effects of sample orientation in Raman microspectroscopy of collagen fibers and their impact on the interpretation of the amide III band *Vibrational Spectroscopy* **53** 314–317 (2010). Cited on page 3

[29] M. Janko, P. Davydovskaya, M. Bauer, A. Zink and R. W. Stark: Anisotropic Raman scattering in collagen bundles *Optics Letters* **35** 2765–2767 (2010). Cited on pages 3 and 26

[30] S. Gamsjaeger, A. Masic, P. Roschger, M. Kazanci, J. W. C. Dunlop, K. Klaushofer, E. P. Paschalis and P. Fratzl: Cortical bone composition and orientation as a function of animal and tissue age in mice by Raman spectroscopy *Bone* **47** 392–399 (2010). Cited on pages 3, 24 and 26

[31] G. Falgayrac, S. Facq, G. Leroy, B. Cortet and G. Penel: New method for Raman investigation of the orientation of collagen fibrils and crystallites in the Haversian system of bone *Applied spectroscopy* **64** 775–780 (2010). Cited on page 26

[32] M. Raghavan, N. D. Sahar, R. H. Wilson, M.-A. Mycek, N. Pleshko, D. H. Kohn and M. D. Morris: Quantitative polarized Raman spectroscopy in highly turbid bone tissue *Journal of Biomedical Optics* **15** 037001–037001–7 (2010).

[33] D. Carnelli, P. Vena, M. Dao, C. Ortiz and R. Contro: Orientation and size-dependent mechanical modulation within individual secondary osteons in cortical bone tissue *Journal of The Royal Society Interface* **10** 20120953 (2013).

[34] A. J. Makowski, C. A. Patil, A. Mahadevan-Jansen and J. S. Nyman: Polarization control of Raman spectroscopy optimizes the assessment of bone tissue *Journal of biomedical optics* **18** 55005 (2013). Cited on pages 3 and 24

[35] A. Masic, L. Bertinetti, R. Schuetz, L. Galvis, N. Timofeeva, J. W. C. Dunlop, J. Seto, M. A. Hartmann and P. Fratzl: Observations of multiscale, stress-induced changes of collagen orientation in tendon by polarized Raman spectroscopy *Biomacromolecules* **12** 3989–3996 (2011). Cited on pages 3, 26, 48, 50, 55, 58, 59 and 101

[36] L. Galvis, J. W. C. Dunlop, G. Duda, P. Fratzl and A. Masic: Polarized Raman Anisotropic Response of Collagen in Tendon: Towards 3d Orientation Mapping of Collagen in Tissues *PLoS One* **8** e63518 (2013). Cited on pages 3, 14, 25, 50, 51, 52, 53, 58, 59, 73, 83 and 101

[37] S. Hengsberger, A. Kulik and P. Zysset: Nanoindentation discriminates the elastic properties of individual human bone lamellae under dry and physiological conditions *Bone* **30** 178–184 (2002). Cited on pages 3 and 16

[38] J. Xu, J. Y. Rho, S. R. Mishra and Z. Fan: Atomic force microscopy and nanoindentation characterization of human lamellar bone prepared by microtome sectioning and mechanical polishing technique *Journal of biomedical materials research. Part A* **67** 719–726 (2003).

[39] H. Gupta, U. Stachewicz, W. Wagermaier, P. Roschger, H. Wagner and P. Fratzl: Mechanical modulation at the lamellar level in osteonal bone *Journal of Materials Research* **21** 1913–1921 (2006). Cited on pages 3, 14, 16, 28, 77 and 83

[40] K. Raum, K. Jenderka, A. Klemenz and J. Brandt: Multilayer analysis: quantitative scanning acoustic microscopy for tissue characterization at a microscopic scale *IEEE Transactions on Ultrasonics, Ferroelectrics, and Frequency Control* **50** 507–516 (2003). Cited on pages 3, 28, 69, 71 and 90

[41] F. S. Utku, E. Klein, H. Saybasili, C. A. Yucesoy and S. Weiner: Probing the role of water in lamellar bone by dehydration in the environmental scanning electron microscope *Journal of Structural Biology* **162** 361–367 (2008). Cited on pages 3, 14 and 83

[42] M. Kazanci, H. D. Wagner, N. I. Manjubala, H. S. Gupta, E. Paschalis, P. Roschger and P. Fratzl: Raman imaging of two orthogonal planes within cortical bone *Bone* **41** 456–461 (2007). Cited on pages 3, 14 and 78

[43] E. M. Spiesz, A. G. Reisinger, W. Kaminsky, P. Roschger, D. H. Pahr and P. K. Zysset: Computational and experimental methodology for site-matched investigations of the influence of mineral mass fraction and collagen orientation on the axial indentation modulus of lamellar bone *Journal of the Mechanical Behavior of Biomedical Materials* **28** 195–205 (2013). Cited on page 3

[44] J. Y. Rho, T. Y. Tsui and G. M. Pharr: Elastic properties of human cortical and trabecular lamellar bone measured by nanoindentation *Biomaterials* **18** 1325–1330 (1997). Cited on pages 7, 74 and 102

[45] S. Weiner and H. D. Wagner: The Material Bone: Structure-Mechanical Function Relations *Annual Review of Materials Science* **28** 271–298 (1998). Cited on page 8

[46] J. D. Currey: The design of mineralised hard tissues for their mechanical functions *Journal of Experimental Biology* **202** 3285–3294 (1999).

[47] J. S. Nyman, M. Reyes and X. Wang: Effect of ultrastructural changes on the toughness of bone *Micron* **36** 566–582 (2005). Cited on page 7

[48] E. Davies, K. H. Müller, W. C. Wong, C. J. Pickard, D. G. Reid, J. N. Skepper and M. J. Duer: Citrate bridges between mineral platelets in bone *Proceedings of the National Academy of Sciences of the United States of America* **111** E1354–1363 (2014). Cited on page 7

[49] S. R. Stock: The Mineral-Collagen Interface in Bone *Calcified Tissue International* **97** 262–280 (2015). Cited on page 7

[50] S. J. Eppell, W. Tong, J. Lawrence Katz, L. Kuhn and M. J. Glimcher: Shape and size of isolated bone mineralites measured using atomic force microscopy *Journal of Orthopaedic Research* **19** 1027–1034 (2001). Cited on page 7

[51] P. Fratzl, H. S. Gupta, E. P. Paschalis and P. Roschger: Structure and mechanical quality of the collagen–mineral nano-composite in bone *Journal of Materials Chemistry* **14** 2115–2123 (2004). Cited on pages 8 and 78

[52] M. A. Rubin, I. Jasiuk, J. Taylor, J. Rubin, T. Ganey and R. P. Apkarian: TEM analysis of the nanostructure of normal and osteoporotic human trabecular bone *Bone* **33** 270–282 (2003). Cited on page 7

[53] W. J. Landis, K. J. Hodgens, J. Arena, M. J. Song and B. F. McEwen: Structural relations between collagen and mineral in bone as determined by high voltage electron microscopic tomography *Microscopy research and technique* **33** 192–202 (1996). Cited on page 7

[54] W. J. Landis and F. H. Silver: The structure and function of normally mineralizing avian tendons *Comparative Biochemistry and Physiology. Part A, Molecular & Integrative Physiology* **133** 1135–1157 (2002). Cited on page 7

[55] Y. Bala and E. Seeman: Bone's Material Constituents and their Contribution to Bone Strength in Health, Disease, and Treatment *Calcified Tissue International* **97** 308–326 (2015). Cited on page 7

[56] B. Depalle, Z. Qin, S. J. Shefelbine and M. J. Buehler: Influence of cross-link structure, density and mechanical properties in the mesoscale deformation mechanisms of collagen fibrils *Journal of the Mechanical Behavior of Biomedical Materials* **52** 1–13 (2015). Cited on page 7

[57] L. E. Bertassoni, J. P. R. Orgel, O. Antipova and M. V. Swain: The dentin organic matrix - limitations of restorative dentistry hidden on the nanometer scale *Acta Biomaterialia* **8** 2419–2433 (2012). Cited on page 7

[58] A. L. Arsenault: Image analysis of collagen-associated mineral distribution in cryogenically prepared turkey leg tendons *Calcified Tissue International* **48** 56–62 (1991). Cited on page 8

[59] N. Sasaki, A. Tagami, T. Goto, M. Taniguchi, M. Nakata and K. Hikichi: Atomic force microscopic studies on the structure of bovine femoral cortical bone at the collagen fibril-mineral level *Journal of Materials Science: Materials in Medicine* **13** 333–337 (2002). Cited on pages 8 and 16

[60] W. Zhang, S. S. Liao and F. Z. Cui: Hierarchical Self-Assembly of Nano-Fibrils in Mineralized Collagen *Chemistry of Materials* **15** 3221–3226 (2003). Cited on page 8

[61] P. Fratzl, N. Fratzl-Zelman, K. Klaushofer, G. Vogl and K. Koller: Nucleation and growth of mineral crystals in bone studied by small-angle X-ray scattering *Calcified Tissue International* **48** 407–413 (1991). Cited on page 8

[62] W. J. Landis, M. J. Song, A. Leith, L. McEwen and B. F. McEwen: Mineral and organic matrix interaction in normally calcifying tendon visualized in three dimensions by high-voltage electron microscopic tomography and graphic image reconstruction *Journal of Structural Biology* **110** 39–54 (1993). Cited on page 8

[63] N. Reznikov, R. Shahar and S. Weiner: Three-dimensional structure of human lamellar bone: The presence of two different materials and new insights into the hierarchical organization *Bone* **59** 93–104 (2014). Cited on pages 8, 11, 12, 15, 44, 56, 60 and 101

[64] R. R. Cooper, J. W. Milgram and R. A. Robinson: Morphology of the osteon. An electron microscopic study *The Journal of Bone and Joint Surgery. American Volume* **48** 1239–1271 (1966). Cited on page 10

[65] L. F. Bonewald: The amazing osteocyte *Journal of Bone and Mineral Research* **26** 229–238 (2011). Cited on page 10

[66] J. Klein-Nulend, A. D. Bakker, R. G. Bacabac, A. Vatsa and S. Weinbaum: Mechanosensation and transduction in osteocytes *Bone* **54** 182–190 (2013). Cited on page 10

[67] K. Raum, I. Leguerney, F. Chandelier, M. Talmant, A. Saïed, F. Peyrin and P. Laugier: Site-matched assessment of structural and tissue properties of cortical bone using scanning acoustic microscopy and synchrotron radiation μCT *Physics in Medicine and Biology* **51** 733 (2006). Cited on pages 10, 28, 35, 74, 77 and 102

[68] A. Boskey and N. P. Camacho: FT-IR Imaging of Native and Tissue-Engineered Bone and Cartilage *Biomaterials* **28** 2465 (2007). Cited on pages 77 and 78

[69] S. Gourion-Arsiquaud, J. C. Burket, L. M. Havill, E. DiCarlo, S. B. Doty, R. Mendelsohn, M. C. H. v. d. Meulen and A. L. Boskey: Spatial Variation in Osteonal Bone Properties Relative to Tissue and Animal Age *Journal of Bone and Mineral Research* **24** 1271 (2009). Cited on pages 10, 77, 78 and 102

[70] W. Gebhardt: Über funktionell wichtige anordnungweisen der feineren und grösseren bauelemente des wirbeltierknoches. ii spezieller teil. i. der bau der haversschen lamellensysteme und seine funktionelle bedeutung *Archiv für Entwicklungsmechanik der Organismen* 187 – 322 (1906). Cited on pages 11 and 14

[71] A. Ascenzi and E. Bonucci: The tensile properties of single osteons *The Anatomical Record* **158** 375–386 (1967). Cited on page 11

[72] M. A. Meyers, P.-Y. Chen, A. Y.-M. Lin and Y. Seki: Biological materials: Structure and mechanical properties *Progress in Materials Science* **53** 1–206 (2008). Cited on page 12

[73] E. B. Ruth: Bone studies; fibrillar structure of adult human bone *The American Journal of Anatomy* **80** 35–53 (1947). Cited on page 14

[74] A. Ascenzi and E. Bonucci: A quantitative investigation of the birefringence of the osteon *Acta Anatomica* **44** 236–262 (1961). Cited on page 14

[75] E. M. Spiesz, W. Kaminsky and P. K. Zysset: A quantitative collagen fibers orientation assessment using birefringence measurements: Calibration and application to human osteons *Journal of Structural Biology* **176** 302–306 (2011). Cited on pages 14 and 86

[76] M. G. Ascenzi, A. Ascenzi, A. Benvenuti, M. Burghammer, S. Panzavolta and A. Bigi: Structural differences between "dark" and "bright" isolated human osteonic lamellae *Journal of structural biology* **141** 22–33 (2003). Cited on pages 14 and 45

[77] M.-G. Ascenzi and A. Lomovtsev: Collagen orientation patterns in human secondary osteons, quantified in the radial direction by confocal microscopy *Journal of structural biology* **153** 14–30 (2006). Cited on pages 14 and 45

[78] M. D. Morris and G. S. Mandair: Raman Assessment of Bone Quality *Clinical Orthopaedics and Related Research* **469** 2160–2169 (2010). Cited on pages 13, 14, 18, 21, 23, 24, 78 and 89

[79] G. S. Mandair and M. D. Morris: Contributions of Raman spectroscopy to the understanding of bone strength *BoneKEy Reports* **4** 620 (2015). Cited on page 14

[80] E. P. Paschalis, E. DiCarlo, F. Betts, P. Sherman, R. Mendelsohn and A. L. Boskey: FTIR microspectroscopic analysis of human osteonal bone *Calcified Tissue International* **59** 480–487 (1996). Cited on pages 14, 24, 45 and 78

[81] M. D. Morris and W. F. Finney: Recent developments in Raman and infrared spectroscopy and imaging of bone tissue *Spectroscopy: An International Journal* **18** 155–159 (2004).

[82] D. Farlay, G. Panczer, C. Rey, P. D. Delmas and G. Boivin: Mineral maturity and crystallinity index are distinct characteristics of bone mineral *Journal of Bone and Mineral Metabolism* **28** 433–445 (2010). Cited on page 14

[83] K. Akesson, M. D. Grynpas, R. G. Hancock, R. Odselius and K. J. Obrant: Energy-dispersive X-ray microanalysis of the bone mineral content in human trabecular bone: a comparison with ICPES and neutron activation analysis *Calcified Tissue International* **55** 236–239 (1994). Cited on page 14

[84] P. Roschger, P. Fratzl, J. Eschberger and K. Klaushofer: Validation of quantitative backscattered electron imaging for the measurement of mineral density distribution in human bone biopsies *Bone* **23** 319–326 (1998).

[85] J. G. Skedros, J. L. Holmes, E. G. Vajda and R. D. Bloebaum: Cement lines of secondary osteons in human bone are not mineral-deficient: new data in a historical perspective *The Anatomical Record. Part A, Discoveries in Molecular, Cellular, and Evolutionary Biology* **286** 781–803 (2005). Cited on page 14

[86] L. A. Feldkamp, S. A. Goldstein, A. M. Parfitt, G. Jesion and M. Kleerekoper: The direct examination of three-dimensional bone architecture in vitro by computed tomography *Journal of Bone and Mineral Research* **4** 3–11 (1989). Cited on page 15

[87] K. Engelke, W. Graeff, L. Meiss, M. Hahn and G. Delling: High spatial resolution imaging of bone mineral using computed microtomography. Comparison with microradiography and undecalcified histologic sections *Investigative Radiology* **28** 341–349 (1993). Cited on page 15

[88] M. Salomé, F. Peyrin, P. Cloetens, C. Odet, A. M. Laval-Jeantet, J. Baruchel and P. Spanne: A synchrotron radiation microtomography system for the analysis of trabecular bone samples *Medical Physics* **26** 2194–2204 (1999). Cited on page 15

[89] F. Peyrin, M. Salomé, S. Nuzzo, P. Cloetens, A. M. Laval-Jeantet and J. Baruchel: Perspectives in three-dimensional analysis of bone samples using synchrotron radiation microtomography *Cellular and Molecular Biology* **46** 1089–1102 (2000).

[90] S. Nuzzo, F. Peyrin, P. Cloetens, J. Baruchel and G. Boivin: Quantification of the degree of mineralization of bone in three dimensions using synchrotron radiation microtomography *Medical Physics* **29** 2672–2681 (2002). Cited on page 15

[91] M. Langer, A. Pacureanu, H. Suhonen, Q. Grimal, P. Cloetens and F. Peyrin: X-Ray Phase Nanotomography Resolves the 3d Human Bone Ultrastructure *PLoS One* **7** e35691 (2012). Cited on pages 15, 42, 55, 56 and 67

[92] A. Gourrier, W. Wagermaier, M. Burghammer, D. Lammie, H. S. Gupta, P. Fratzl, C. Riekel, T. J. Wess and O. Paris: Scanning X-ray imaging with small-angle scattering contrast *Journal of Applied Crystallography* **40** s78–s82 (2007). Cited on page 15

[93] R. Seidel, A. Gourrier, M. Kerschnitzki, M. Burghammer, P. Fratzl, H. S. Gupta and W. Wagermaier: Synchrotron 3d SAXS analysis of bone nanostructure *Bioinspired, Biomimetic and Nanobiomaterials* **1** 123–131 (2012). Cited on page 15

[94] D. Eichert, M. Salomé, M. Banu, J. Susini and C. Rey: Preliminary characterization of calcium chemical environment in apatitic and non-apatitic calcium phosphates of biological interest by X-ray absorption spectroscopy *Spectrochimica Acta Part B: Atomic Spectroscopy* **60** 850–858 (2005). Cited on page 15

[95] B. Hesse, M. Salome, H. Castillo-Michel, M. Cotte, B. Fayard, C. J. Sahle, W. De Nolf, J. Hradilova, A. Masic, B. Kanngießer et al.: Full-Field Calcium K-Edge X-ray Absorption Near-Edge Structure Spectroscopy on Cortical Bone at the Micron-Scale: Polarization Effects Reveal Mineral Orientation *Analytical Chemistry* **88** 3826–3835 (2016). Cited on page 15

[96] S. Lees, K. S. Prostak, V. K. Ingle and K. Kjoller: The loci of mineral in turkey leg tendon as seen by atomic force microscope and electron microscopy *Calcified Tissue International* **55** 180–189 (1994). Cited on page 16

[97] P. K. Zysset, X. E. Guo, C. E. Hoffler, K. E. Moore and S. A. Goldstein: Elastic modulus and hardness of cortical and trabecular bone lamellae measured by nanoindentation in the human femur *Journal of Biomechanics* **32** 1005–1012 (1999). Cited on page 16

[98] K. Raum, Q. Grimal and A. Gerisch: Multiscale structure-functional modeling of lamellar bone. *Acoustical Society of America Journal* **127** 2033 (2010). Cited on pages 16, 28, 34, 35 and 72

[99] I. R. Lewis and H. Edwards: Handbook of Raman Spectroscopy: From the Research Laboratory to the Process Line *CRC Press* (2001). Cited on page 13

[100] J. R. Ferraro, K. Nakamoto and C. W. Brown: Introductory Raman Spectroscopy *Academic Press* (2003). Cited on page 13

[101] E. DiMasi and L. B. Gower: Biomineralization Sourcebook: Characterization of Biominerals and Biomimetic Materials *CRC Press* (2014). Cited on page 13

[102] J. A. Timlin, A. Carden, M. D. Morris, R. M. Rajachar and D. H. Kohn: Raman Spectroscopic Imaging Markers for Fatigue-Related Microdamage in Bovine Bone *Analytical Chemistry* **72** 2229–2236 (2000). Cited on page 13

[103] E. Donnelly, A. L. Boskey, S. P. Baker, V. D. Meulen and M. C. H: Effects of tissue age on bone tissue material composition and nanomechanical properties in the rat cortex *Journal of Biomedical Materials Research Part A* **92A** 1048–1056 (2010). Cited on pages 13 and 17

[104] A. L. Dendramis, J. W. Poser and E. W. Schwinn: Laser raman spectroscopy of calf bone Gla protein *Biochimica et Biophysica Acta (BBA) - Protein Structure and Molecular Enzymology* **742** 525–529 (1983). Cited on page 18

[105] G. Penel, C. Delfosse, M. Descamps and G. Leroy: Composition of bone and apatitic biomaterials as revealed by intravital Raman microspectroscopy *Bone* **36** 893–901 (2005). Cited on page 18

[106] D. A. Shea and M. D. Morris: Bone Tissue Fluorescence Reduction for Visible Laser Raman Spectroscopy *Applied Spectroscopy* **56** 182–186 (2002). Cited on page 18

[107] D. Rohleder, G. Kocherscheidt, K. Gerber, W. Kiefer, W. Köhler, J. Möcks and W. Petrich: Comparison of mid-infrared and Raman spectroscopy in the quantitative analysis of serum *Journal of Biomedical Optics* **10** 031108 (2005). Cited on page 18

[108] C. Krafft, D. Codrich, G. Pelizzo and V. Sergo: Raman and FTIR microscopic imaging of colon tissue: a comparative study *Journal of Biophotonics* **1** 154–169 (2008). Cited on page 18

[109] P. Larkin: Infrared and Raman Spectroscopy *Elsevier* (2011). Cited on pages 18 and 19

[110] M. Tanaka and R. J. Young: Review Polarised Raman spectroscopy for the study of molecular orientation distributions in polymers *Journal of Materials Science* **41** 963–991 (2006). Cited on pages 19 and 20

[111] M. Tsuboi and G. J. Thomas: Raman Scattering Tensors in Biological Molecules and Their Assemblies *Applied Spectroscopy Reviews* (2006). Cited on pages 19 and 25

[112] M. Tsuboi, J. M. Benevides and J. George J. Thomas: Raman Tensors and their application in structural studies of biological systems *Proceedings of the Japan Academy, Series B* **85** 83–97 (2009). Cited on page 19

[113] D. Pienkowski, T. M. Doers, M.-C. Monier-Faugere, Z. Geng, N. P. Camacho, A. L. Boskey and H. H. Malluche: Calcitonin Alters Bone Quality in Beagle Dogs *Journal of Bone and Mineral Research* **12** 1936–1943 (1997). Cited on page 23

[114] H. Ou-Yang, E. P. Paschalis, W. E. Mayo, A. L. Boskey and R. Mendelsohn: Infrared microscopic imaging of bone: spatial distribution of CO3(2-) *Journal of Bone and Mineral Research* **16** 893–900 (2001). Cited on pages 23 and 24

[115] A. Awonusi, M. D. Morris and M. M. J. Tecklenburg: Carbonate Assignment and Calibration in the Raman Spectrum of Apatite *Calcified Tissue International* **81** 46–52 (2007). Cited on pages 23, 24 and 78

[116] C. P. Tarnowski, M. A. Ignelzi and M. D. Morris: Mineralization of Developing Mouse Calvaria as Revealed by Raman Microspectroscopy *Journal of Bone and Mineral Research* **17** 1118–1126 (2002). Cited on page 23

[117] B. R. McCreadie, M. D. Morris, T.-c. Chen, D. Sudhaker Rao, W. F. Finney, E. Widjaja and S. A. Goldstein: Bone tissue compositional differences in women with and without osteoporotic fracture *Bone* **39** 1190–1195 (2006). Cited on page 23

[118] J. J. Freeman, B. Wopenka, M. J. Silva and J. D. Pasteris: Raman spectroscopic detection of changes in bioapatite in mouse femora as a function of age and in vitro fluoride treatment *Calcified Tissue International* **68** 156–162 (2001). Cited on page 24

[119] O. Akkus, F. Adar and M. B. Schaffler: Age-related changes in physicochemical properties of mineral crystals are related to impaired mechanical function of cortical bone *Bone* **34** 443–453 (2004). Cited on page 24

[120] J. S. Yerramshetty, C. Lind and O. Akkus: The compositional and physicochemical homogeneity of male femoral cortex increases after the sixth decade *Bone* **39** 1236–1243 (2006). Cited on page 24

[121] N. Pleshko, A. Boskey and R. Mendelsohn: Novel infrared spectroscopic method for the determination of crystallinity of hydroxyapatite minerals. *Biophysical Journal* **60** 786 (1991). Cited on page 24

[122] J. D. Pasteris, B. Wopenka, J. J. Freeman, K. Rogers, E. Valsami-Jones, J. A. Houwen and M. J. Silva: Lack of OH in nanocrystalline apatite as a function of degree of atomic order: implications for bone and biomaterials *Biomaterials* **25** 229–238 (2004). Cited on page 24

[123] E. P. Paschalis, F. Betts, E. DiCarlo, R. Mendelsohn and A. L. Boskey: FTIR microspectroscopic analysis of human iliac crest biopsies from untreated osteoporotic bone *Calcified Tissue International* **61** 487–492 (1997). Cited on page 24

[124] S. J. Gadeleta, A. L. Boskey, E. Paschalis, C. Carlson, F. Menschik, T. Baldini, M. Peterson and C. M. Rimnac: A physical, chemical, and mechanical study of lumbar vertebrae from normal, ovariectomized, and nandrolone decanoate-treated cynomolgus monkeys (macaca fascicularis) *Bone* **27** 541–550 (2000). Cited on page 24

[125] M.-E. Rousseau, T. Lefèvre, L. Beaulieu, T. Asakura and M. Pézolet: Study of protein conformation and orientation in silkworm and spider silk fibers using Raman microspectroscopy *Biomacromolecules* **5** 2247–2257 (2004). Cited on page 25

[126] M. Tsuboi, J. M. Benevides, P. Bondre and G. J. Thomas: Structural details of the thermophilic filamentous bacteriophage PH75 determined by polarized Raman microspectroscopy *Biochemistry* **44** 4861–4869 (2005). Cited on page 26

[127] K. Raum, R. O. Cleveland, F. Peyrin and P. Laugier: Derivation of elastic stiffness from site-matched mineral density and acoustic impedance maps *Physics in medicine and biology* **51** 747–758 (2006). Cited on pages 28, 74 and 102

[128] F. Rupin, A. Saïed, D. Dalmas, F. Peyrin, S. Haupert, K. Raum, E. Barthel, G. Boivin and P. Laugier: Assessment of Microelastic Properties of Bone Using Scanning Acoustic Microscopy: A Face-to-Face Comparison with Nanoindentation *Japanese Journal of Applied Physics* **48** 07GK01 (2009). Cited on page 28

[129] I. Manjubala, Y. Liu, D. R. Epari, P. Roschger, H. Schell, P. Fratzl and G. N. Duda: Spatial and temporal variations of mechanical properties and mineral content of the external callus during bone healing *Bone* **45** 185–192 (2009). Cited on page 28

[130] G. Franzoso and P. K. Zysset: Elastic Anisotropy of Human Cortical Bone Secondary Osteons Measured by Nanoindentation *Journal of Biomechanical Engineering* **131** 021001 (2009). Cited on pages 28 and 88

[131] P. K. Zysset: Indentation of bone tissue: a short review *Osteoporosis international: a journal established as result of cooperation between the European Foundation for Osteoporosis and the National Osteoporosis Foundation of the USA* **20** 1049–1055 (2009). Cited on page 28

[132] R. C. Preston: Output Measurements for Medical Ultrasound *Springer Science & Business Media* (1991). Cited on page 28

[133] D. Rohrbach: Quantitative ultrasound in transverse transmission for bone quality assessment and monitoring fracture healing *Humboldt-Universität zu Berlin* (2013). Cited on page 29

[134] J. Achenbach: Wave Propagation in Elastic Solids, Volume 16 *North Holland* (1987). Cited on page 31

[135] G. S. Kino: Acoustic Waves: Devices, Imaging, and Analog Signal Processing *Prentice Hall* (1987).

[136] B. A. Auld: Acoustic fields and waves in solids *R.E. Krieger* (1990). Cited on page 32

[137] D. Royer and E. Dieulesaint: Elastic Waves in Solids II: Generation, Acousto-optic Interaction, Applications *Springer Science & Business Media* (1999). Cited on page 31

[138] K. Raum: Microelastic imaging of bone *IEEE Transactions on Ultrasonics, Ferroelectrics and Frequency Control* **55** 1417–1431 (2008). Cited on pages 33 and 72

[139] S. Hirsekorn, S. Pangraz, G. Weides and W. Arnold: Measurement of elastic impedance with high spatial resolution using acoustic microscopy *Applied Physics Letters* **67** 745–747 (1995). Cited on page 34

[140] S. Hirsekorn, S. Pangraz, G. Weides and W. Arnold: Erratum: "Measurement of elastic impedance with high spatial resolution using acoustic microscopy" [Appl. Phys. Lett. 67, 745 (1995)] *Applied Physics Letters* **69** 2138–2138 (1996). Cited on page 34

[141] P. Laugier and G. Haïat: Bone Quantitative Ultrasound *Springer* (2011). Cited on pages 35 and 36

[142] P. M. Morse and K. U. Ingard: Theoretical Acoustics *Princeton University Press* (1987). Cited on page 35

[143] J. D. Jackson: Classical electrodynamics *Wiley* (1975). Cited on page 37

[144] T. J. Davis, D. Gao, T. E. Gureyev, A. W. Stevenson and S. W. Wilkins: Phase-contrast imaging of weakly absorbing materials using hard X-rays *Nature* **373** 595–598 (1995). Cited on page 38

[145] A. Guinier, A. Guinier and Guinier: X-Ray Diffraction: In Crystals, Imperfect Crystals, and Amorphous Bodies *Dover Pubn Inc* (1994). Cited on page 39

[146] F. Pfeiffer, T. Weitkamp, O. Bunk and C. David: Phase retrieval and differential phase-contrast imaging with low-brilliance X-ray sources *Nature Physics* **2** 258–261 (2006). Cited on page 39

[147] B. Hesse: Characterization of tissue properties on the sub-micron scale in human bone by means of synchrotron radiation CT *Humboldt-Universität zu Berlin* (2014). Cited on page 40

[148] T. Weitkamp, A. Diaz, C. David, F. Pfeiffer, M. Stampanoni, P. Cloetens and E. Ziegler: X-ray phase imaging with a grating interferometer *Optics Express* **13** 6296–6304 (2005). Cited on page 39

[149] V. N. Ingal and E. A. Beliaevskaya: X-ray plane-wave topography observation of the phase contrast from a non-crystalline object *Journal of Physics D: Applied Physics* **28** 2314 (1995). Cited on page 39

[150] D. Chapman, W. Thomlinson, R. E. Johnston, D. Washburn, E. Pisano, N. Gmür, Z. Zhong, R. Menk, F. Arfelli and D. Sayers: Diffraction enhanced x-ray imaging *Physics in Medicine and Biology* **42** 2015 (1997). Cited on page 39

[151] S. W. Wilkins, T. E. Gureyev, D. Gao, A. Pogany and A. W. Stevenson: Phase-contrast imaging using polychromatic hard X-rays *Nature* **384** 335–338 (1996). Cited on page 39

[152] P. Cloetens, W. Ludwig, J. Baruchel, D. V. Dyck, J. V. Landuyt, J. P. Guigay and M. Schlenker: Holotomography: Quantitative phase tomography with micrometer resolution using hard synchrotron radiation x rays *Applied Physics Letters* **75** 2912–2914 (1999). Cited on page 40

[153] M. Langer, P. Cloetens and F. Peyrin: Regularization of phase retrieval with phase-attenuation duality prior for 3-D holotomography *IEEE Transactions on Image Processing* **19** 2428–2436 (2010). Cited on page 39

[154] H. F. Talbot: LXXVI. Facts relating to optical science. No. IV *Philosophical Magazine Series 3* **9** 401–407 (1836). Cited on page 40

[155] P. Cloetens, J. P. Guigay, C. D. Martino, J. Baruchel and M. Schlenker: Fractional Talbot imaging of phase gratings with hard x rays *Optics Letters* **22** 1059–1061 (1997). Cited on page 40

[156] D. Paganin, S. C. Mayo, T. E. Gureyev, P. R. Miller and S. W. Wilkins: Simultaneous phase and amplitude extraction from a single defocused image of a homogeneous object *Journal of Microscopy* **206** 33–40 (2002). Cited on page 40

[157] P. Varga, B. Hesse, M. Langer, S. Schrof, N. Männicke, H. Suhonen, A. Pacureanu, D. Pahr, F. Peyrin and K. Raum: Synchrotron X-ray phase nano-tomography-based analysis of the lacunar–canalicular network morphology and its relation to the strains experienced by osteocytes in situ as predicted by case-specific finite element analysis *Biomechanics and Modeling in Mechanobiology* **14** 267–282 (2014). Cited on pages 42 and 64

[158] B. Hesse, P. Varga, M. Langer, A. Pacureanu, S. Schrof, N. Männicke, H. Suhonen, P. Maurer, P. Cloetens, F. Peyrin and K. Raum: Canalicular Network Morphology Is the Major Determinant of the Spatial Distribution of Mass Density in Human Bone Tissue: Evidence by Means of Synchrotron Radiation Phase-Contrast nano-CT *Journal of Bone and Mineral Research* **30** 346–356 (2015). Cited on pages 42 and 68

[159] V. J. Kingsmill and A. Boyde: Mineralisation density of human mandibular bone: quantitative backscattered electron image analysis *Journal of Anatomy* **192** 245–256 (1998). Cited on pages 43, 55 and 56

[160] S. Schrof, P. Varga, L. Galvis, K. Raum and A. Masic: 3d Raman mapping of the collagen fibril orientation in human osteonal lamellae *Journal of Structural Biology* **187** 266–275 (2014). Cited on pages 45 and 49

[161] P. Fratzl, W. Wagermaier, A. Gourrier, M. Burghammer, M. Kerschnitzki, R. Seidel and H. S. Gupta: Synchrotron 3d SAXS analysis of bone nanostructure *Bioinspired, Biomimetic and Nanobiomaterials* **1** 123–131 (2012). Cited on page 45

[162] A. Faingold, S. R. Cohen, N. Reznikov and H. D. Wagner: Osteonal lamellae elementary units: Lamellar microstructure, curvature and mechanical properties *Acta Biomaterialia* **9** 5956–5962 (2013). Cited on page 56

[163] A. Gautieri, S. Vesentini, A. Redaelli and M. J. Buehler: Hierarchical Structure and Nanomechanics of Collagen Microfibrils from the Atomistic Scale Up *Nano Letters* **11** 757–766 (2011). Cited on page 58

[164] P. Fratzl, K. Misof, I. Zizak, G. Rapp, H. Amenitsch and S. Bernstorff: Fibrillar Structure and Mechanical Properties of Collagen *Journal of Structural Biology* **122** 119–122 (1998). Cited on page 58

[165] S. Schrof, P. Varga, B. Hesse, M. Schöne, R. Schütz, A. Masic and K. Raum: Multimodal correlative investigation of the interplaying microarchitecture, chemical composition and mechanical properties of human cortical bone tissue reveals predominant role of fibrillar organization in determining microelastic tissue properties *Acta Biomaterialia* **44** 51–64 (2016). Cited on pages 63, 66, 73, 77, 80, 81, 84, 85, 87 and 126

[166] E. Dall'Ara, B. Luisier, R. Schmidt, M. Pretterklieber, F. Kainberger, P. Zysset and D. Pahr: DXA predictions of human femoral mechanical properties depend on the load configuration *Medical Engineering and Physics* **35** 1564–1572 (2013). Cited on pages 64 and 65

[167] A. G. Reisinger, D. H. Pahr and P. K. Zysset: Sensitivity analysis and parametric study of elastic properties of an unidirectional mineralized bone fibril-array using mean field methods *Biomechanics and Modeling in Mechanobiology* **9** 499–510 (2010). Cited on page 71

[168] S. Lakshmanan, A. Bodi and K. Raum: Assessment of anisotropic tissue elasticity of cortical bone from high-resolution, angular acoustic measurements *IEEE transactions on ultrasonics, ferroelectrics, and frequency control* **54** 1560–1570 (2007). Cited on pages 72 and 95

[169] B. Preininger, S. Checa, F. L. Molnar, P. Fratzl, G. N. Duda and K. Raum: Spatial-temporal mapping of bone structural and elastic properties in a sheep model following osteotomy *Ultrasound in Medicine & Biology* **37** 474–483 (2011). Cited on page 72

[170] M. Petra, J. Anastassopoulou, T. Theologis and T. Theophanides: Synchrotron micro-FT-IR spectroscopic evaluation of normal paediatric human bone *Journal of Molecular Structure* **733** 101–110 (2005). Cited on page 77

[171] H. D. Barth, E. A. Zimmermann, E. Schaible, S. Y. Tang, T. Alliston and R. O. Ritchie: Characterization of the effects of x-ray irradiation on the hierarchical structure and mechanical properties of human cortical bone *Biomaterials* **32** 8892–8904 (2011). Cited on page 89

[172] A. Bushby, V. Ferguson and A. Boyde: Nanoindentation of bone: Comparison of specimens tested in liquid and embedded in polymethylmethacrylate *Journal of Materials Research* **19** 249–259 (2004). Cited on page 89

[173] J. Kühnisch, J. Seto, C. Lange, S. Schrof, S. Stumpp, K. Kobus, J. Grohmann, N. Kossler, P. Varga, M. Osswald et al.: Multiscale, converging defects of macro-porosity, microstructure and matrix mineralization impact long bone fragility in NF1 *PLoS One* **9** e86115 (2014). Cited on pages 93 and 98

[174] X. Wu, S. A. Estwick, S. Chen, M. Yu, W. Ming, T. D. Nebesio, Y. Li, J. Yuan, R. Kapur, D. Ingram, M. C. Yoder and F.-C. Yang: Neurofibromin plays a critical role in modulating osteoblast differentiation of mesenchymal stem/progenitor cells *Human Molecular Genetics* **15** 2837–2845 (2006). Cited on page 93

[175] A. Schindeler and D. G. Little: Recent insights into bone development, homeostasis, and repair in type 1 neurofibromatosis (NF1) *Bone* **42** 616–622 (2008). Cited on page 93

[176] W. Zhang, S. D. Rhodes, L. Zhao, Y. He, Y. Zhang, Y. Shen, D. Yang, X. Wu, X. Li, X. Yang et al.: Primary osteopathy of vertebrae in a neurofibromatosis type 1 murine model *Bone* **48** 1378–1387 (2011). Cited on page 93

[177] S. Alwan, S. J. Tredwell and J. M. Friedman: Is osseous dysplasia a primary feature of neurofibromatosis 1 (NF1)? *Clinical Genetics* **67** 378–390 (2005). Cited on page 93

[178] M. Kolanczyk, J. Kühnisch, N. Kossler, M. Osswald, S. Stumpp, B. Thurisch, U. Kornak and S. Mundlos: Modelling neurofibromatosis type 1 tibial dysplasia and its treatment with lovastatin *BMC Medicine* **6** 21 (2008). Cited on pages 94 and 95

[179] D. A. Stevenson, J. C. Carey, D. H. Viskochil, L. J. Moyer-Mileur, H. Slater, M. A. Murray, J. L. D'Astous and K. A. Murray: Analysis of radiographic characteristics of anterolateral bowing of the leg before fracture in neurofibromatosis type 1 *Journal of Pediatric Orthopedics* **29** 385–392 (2009). Cited on page 93

[180] F. Elefteriou, M. D. Benson, H. Sowa, M. Starbuck, X. Liu, D. Ron, L. F. Parada and G. Karsenty: ATF4 mediation of NF1 functions in osteoblast reveals a nutritional basis for congenital skeletal dysplasiae *Cell Metabolism* **4** 441–451 (2006). Cited on pages 93, 94 and 98

[181] F. Elefteriou, M. Kolanczyk, A. Schindeler, D. H. Viskochil, J. M. Hock, E. K. Schorry, A. H. Crawford, J. M. Friedman, D. Little, J. Peltonen et al.: Skeletal abnormalities in neurofibromatosis type 1: approaches to therapeutic options *American Journal of Medical Genetics. Part A* **149A** 2327–2338 (2009). Cited on pages 93 and 94

[182] M. Kolanczyk, N. Kossler, J. Kühnisch, L. Lavitas, S. Stricker, U. Wilkening, I. Manjubala, P. Fratzl, R. Spörle, B. G. Herrmann, L. F. Parada, U. Kornak and S. Mundlos: Multiple roles for neurofibromin in skeletal development and growth *Human Molecular Genetics* **16** 874–886 (2007). Cited on pages 94, 95 and 98

[183] K. Raum, T. Hofmann, I. Leguerney, A. Saïed, F. Peyrin, L. Vico and P. Laugier: Variations of microstructure, mineral density and tissue elasticity in B6/C3h mice *Bone* **41** 1017–1024 (2007). Cited on page 94

[184] M. Lammert, M. Kappler, V.-F. Mautner, K. Lammert, S. Störkel, J. M. Friedman and D. Atkins: Decreased bone mineral density in patients with neurofibromatosis 1 *Osteoporosis International* **16** 1161–1166 (2005). Cited on page 98

[185] S. Seitz, C. Schnabel, B. Busse, H. U. Schmidt, F. T. Beil, R. E. Friedrich, T. Schinke, V. F. Mautner and M. Amling: High bone turnover and accumulation of osteoid in patients with neurofibromatosis 1 *Osteoporosis International* **21** 119–127 (2010). Cited on page 98

Supplementary Information

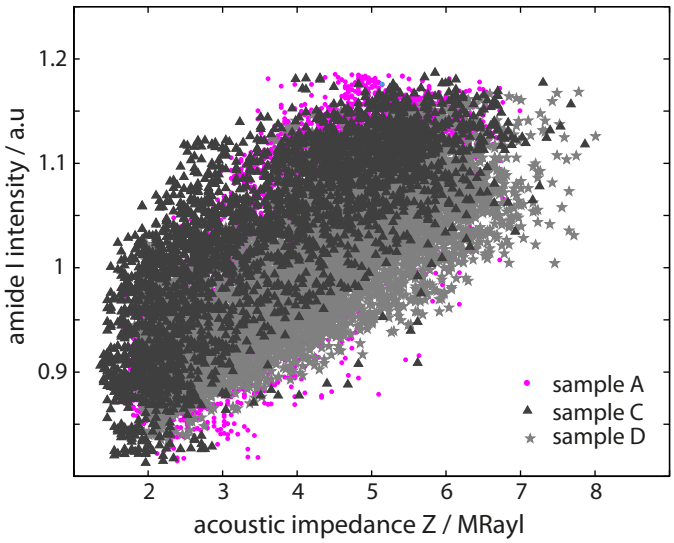

Figure 4.1: **Spatial point-by-point correlation of acoustic impedance Z and amide I intensity of pooled data sets of three osteons of three different samples.**

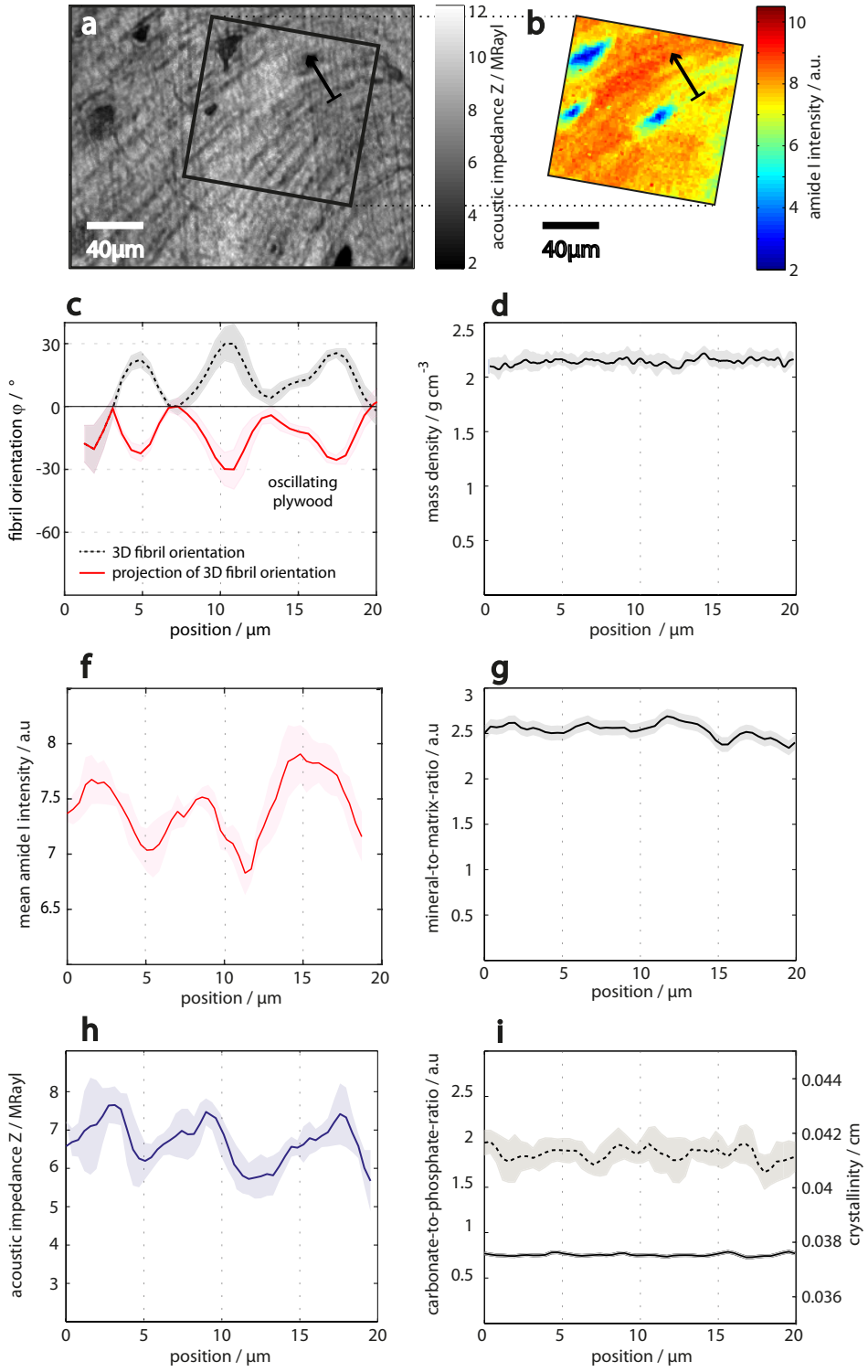

Figure 4.2: Comparative line profile analysis of several interstitial tissue lamellae by means SR-nanoCT, PRS and SAM. (a) SAM acoustic impedance map. The black arrow marks the location of the presented line profiles. (b) Corresponding amide I intensity map. (c) 3D quantitative fibril orientation φ (black line) and the corresponding projection (red line) derived by means of SR-nanoCT. (c) Line profile of the lamellar mass density ditsribution. Corresponding profiles of PRS tissue parameters of the same lamellae (f,g,i) and acoustic impedance Z (h). Image reprinted from [165] with permission from Elsevier.

List of Abbreviations

2D	two-dimensional
3D	three-dimensional
aBMD	areal bone mineral density
ACF	autocorrelation function
AFM	atomic force microscopy
cdf	cumulative density function
CLSM	confocal laser scanning microscopy
CTPR	carbonate-to-phosphate-ratio
DXA	dual-energy X-ray Absorptiometry
EDX	energy dispersive X-ray spectroscopy
FIB-SEM	serial focused ion beam SEM
FFT	fast Fourier transformation
FTIR	Fourier transformed infrared spectroscopy
FWHM	full width at half maximum
hAp	hydroxyapatite
IT	interstitial tissue
LCN	lacuno-canalicular network
LM	light microscopy
MTMR	mineral-to-matrix-ratio
NA	numerical aperture
NCP	non-collagenous protein

NF1	Neurofibromatosis type 1
Nf1	neurofibromin 1 gene
NI	nanoindentation
OT	osteonal tissue
PRS	polarized Raman spectroscopy
qBEI	Quantitative backscattered electron imaging
ROI	region of interest
RS	Raman spectroscopy
RTT	rat tail tendon
SAXS	small angle X-ray scattering
SAM	scanning acoustic microscopy
SEM	scanning electron microscopy
SR-nanoCT	synchrotron phase contrast nano computed tomography
SR-μCT	synchrotron phase contrast micro computed tomography
TEM	transmission electron microscopy
VOI	volume of interest
WAXD	wide angle X-ray diffraction
XANES	X-ray absorption near edge spectroscopy

List of Figures

List of Tables

List of Publications

S. Schrof, P. Varga, B. Hesse, M. Schöne, R. Schütz, A. Masic and K. Raum: Multimodal correlative investigation of the interplaying microarchitecture, chemical composition and mechanical properties of human cortical bone tissue reveals predominant role of fibrillar organization in determining microelastic tissue properties *Acta Biomaterialia* **44** 51–64

R. Penta, K. Raum, Q. Grimal, **S. Schrof** and A. Gerisch: Can a continuous mineral foam explain the stiffening of aged bone tissue? A micromechanical approach to mineral fusion in musculoskeletal tissues *Bioinspiration Biomimetics* **11** 035004 (2016).

B. Hesse, M. Salome, H. Castillo-Michel, M. Cotte, B. Fayard, C. J. Sahle, W. De Nolf, J. Hradilova, A. Masic, B. Kanngießer, Bohner M., Varga P., Raum K., **S. Schrof**: Full-Field Calcium K-Edge X-ray Absorption Near-Edge Structure Spectroscopy on Cortical Bone at the Micron-Scale: Polarization Effects Reveal Mineral Orientation *Analytical Chemistry* **88** 3826–3835 (2016).

S. Schrof, P. Varga, L. Galvis, K. Raum and A. Masic: 3D Raman mapping of the collagen fibril orientation in human osteonal lamellae *Journal of Structural Biology* **187** 266–275 (2014).

B. Hesse, P. Varga, M. Langer, A. Pacureanu, **S. Schrof**, N. Männicke, H. Suhonen, P. Maurer, P. Cloetens, F. Peyrin and K. Raum: Canalicular Network Morphology Is the Major Determinant of the Spatial Distribution of Mass Density in Human Bone Tissue: Evidence by Means of Synchrotron Radiation Phase-Contrast nano-CT *Journal of Bone and Mineral Research* **30** 346–356 (2015).

P. Varga, B. Hesse, M. Langer, **S. Schrof**, N. Männicke, H. Suhonen, A. Pacureanu, D. Pahr, F. Peyrin and K. Raum: Synchrotron X-ray phase nanotomography-based analysis of the lacunar–canalicular network morphology and its relation to the strains experienced by osteocytes in situ as predicted by case-specific finite element analysis B*iomechanics and Modeling in Mechanobiology* **14** 267–282 (2014).

B. Hesse, M. Langer, P. Varga, A. Pacureanu, P. Dong, **S. Schrof**, N. Männicke, H. Suhonen, C. Olivier, P. Maurer, G. J. Kazakia, K. Raum and F. Peyrin: Alterations of Mass Density and 3d Osteocyte Lacunar Properties in Bisphosphonate-Related Osteonecrotic Human Jaw Bone, a Synchrotron μCT Study *PLoS One* **9** e88481 (2014).

S. Tiburtius, **S. Schrof**, F. Molnár, P. Varga, F. Peyrin, Q. Grimal, K. Raum and A. Gerisch: On the elastic properties of mineralized turkey leg tendon tissue: multiscale model and experiment *Biomechanics and Modeling in Mechanobiology* **13** 1003-1023 (2014).

J. Kühnisch, J. Seto, C. Lange, **S. Schrof**, S. Stumpp, K. Kobus, J. Grohmann, N. Kossler, P. Varga, M. Osswald et al.: Multiscale, converging defects of macro-porosity, microstructure and matrix mineralization impact long bone fragility in NF1 **PLoS One 9** e86115 (2014).

S. Schrof, T. Staudt, E. Rittweger, N. Wittenmayer, T. Dresbach, J. Engelhardt and S. W. Hell: STED nanoscopy with mass-produced laser diodes *Optics Express* **19** 8066–8072 (2011).

Acknowledgments

For reasons of data protection, the acknowledgments are not included in the online version.

Ich erkläre, dass ich die Dissertation selbständig und nur unter Verwendung der von mir gemäß § 7 Abs. 3 der Promotionsordnung der Mathematisch-Naturwissenschaftlichen Fakultät, veröffentlicht im Amtlichen Mitteilungsblatt der Humboldt-Universität zu Berlin Nr. 126/2014 am 18.11.2014 angegebenen Hilfsmittel angefertigt habe.

Berlin, den _____